Summer 8-1-2021

Doping of Conjugated Polymers: Preparation, Characterization and Device Fabrication

Kan Tang

DOPING OF CONJUGATED POLYMERS: PREPARATION, CHARACTERIZATION AND DEVICE FABRICATION

by

Kan Tang

A Dissertation
Submitted to the Graduate School,
the College of Arts and Sciences
and the School of Mathematics and Natural Sciences
at The University of Southern Mississippi
in Partial Fulfillment of the Requirements
for the Degree of Doctor of Philosophy

Approved by:

Song Guo, Ph. D., Committee Chair
Xiaodan Gu, Ph. D.
David Hayhurst, Ph. D.
Wujian Miao, Ph. D.
Karl Wallace, Ph. D.

August 2021

ABSTRACT

Semiconducting conjugated polymers (CPs) as emerging materials for advanced electronic applications such as sensors, OPVs, and OEFTs has become an intriguing research topic in the past decades. It opens a new avenue of "flexible" electronics, which has shown great potential in next-generation electronic devices.

However, due to the nature of CP materials and related solution processing techniques, unlike almost perfectly crystalline silicon materials, CPs in the solid-state often exhibit much lower crystallinity if it is not complete amorphous, which severely hinder the electronic property and optical property of the materials. The crystallinity of CPs in a film is often uniquely governed by the aggregation process involving intermolecular interactions such as π-π stacking. On the other hand, chemical doping of CPs by a dopant is regarded as an effective method to enhance the performance of CPs by increasing their conductivity by several orders of magnitude. By a combination of optical and microscopic techniques, the π-π aggregation of P3HT, a typical CP, has been proved to capable of promoting its chemical doping with F4TCNQ. The *I*-*V* characteristics shows that the doped P3HT film has a 10^5 times higher conductivity than the undoped P3HT film.

Besides the preparation of CP films, novel nanostructures of CPs such as highly crystalline nanowires with a width <100 nm can also be prepared. By a combination of AFM and KPFM technique, the relationship between surface potential and doping regime can be established for chemically doped P3HT nanowires. Overly doped P3HT nanowires exhibit distinct "dot-like" dark features in KPFM imaging as compare to undoped and

moderately doped P3HT nanowires, which is corresponding to the morphological feature in the AFM topography imaging.

Apart from chemical doping of CPs, a new doping route based on manipulating ion injection into/out of the CP films has been developed. The so-called organic electrochemical transistors (OECTs) have been fabricated on interdigitated electrodes (IDEs). This lithography-free set-up of OECTs show improved water stability under cycling gate bias conditions after crosslinking, which provides a useful platform for the applications such as bio-sensing.

ACKNOWLEDGMENTS

First, I would like to sincerely thank my research advisor, Dr. Song Guo, for supervising my research projects throughout my PhD program. I am grateful for the grand vision and helpful discussion you provided for the research topics, particularly in the principles of AFM and electrochemical redox processes, which leads to a productive period. It is your generosity, patience, and inspirational thoughts that promote the advance in both my graduate program and daily life. I am also grateful to have the chance to work with the members in Dr. Guo's lab, so thank you, Amin, Nick, and Trishal for the assistance and accompany in the journey.

I also would like to thank Dr. Wujian Miao in the Department of Chemistry and Biochemistry for his suggestion in electrochemistry and instrumentation. Also, Arati and Jesse, thank you for the help in setting up materials and devices for electrochemical measurements.

The experiments in this thesis also got a lot of help from the School of polymers and High-Performance Materials. The electronic characterization of materials was assisted by Dr. Jason Azoulay and Dr. Xiaodan Gu's labs. So, thank you Lifeng, Jasmine, and Song for your generous help in operating some of the state-of-art lab equipment such as probe station and small-angle X-ray scattering line amid your own busy graduate school lives.

I also want to thank my committee members Dr. Karl Wallace and Dr. David Hayhurst in the Department of Chemistry and Biochemistry for providing valuable suggestions on the projects. Also, Mrs. Sharon King, Ms. Tina Masterson, and Ms. Autumn

Webb, thanks for your help in general graduate program issues and lab teaching. Finally, I would like to acknowledge the financial support from the University of Southern Mississippi and the NSF CAREER award (NSF DMR-1554841).

TABLE OF CONTENTS

LIST OF TABLES

LIST OF ILLUSTRATIONS

CHAPTER I – Background and Experimental Techniques

1.1 Introduction of Conjugated Polymers

Conjugated polymer (CP) as a representative π-conjugated system has emerged as a promising material for electronic devices.[1-7] For example, a water-soluble conjugated polymer, poly(3,4-ethylenedioxythiophene) polystyrene sulfonate (PEDOT:PSS), has been widely used as transparent conductive coatings for flexible electrode, which exhibits promising potential in the replacement of rigid, expensive, and environmentally unfriendly indium tin oxide (ITO).[8-10] This offers new possibilities especially in OLED displays and printed electronics. On the other hand, poly(3-hexylthiophene) (P3HT), a classic polythiophene material, has been regarded as a benchmark material for organic electronic devices such as organic photovoltaics (OPVs)[11] and organic field-effect transistors (OFETs).[12-14]

The research on CP was initiated in the 1970s with the accidental discovery of metallic electrical conductivity in iodine doped polyacetylene, so-called "synthetic metal", by Heeger, MacDiarmid, and Shirakawa.[15, 16] Their pioneering work on conductive polymers led to the award of Nobel Prize in Chemistry in 2000. Following the original work in polyacetylene, research on CP gradually switches to coplanar aromatic systems involving monomers such as pyrrole, benzene, aniline, and thiophene (Figure 1.1), mainly due to improved stability and their nondegenerate ground states.[17-19] In particular, polythiophene (PT) is one of the most studied aromatic systems and is regarded as a stable and versatile compound for organic electronics.[18, 19] Two major polymerization methods

are adopted in the synthesis of PT, (i) electrochemical polymerization of designated thiophene monomer on electrode[20-22] and (ii) nickel-catalyzed polymerization of thiophene monomer in a Grignard reagent form.[23-27] Recently, there is ascending research attention devoted to the precise synthesis of PTs.

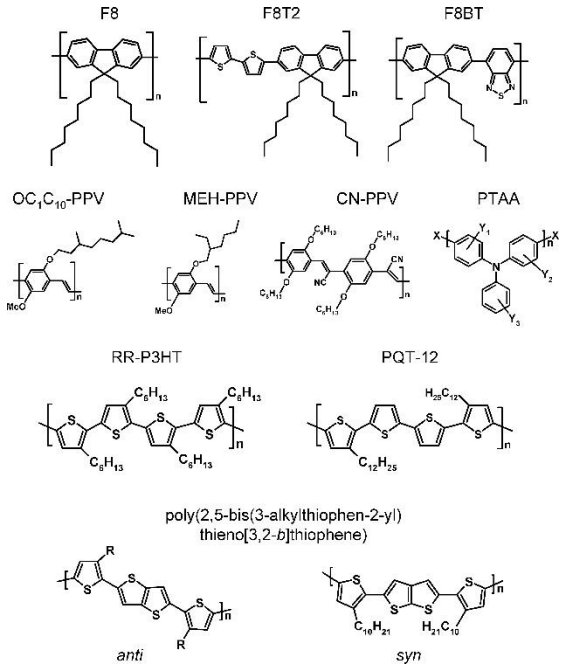

Figure 1.1 *Typical P-type and N-type conjugated polymers. Reproduced with permission from Ref.[28] Copyright (2007) American Chemical Society.*

Bandgap (E_g) of material largely affects the charge transport because more charge carriers can be thermally excited into conduction band if E_g can be effectively reduced. However, low dimensional materials such as π-π stacking PTs generally result in a theoretical E_g larger than 1.50 eV, which is not ideal for effective charge transport.[19] Localization of π electrons due to the coupling of electrons and phonons caused by defects inside materials is believed to be responsible for this phenomenon. Roncali proposed a comprehensive expression for the E_g of CP as follows,[19]

$$E_g = E^{\delta r} + E^{\theta} + E^{Res} + E^{Sub} + E^{int} \qquad \text{(Eq. 1.1)}$$

where $E^{\delta r}$ stands for the contribution from the degree of bond length alternation (BLA), E^{θ} represents E_g increase due to the departure from coplanarity, E^{Res} is the contribution from delocalization of π electrons, E^{Sub} accounts for the effect introduced by substituents and E^{int} is the contribution from the interchain coupling. Note that the first four terms in the equation account for intramolecular ordering while the last term involves intermolecular ordering. That means to effectively reduce E_g, increasing both intra- and intermolecular ordering is necessary for improving the intrinsic electrical conductivity of PTs without the presence of oxidative doping. For a π-conjugated system like PTs, molecular ordering is determined by both single-chain conformation and interchain folding/aggregation. Next, a detailed discussion on the molecular ordering of PTs will be presented.

1.2 Molecular Ordering of Conjugated Polymers: Structures and Properties

It is not difficult to imagine both intramolecular and intermolecular interactions would have decisive effects on the behavior of excitons and/or polarons transportation within the materials. Even for a conjugated polymer with fixed chemical compositions, those interactions can also strongly depend on the molecular packing of chain segments. Typically, higher molecular ordering and lower temperature promote delocalization of excitons while defects and higher temperature prefer localization. However, due to various conditions of the formation of conjugated polymer aggregates, molecular interactions within those materials can be complicated. Therefore, understanding the influences of molecular ordering on the optoelectronic properties of conjugated polymer aggregates can be crucial in the photochemical processes or devices involving conjugated polymers, such as OPVs and OECTs.

1.2.1 Fundamentals on the Spectroscopy of Conjugated Polymers: J - and H - aggregates

Molecular aggregate systems like π-π stacking polythiophene aggregates exhibit properties of special chromophores in contract to isolated monomers, for example, absorption band can be shifted to a longer wavelength (red-shifted) or a shorter wavelength (blue-shifted) compared to the monomer absorption band. As pointed out in a ceremonial review article by Wurthner et al.,[29] it was initiated by the unusual finding of the appearance of an intense, redshifted narrow band in the UV-vis absorption spectrum of pseudoisocyanine chloride (PIC) in water, which was discovered independently by Jelly and Scheibe almost 80 years ago, as a consequence of emerging dye research back in time.[30, 31] The fundamental ideas on understanding photochemical characteristics such as adsorption and emission of molecular aggregates were firstly established by Kasha and his coworkers around 1960s.[32, 33] Kesha's theory introduces a solid model that well explains the basics of the photochemical phenomenon of molecular aggregate systems, especially for the dyes. Recently, Spano et al. further developed and expanded Kasha's theory and used it to successfully interpret and explain adsorption and emission of various aggregate systems on conjugated polymers[34-42], which greatly fulfills the rapid development of conjugated polymer materials. The following introduction on Kesha's model will use the formalisms from Spano.[34, 38, 39, 43]

When vibronic coupling and overlaps of nearest-neighbor wave functions are neglected, the Coulomb coupling (J_C) between two identical molecules with the same transition dipole moment (μ) can be written as,

$$J_C = \frac{\mu^2(1-3cos^2\theta)}{4\pi R^3} \qquad \text{(Eq. 1.2)}$$

in which μ is the transition dipole moment corresponding to the transition from ground state S_0 to the first excited state S_1, R is the distance between two centers of adjacent molecules, and ε is the dielectric constant of the (solvent) medium. The incline angle θ (Figure 1.2) characterizes the relative translation of adjacent molecules in the long molecular axis direction of the aggregate when θ approaches 0, the transition dipoles of molecules tend to be "head-to-tail", meaning there is a larger intermolecular slip. While if θ is close to $\pi/2$, the orientation of dipoles become "side-by-side", which indicates no intermolecular slip. There is a specific angle by which the Coulomb coupling

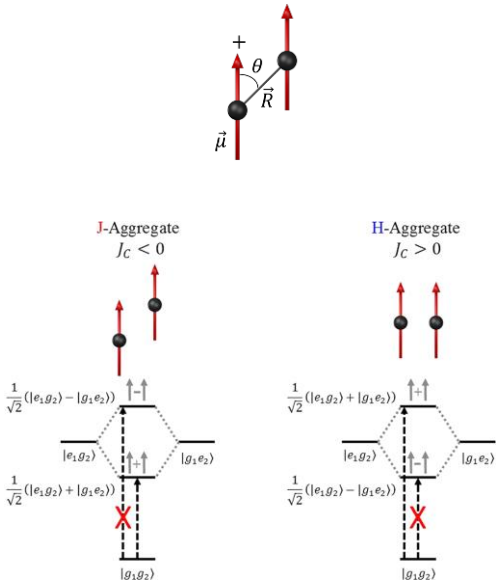

Figure 1.2 *Transition dipole moments of simplified point of mass and schematic molecular orbitals for the dimers of both J- type and H-type aggregate. The energy splitting at excited states is* $2|J_C|$ *for both J- and H-aggregates. Reproduced with permission from Ref.*[35] *Copyright (2018) American Chemical Society.*

(J_C) equals 0. This is the so-called "magic angle" $\theta_M = 54.7^o$. According to Kesha's theory, H-aggregates have a smaller intermolecular slip, resulting in positive J_C and a "side-by-

side" orientation between transition dipoles ($\theta_M < \theta < \pi/2$). In contrast, transition dipoles in J-aggregates maintain a "head-to-tail" orientation ($0 < \theta < \theta_M$) due to the large slip in the long axis, which corresponds to a negative Coulomb coupling. As shown in Figure 1.2, the sign of J_C determines the photochemical response of molecular aggregates. The energy level of the in-phase state is shifted by J_C as compared to the energy of the excited state of a monomer while the energy level out-of-phase state is shifted by $-J_C$. As a result, the symmetric linear combination of the two excited states $|e_1g_2\rangle + |g_1e_2\rangle$ occupies a lower energy state than antisymmetric state $|e_1g_2\rangle - |g_1e_2\rangle$ in J-aggregates, while in H-aggregate the order is just in reverse. The excitation from the ground state to the antisymmetric excited state is strongly suppressed due to the offset of the transition dipole moments attributed to the aggregates in the antisymmetric state. Therefore, in H-aggregates, the absorption is blue-shifted compared to the adsorption of monomer, while the absorption in J-aggregates is red-shifted. As for photoluminescence (PL), Kesha's rule states that fluorescence occurs with the transition from the lowest excited state to the ground states.[44] In H-aggregates, exciton has to undergo a rapid intraband relaxation from the symmetric $|e_1g_2\rangle + |g_1e_2\rangle$ state to the antisymmetric excited state $|e_1g_2\rangle - |g_1e_2\rangle$ after absorption. However, due to the cancellation of the transition dipole moment, the antisymmetric excited state is not directly coupling to the ground state radiatively, resulting in a strong depression of 0-0 fluorescence as shown in Figure 1.3. The reason why 0-0 excitation and emission are not strictly forbidden is because of thermal activation and inevitable structural disorder, which breaks the symmetry and makes 0-0 transitions of H-aggregates still accessible in a suppressed manner. In contrast, the largely populated excited state in J-

aggregates is already the symmetric state with the lowest energy, therefore, the 0-0 fluorescence is promoted. In fact, for a molecular aggregate with N coupled chromophores, the decay rate is amplified by N times compared to the emission of single monomers.

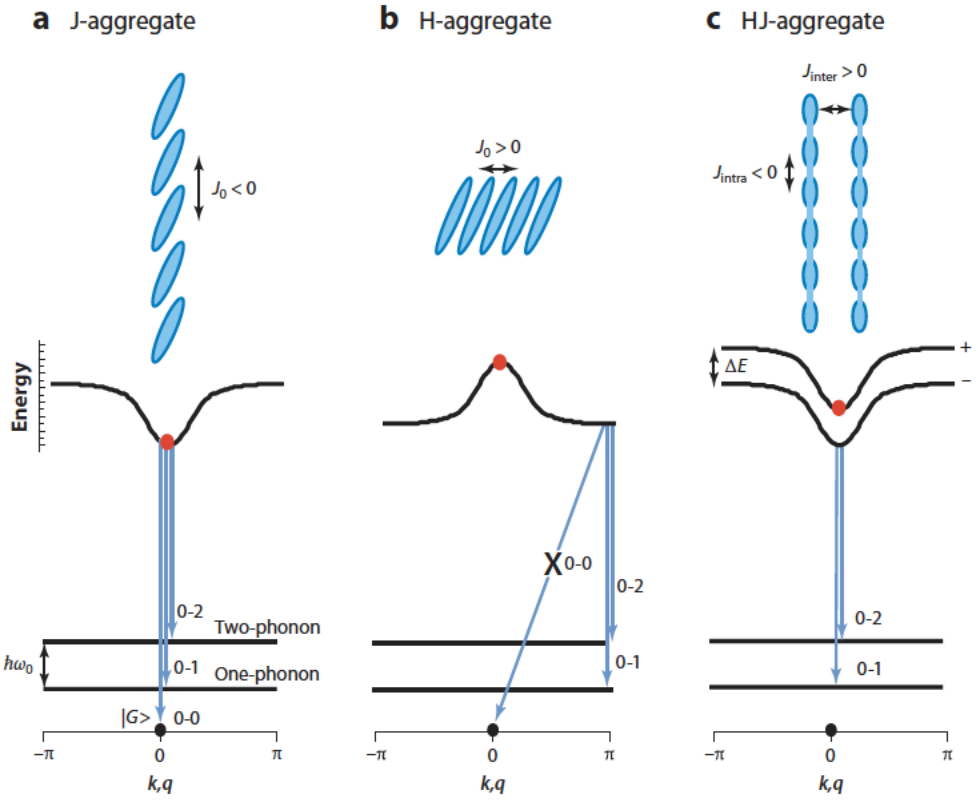

Figure 1.3 *Orientations of J-, H- and HJ-aggregates and corresponding energy band diagrams. Reproduced with permission from Ref.*[38] *Copyright (2014) Annual reviews, Inc.*

Kesha's model is very successful in understanding the distinguished fundamental difference between J- and H-aggregate of dyes. However, it also has obvious limitations especially on the interpretation of more complicated conjugated polymer aggregates. The vibronic coupling between electronic transition with vibrational transitions such as vinyl/ring stretching in P3HT is omitted. Recognizing both the significance and limitations

of Kesha's model, Spano proposes a more specific model of weakly interacting H-aggregates, incorporating vinyl/ring stretching mode with vibrational energy $\hbar\omega_0$ into the existing 1D exciton model of side by side H-aggregates from Kesha, while omitting intrachain coupling of the excitons.[41] This model focuses on the interpretation of optical properties of conjugated polymer aggregates prepared from conventional solution-casting methods such as regioregular P3HT films spun from low boiling point solvent.[41, 45] The absorption spectrum can be deconvoluted into a larger wavelength (lower energy) domains ascribed to the H-aggregates with weak interactions and a lower wavelength (higher energy) domain attributed to the contribution from more disordered chains, in another word, the non-aggregation states of conjugated polymers.[40] Due to energy dispersion relationship in periodic potential boundary conditions, nearest-neighboring intrachain Coulombic coupling of aggregates can be written as a function of wavenumber *k*,

$$J_k = 2J_C \cos k \qquad \text{(Eq. 1.3)}$$

If interchain exciton bandwidth *W* is defined as the difference of J_k between k = 0 and k = π, due to the energy dispersion relationship, *W* can be written as,

$$W = |J_{k=0} - J_{k=\pi}| = 4J_C \qquad \text{(Eq. 1.4)}$$

Assuming a Huang-Rhys factor of unity, the ratio of oscillator strengths of two major absorptions peaks, the 0-0 and 0-1 vibronic transitions can then be correlated to the interchain exciton bandwidth *W* as follows,[37, 40, 41]

$$\frac{A_{0-0}}{A_{0-1}} \approx \left(\frac{1 - \frac{0.24W}{\hbar\omega_0}}{1 + \frac{0.073W}{\hbar\omega_0}} \right)^2 \qquad \text{(Eq. 1.5)}$$

where the $\hbar\omega_0$ is the energy associated with the main intramolecular vibration such as vinyl/ring stretching in P3HT. If the ratio is lower than 1, meaning the transition of 0-0 is suppressed and the aggregates are H-type. Conversely, if the ratio is close to 1, the aggregates are J-type. This signature ratio in the absorption obtained experimentally can also be used to extracted exciton bandwidth *W* of conjugated polymer aggregates derived from various conditions.[39, 45] Due to the difference in the sign of Coulomb coupling (J_C), this ratio increases with *W* in J-aggregates, while it decreases with *W* in H-aggregates, thus, it can be regarded as a useful index for the determination of the crystalline degree of conjugated polymer aggregates within thin films. As for the photoluminescence (PL) spectrum, it is directly correlated to two parameters. First, the thermal disorder, which can be represented by the width of the Gaussian distribution of the energy of state as σ. Second, the intra-aggregate disorder can be characterized by a spatial correlation length l_0. The ratio of the 0-0 and 0-1 emission oscillator strengths are shown as,[37, 38, 40]

$$\frac{I_{0-0}}{I_{0-1}} \approx \frac{(1 - \beta)\sigma^2}{(1 + \beta)W^2} \qquad \text{(Eq. 1.6)}$$

in which $\beta = \exp(-1/l_0)$. When the aggregates are free from either thermal disorder ($\sigma = 0$) or intra-aggregate disorder ($l_0 = \infty$) the 0-0 emission completely disappears. Typically, with a fixed thermal disorder, this ratio decreases with increasing intra-aggregate disorder β (decreasing l_0). As shown in Figure 1.4, when the intra-aggregate order is high ($l_0 = 100$), the 0-0 is strongly suppressed and almost unnoticeable, while if l_0 approaches zero, the maximal intra-aggregate disorder results in an unsuppressed 0-0 emission.

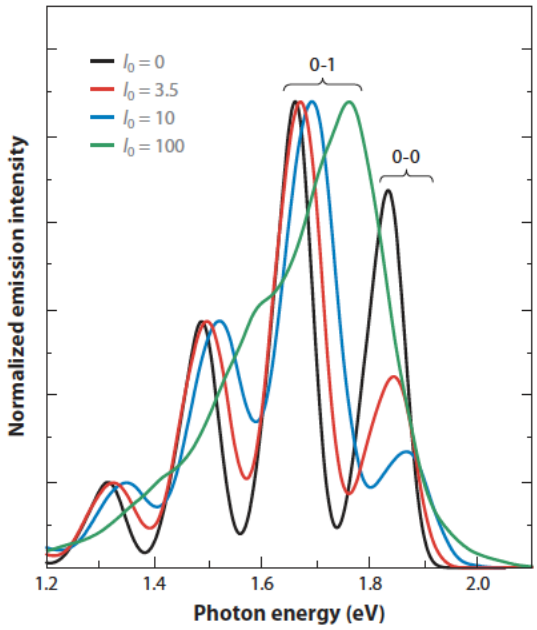

Figure 1.4 *Simulated PL spectra of weakly interacting H-aggregates of P3HT π-stacks. Reproduced from Ref.*[34]*, with the permission from AIP publishing.*

Note: The calculation involves 100 P3HT chromophores. Peak intensities are normalized to the 0-1 line strength. σ = 0.08 eV.

On the other hand, the interaction between chromophores only accounts for the through space Coulombic coupling, while the intermolecular charge transfer induced by wave function overlap of adjacent chromophores (typically 3.5 ~ 3.8 Å[46]) is also neglected. At the same time, intermolecular Coulombic coupling do not always dominate like in typical weakly interacting H-aggregates derived from spin-coating. In some exotic J-aggregates, due to increasing intrachain conjugation length, intrachain Coulombic coupling might dominate. Therefore, a more generic description of the vibronic transitions of conjugated polymer aggregates would be that the ultimate property of conjugated polymer aggregates depends on the interplay between intrachain electronic coupling and interchain coupling. As a result, instead of treating π-π stacking conjugated polymer aggregates as a 1D exciton system in Kesha's model, it should be treated as two-dimensional excitonic

systems, where excitations can be delocalized not only along a single chain of polymer but also between adjacent chains.[38, 42] The intrachain excitons are shown to be of the Wannier-Mott type, in which charge carriers can be transported up to several monomer units. On the other hand, the interchain excitons are Frenkel-type excitons as charge separation is limited to adjacent chains.[38, 42] Recently, P3HT in the form of nanofibers has been prepared by slowly cooling the P3HT in a marginal solvent such as toluene. The formed nanofiber is with strong J-type characteristics, showing dominant 0-0 emission and absorption, which breaks down the classic model of weakly interacting H-aggregates.[47] To account for the stronger intrachain interactions caused by increasing intrachain order and larger conjugation length of the polymer chain, Spano et al. proposed a so-called HJ aggregate model. This model seems to explain the enhanced 0-0 transitions of the J-aggregates well. [42] Due to the limited scope, the details of this model are not presented herein. Since the molecular aggregates involved in this thesis are mainly prepared by the spin-coating method, the pre-existing weakly interacting model developed by Spano et al. will be frequently referred to and used.

1.2.2 Semi-Crystalline Structures of Conjugated polymer aggregates: Using Example P3HT

As mentioned earlier in the spectroscopy of conjugated polymers, the driving force of π-π interaction facilitates the formation of self-assembled conjugated polymer aggregates. In general, the formed aggregates can exhibit various crystal packing motifs, classified by the angle between the transition dipole moment and the packing direction, as shown in Figure 1.5. Unlike small conjugated molecules with bare conjugated cores such

as pentacene, tetracene, perylene diimide, and quaterthiophene, in which 2D motifs like herringbone packing are favored,[48, 49] conjugated molecules with various side-chain substituents like halogen atoms, alkyl and/or aryl chains, etc., tend to form 1D motifs such as H- or J-aggregates. As a result, typical conjugated polymers with alkyl side chains such as P3HT prefer the formation of H- and J-aggregates as well.

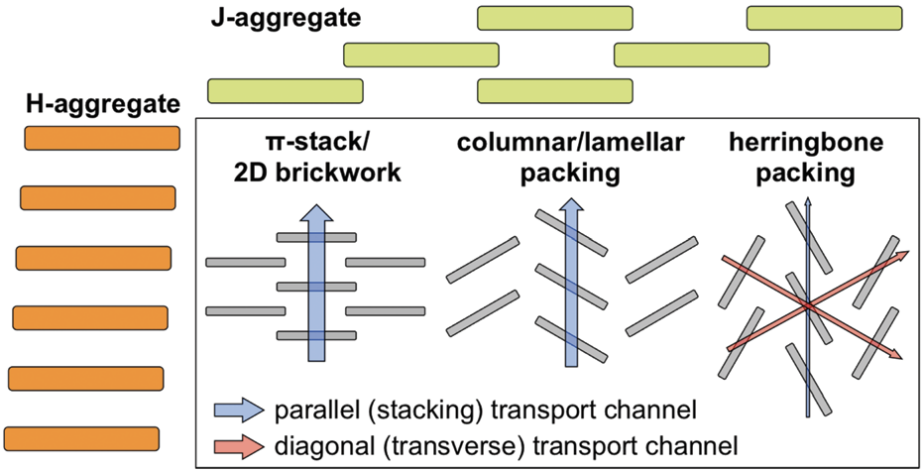

Figure 1.5 *Generic crystal packing motives of the conjugated molecules. Reproduced with permission from Ref.[48] Copyright (2017) Royal Society of Chemistry.*

From the perspective of crystallography, there is a different way to define the molecular ordering of conjugated polymers based mainly on XRD diffraction and STEM. As shown in Figure 1.6, the P3HT crystal can grow in three dimensions. In b-direction, P3HT assembles via π-π interaction, and the spacing between π-stacks is about 0.38 nm for P3HT. On the other hand, P3HT can also assemble along chains (c-direction) via van der Waals interaction. In such a way, highly ordered π-stacks can be interconnected by disordered regions. In a-direction, P3HT forms ordered lamella region via alkyl-alkyl van der Waals interaction with a finite interlayer thickness. In general, two types of crystalline structural models have been assigned due to the difference in interlayer thickness, which

are Form I and Form II. As has been well summarized by Brinkmann[46] and Su et al.,[50] in Form I structure, the interlayer distance in the direction of the side chain (the a-direction has shown in Figure 1.6a) of P3HT crystalline is about 1.6 nm from the earlier electron diffraction works of multiple groups.[51-53] While in Form II structure, the interlayer spacing of the organized lamellar is about 1.2-1.3 nm,[54-56] which is significantly shorter than it in Form I. It is well accepted that the shortening can be explained by the interdigitation of side chains in Form II.[46, 50, 55, 56] The difference between lattice constant (a) of Form I and Form II is independent of Mw of polythiophene (Figure 1.6b), indicating that it is caused by the interdigitation of side chains.

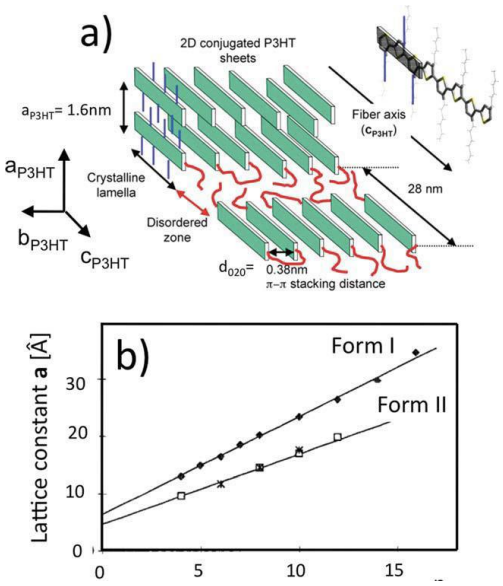

Figure 1.6 *(a) Schematic model that exhibits the self-assembling structure of the semicrystalline P3HT, where a, b, and c represent the lattice parameter in the corresponding lattice directions, (b) Lattice constant (a) as a function of Mw of P3HT. Reproduced with permission from Ref.[46] Copyright (2011) John Wiley and Sons.*

The crystallinity of conjugated polymers has a critical role in determining the charge transport properties of conjugated polymer aggregates. If the impurities/defects can

not be ignored in highly crystalline aggregates, which is very common in a real-world sample, the impedance of the charge carrier motion along the chain direction needs to be taken into consideration. Meanwhile the carrier motion that occurred between adjacent chains in the π-stacking direction is another major channel for charge carrier transport.[57] Last, the side chain direction in the lamella region along a-axis in Figure 1.6a has the largest impedance and are often regarded inaccessible for charge transport since alkyl chains are insulators. Thus, the charge carrier is largely dominated by interchain transport in b-direction and interchain transport in c-direction, which forms a 2D transport channel. Although it is possible to obtain conjugated polymers as single crystals,[54, 58, 59] it requires extensive control on the parameters in the crystallization process such as concentration, temperature, and cooling rate. CPs in the form of polycrystalline materials is more ubiquitous due to the use of common processing techniques such as spin-coating, drop-casting, and ink printing, etc. Thus, optimizing the morphology of regioregular CPs to minimize the impedance of carrier transport becomes a rational direction. It has been observed by Kline et.al[60-62] in polycrystalline regioregular P3HT thin films that the mobility of charge carriers highly depends on the orientations of crystallites. It is defined that "edge-on" represents the orientation where the thiophene ring plane is perpendicular to the surface while "face-on" stands for the scenario when the thiophene ring plane is parallel to the surface (Figure 1.7). It is not difficult to imagine when "edge-on" orientation occurs, the measured charge transport is mainly governed by the b-direction channel. On the other hand, if "face-on" occurs, the charge transport must be dominated by the c-direction channel.

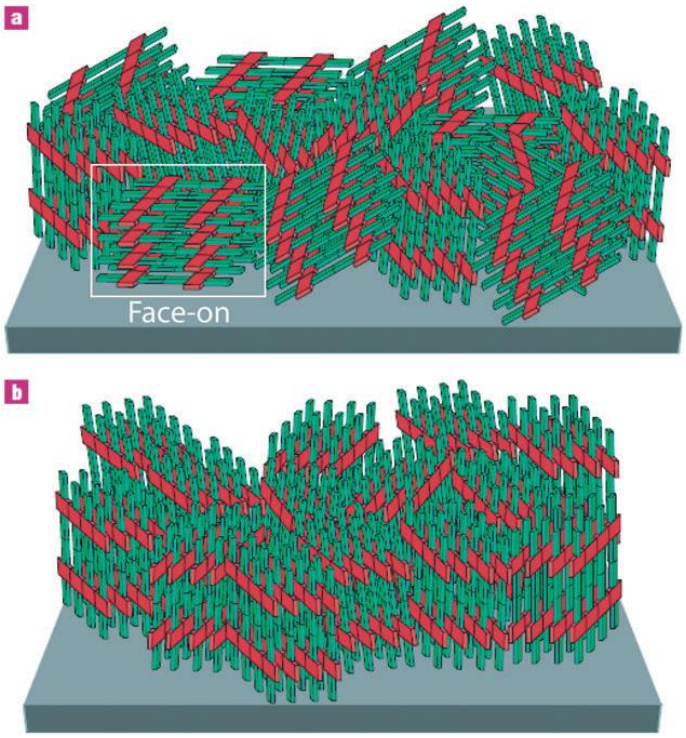

Figure 1.7 *(a) Coexisting of face-on and edge-on orientations in a typical spin-coating sample of regioregular P3HT. (b) Preferred orientation with all edge-on arrangement. Reproduced with permission from Ref.*[62] *Copyright (2006) Springer Nature.*

If the orientation of a thin film can be uniform, in general, either all in edge-on or face-on orientation, the charge transport can be greatly facilitated due to the interconnection of conductive domains. However, in a practical sample, there is always some coexisting of edge-on and face-on, resulting in the grain boundary between edge-on and face-on orientation connected by insulating alkyl side chains, which sharply reduces carrier mobilities. Thus, a classic approach to increase charge transport of conjugated polymers is to minimize the presence of grain boundary between face-on and edge-on crystallites.[57, 62] In other words, processing parameters of film preparation should favor the formation of either edge-on or face-on orientation. On the other hand, the preference on the orientations of crystallites also depends on specific applications. For example, in OECT

devices, high in-plane charge transport mobility between source and drain electrodes is demanded, while in OSC device, charge transport in the vertical direction with respect to the surface of a substrate is decisive to separate photogenerated excitons.[46] In the former case, edge-on orientation with "in-plane" π stacks is preferred. Yang et al. show that edge-on P3HT film (μ = 0.01 cm^2 V^{-1} s^{-1}) has 10 times higher hole mobility than face-on P3HT film, given both films are prepared from spin-coating.[63] Some semi-empirical rules have been established as guidelines for the orientation preference on edge-on or face. For instance, the edge-on orientation of P3HT is preferred when some experimental conditions are met such as the use of higher boiling solvents[46] and the surface passivation of the SiO_2/Si substrates by organosilanes such as octadecyl trichlorosilane (OTS) and hexamethyldisilazane (HMDS),[62, 64] while mostly face-on orientation can be observed in P3HT films spin-coated from solutions in $CHCl_3$.[63] Chang et al. proves that 10 folds higher hole mobility ((μ = 0.12 cm^2 V^{-1} s^{-1}) in OECTs can be achieved by using solvents like 1,2,4-trichlorobenzene rather than $CHCl_3$.[65] However, this kind of simple "selection rules" can be laden with exceptions. For example, Yang et al. use the drop-casting method to prepare P3HT films for OECTs. The results show that P3HT films derived from low boiling point solvents like THF or $CHCl_3$ are of a higher degree of crystallinity and higher hole mobility than the films prepared from the higher boiling point solvent such as toluene.[66] All these results demonstrate the complicity of the convolution effects of solvent type, surface passivation, and casting method on the final orientation and crystallinity of P3HT microstructures within a benign film. It is worthwhile to mention that higher crystallinity does not always lead to high hole mobility. Kline et al. use combined results obtained from

AFM and grazing incidence X-ray scattering (GIXS) to show that the low M_W (4 kDa) films are composed of highly ordered nanorods interconnected with disordered domains, as shown in Figure 1.8a.[60, 61] High M_W (34 kDa) films, however, have a less ordered, isotropic overall morphology (Figure 1.8b). The inferior hole mobility of low M_W sample is caused by a combination of hole trapping effect brought by disordered domain boundaries and inherent electronic effects of chain length.[60, 61] They claim that domain boundaries formed in the low Mw P3HT films are either voids or disordered regions due to the rigidity of shorter polymer chains.[61] Neher et al. propose another model against it,[67, 68] while later on, it seems that they adopt Kline's theory.[69] This result again indicates that minimization of grain boundary to ensure charge transport channel is the priority to improve the performance of OECTs, even surpassing the importance of creating highly packed crystalline domains within a film.

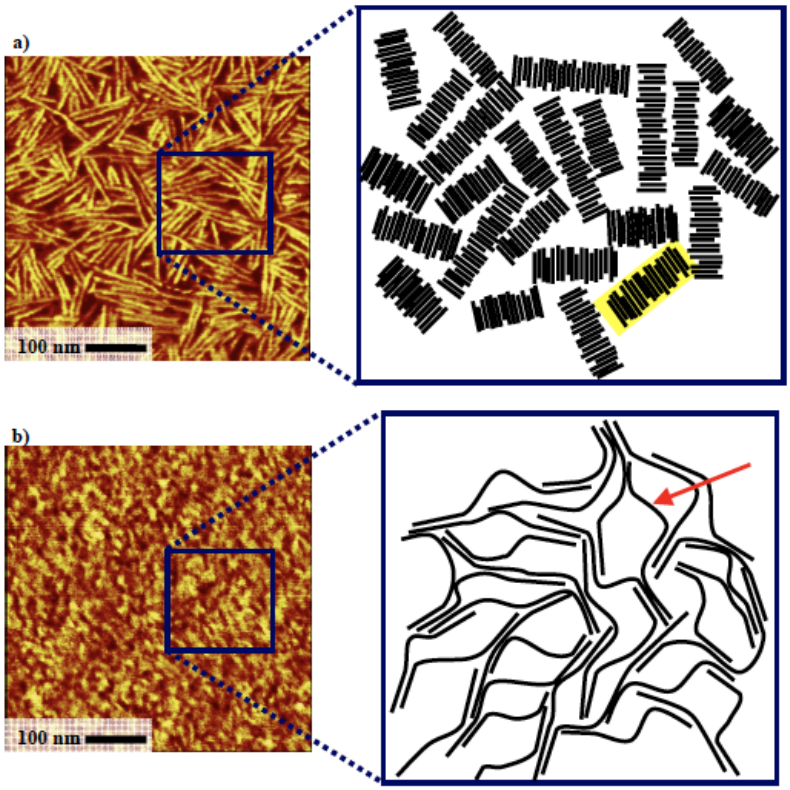

Figure 1.8 *Hole transport modes in low (a) and high-MW (b) P3HT films. Reproduced with permission from Ref.*[61] *Copyright (2005) American Chemical Society.*

Interestingly, there is not much cross-talking on the ordering of conjugated polymers defined by spectroscopy and crystallography. In another word, not much work has been done to elucidate the difference in charge transport properties of H- and J-aggregate. Due to the co-facial π-π stacking in H-aggregates, parallel charge transport channel is more available along the packing direction in H-aggregates, and the interchain hopping of charge carrier is enhanced, thus, it is generally believed that the mobility of charge carrier in small molecule H-aggregates such as quaterthiophene can be one to two orders of magnitude higher than the J-aggregate counterparts.[48, 70] From the existing knowledge of small molecule aggregates, it is reasonable to assume H-aggregates are better

in charge transport than J-aggregates. However, to this date, there is still a lack of a method for the preparation of macroscopically uniform J-aggregate samples. For example, J-aggregates of P3HT can only be in a diluted and isolated nanofiber form by controlling aging in a particular marginal solvent, toluene.[47] The difficulty in making a measurable macroscopic device hinders the direct comparison of its charge transport properties with a readily available thin film of H-aggregate P3HT.

1.3 Chemical doping of Conjugated Polymers

Chemical doping is a promising way of enhancing electrical properties such as the conductivity of organic semiconductors. The electrically enhanced doped materials have shown great promise as charge transport and injection layers in the applications of novel organic electronic devices.[71-73] Most recently, doped OSCs have been applied as thermoelectric materials due to their high figure of merit (ZT).[74-77] However, despite the success of the devices, concerns need to be addressed in terms of its long-term stability. Meanwhile, there is also a lack of fundamental understanding on how to control its charge carrier transportation so that the conductivity of doped materials can be toned. Therefore, there is a great necessity to study the doping of conjugated polymers, from both fundamental and practical points of view.

1.3.1 Doping Mechanisms

According to a comprehensive review by Lussem et al., dopants for the doping of conjugated polymers include several different categories such as small molecules, polyelectrolytes, covalent solids, Brønsted and Lewis acids, and even elemental species like O_2 and halogen gases.[3] In terms of P3HT, p-doping is available since the majority

carrier in P3HT is a hole, which increases the hole density and conductivity of the material. To facilitate effective doping, a strong dopant with relatively high electron affinity (EA) is required, typically larger than 4.5 eV, to ensure electron transfer from the donor conjugated polymers to the dopants. Among all possible candidates, small molecular dopants attract the most interest due to their tunable electron affinity upon structural modifications. Extensive research has been done on the doping of P3HT films,[78-81] either in its polycrystalline or amorphous form. For example, 2,3,5,6-tetrafluoro-7,7,8,8-tetracyanoquinodimethane (F_4TCNQ) can be used as a typical electron acceptor for p-doping of P3HT due to its high EA of 5.24 eV.[82, 83]

Two electron transfer models exist for the explanation of donor-acceptor interaction between conjugated polymers and dopants after the proceeding of doping reactions. As shown in Figure 1.9a, in the so-called integer charge transfer model, the electron is 100% transferred from P3HT to the F_4TCNQ. The transferred electron is assumed to be restrained at the vicinity of F_4TCNQ while the associated hole is either tightly bound to the F_4TCNQ^- anion via Coulombic interaction or exists as a free hole in the P3HT domain. Due to the presence of binding effect caused by Coulombic interaction, the free hole density is much lower than the dopant concentration. In another word, the doping efficiency is much less than 100%. According to Pingel et al.,[84] the doping efficiency of P3HT/F_4TCNQ can be less than 5%, which means only 5% of the F_4TCNQ dopants are converted into free holes. On the other hand, a co-existing model called the hybrid charge transfer model is shown in Figure 1.9b. Frontier molecular orbital hybridization between the HOMO of donor and the LUMO of dopant is supposed to happen, resulting in the formation of a new set of frontier

molecular orbitals, called charge-transfer complex (CTC).[85-87] This new set of frontier molecular orbitals has a lower bandgap between an occupied bonding orbital and a corresponding unoccupied antibonding orbital.

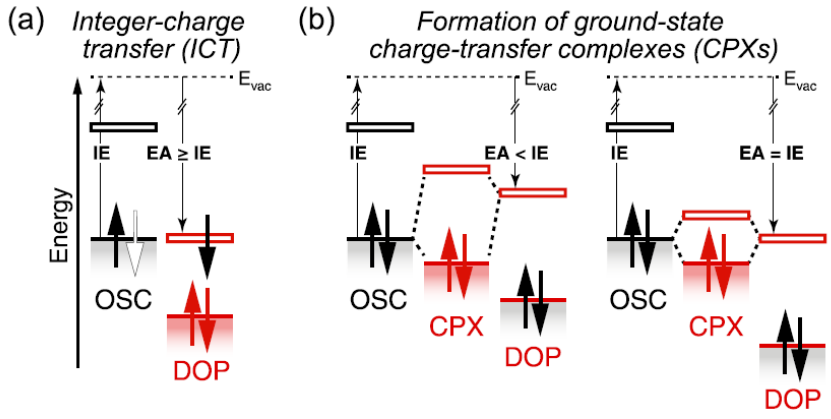

Figure 1.9 *(a) Integer charge transfer model, assuming complete ionization of donor and acceptor. (b) Hybrid charge transfer, showing the formation of hybrid supramolecular charge transfer complex (CTC) orbitals. The electrons in the HOMO of donor are transferred into the bonding orbital from the hybridization of HOMO (donor) and LUMO (acceptor). Reproduced with permission from Ref.[88] Copyright (2015) Elsevier.*

It is important to distinguish several definitions here to clarify the concept around the "efficiency" of doping, which can be misleading in some literature with other terminologies such as doping ratio or percentage of doping. Typically, doping ratio (DR) indicates the molar ratio between dopant and monomer of a conjugated polymer, which can be an arbitrarily large number from 0 to 100%. Meanwhile, the percentage of dopant undergoes charge transfer reaction with conjugated polymer, which is known as the ionization degree of the dopant, is about 50%-70% regardless of doping in solution or within a film.[84] After that, most of the holes created are still tightly bound to the anion, resulting in a minor number of free charge carrier. Thus, the general expression for doping efficiency (DE) should be,

$$\mathrm{DE} = \mathrm{DR} \times \text{Ionization degree} \times \text{Percentage of free holes} \qquad \text{(Eq. 1.7)}$$

Doping efficiency is not close to the doping ratio at all. Due to its lower value, doping efficiency can be viewed as a bottleneck to further enhance the doping of conjugated polymers.

To distinguish which model is suitable for the doping of conjugated polymers such as P3HT, multiple approaches have been made. Inspired by the observation on the unchanged ionization percentage of F_4TCNQ in solution and within a film, Pingel et al proposed that the majority of dopant F_4TCNQ should adopt integer charge transfer when interacting with P3HT.[84] On the other hand, UV-Vis results from Mendez et al. directly show that only ICT peaks belong to F_4TCNQ anions can be observed at around 1.5 eV in P3HT/ F_4TCNQ spectrum, with no adsorption peaks of CTCs in the NIR region below 1 eV. While the NIR adsorption of CTCs can be observed in small molecules doped with F_4TCNQ such as quaterthiophene (4T).[87] Using FTIR spectroscopy, Neelamraju et al. propose that the relative fraction of CTC correlates with the microstructure of the film. In P3HT films derived from regioregular P3HT, ICT is much preferred than CTC.[89] Clearly, it seems that intermolecular frontier orbital hybridization is much more prominent in small conjugated molecules than in conjugated polymers. However, little progress has been made to explain this phenomenon, there is still a lack of fundamental understanding on the preference of charge transfer model based on a clear molecular orbital picture.

1.3.2 Changes in the Electronic Property of Conjugated Polymers after Chemical Doping

Obviously, the electronic structure of the conjugated/dopant pair is altered by performing chemical doping. One major characteristic of doping is that it can change the work function of the conjugated polymer matrix via electron transfer from donor to acceptor. Neher's group observe a significant upshift of the work function of P3HT only occurs on low work function substrates such as aluminum due to the formation of classic Schottky contact between P3HT and aluminum, while little change can be found on other substrates with higher work function larger than 4.5 eV such as copper.[84] This result implies doped P3HT might be a good work function modifier as long as low work function metal is used as an electrode (Figure 1.10). Similarly, Fehlman's group also find abrupt upshifts in the work function of P3HT on various substrates with work function ranging from 3 eV to 5 eV.[90]

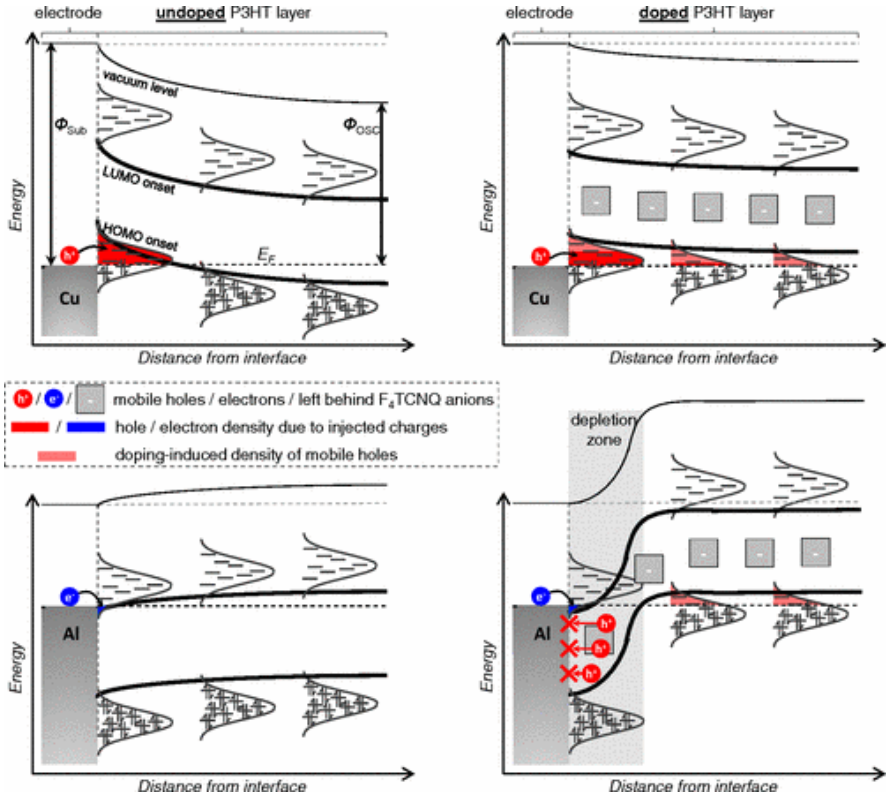

Figure 1.10 *Electron or hole transfer of undoped (left) and doped (right) of P3HT films on different metal substrates. Reproduced with permission from Ref.*[84] *Copyright (2012) American Physical Society.*

On the other hand, doping of conjugated polymers increases free charge carrier concentration. As mentioned earlier, the doping efficiency of P3HT is far lower than the doping ratio. Despite limited doping efficiency, the increase of free charge carrier concentration can still be significant due to the low number of intrinsic charge carrier before doping. As shown in Figure 1.11a, hole concentration increases linearly with the doping ratio. Meanwhile, the conductivity (σ) of P3HT film also increases accordingly, but in a more complicated manner.[91]

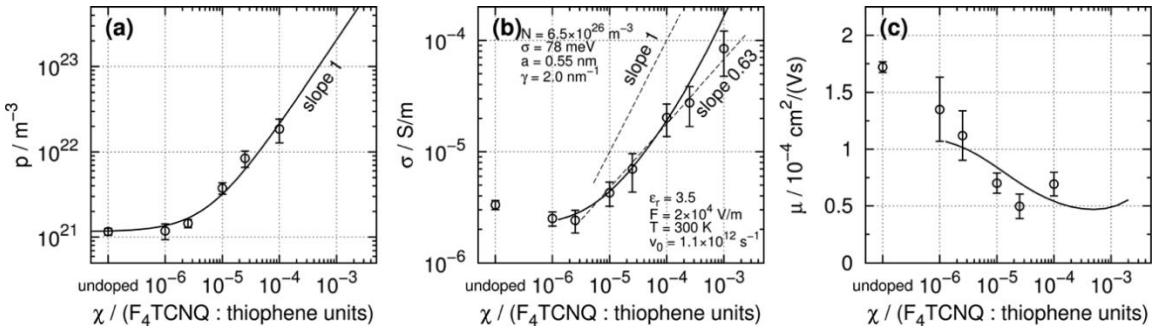

Figure 1.11 *(a) Hole concentration of P3HT films as a function of doping ratio. (b) Conductivity as a function of doping ratio. (c) Hole mobility as a function of doping ratio. Solid lines indicate linear fittings. Reproduced with permission from Ref.*[91] *Copyright (2012) American Physical Society.*

It can be seen from Figure 1.11b that at low doping ratios ($\chi < 0.01\%$), a sublinear increase of the conductivity exhibits. While at higher doping ratios ($\chi < 0.1\%$), the increase of conductivity follows a linear pattern. Since bulk conductivity is proportional to the product of hole concentration and hole mobility. Pingel et al. explain that the sublinear increase of conductivity is probably due to the sharp decrease of hole mobility (Figure 1.11c), which offsets the increase of hole concentration.[91] This negative contribution to the conductivity becomes weaker as hole mobility is stabilized in a higher doping ratio as shown in Figure 1.11c, so that the linear increase of conductivity as a function of doping ratio is ensured. However, despite the successful explanation on the trend of conductivity, the reason for the initial sharp decay and later stabilization of hole mobility is still unknown. Duong et al. examine doping ratios much higher than the regime Pingel et al. adopted. They observe that a maximal in-plane conductivity of doped P3HT films is achieved at a doping ratio of 17%, which leads to the conductivity of ~1 S/cm.[81] Two separated doping regimes are proposed. At doping ratio lower than 3%, it is named after "weak doping regime", where dopant resides in amorphous region of P3HT film. The

"strong doping regime" refers to the doping ratio larger than 3%. According to their results, it seems the doping efficiency is much higher in a strong doping regime than a weak doping regime by 2-3 orders of magnitude. However, the parameter used for the evaluation of concentration (c) dependent conductivity (σ), $d\sigma/dc$, completely omits the contribution from hole mobility. Therefore, the true trend of doping efficiency and hole mobility upon elevated doping ratio ($\chi > 1\%$) remains unclear. Despite this, it is generally observed that doping of P3HT by F_4TCNQ can greatly improve the conductivity of P3HT by $10^3 \sim 10^4$ times.[92] Thus, chemical doping is widely accepted as a practical route to tune the electrical conductivity of conjugated polymers.

1.3.3 Doping Methods

Multiple approaches can be made for the doping of conjugated polymers. Generally, it can be performed via solution doping,[78, 81, 84, 91] vapor doping[76, 93-96] and sequential doping.[80, 97-99] Solution doping can be referred to as the process, where a dopant solution is mixed with a solution of conjugated polymer for the proceeding of charge transfer reaction in a solvent. After the reaction, the resultant doping products can be spin-coated onto a suitable substrate to form a doped polymer film.[84, 91] As for vapor processing, it is a technique widely applied historically. In fact, doping of the very first few conjugated polymers, polyacetylene, was accomplished by iodine vapor, as shown by the early work by Shirakawa, Heeger, and MacDiarmid.[15, 100] In terms of vapor doping of P3HT, F_4TCNQ is frequently used as a vapor source for doping.[75, 76, 93]As shown in Figure 1.12, dopant molecules can sublime upon heating and infiltrate into the target composed of conjugated polymer.[76]

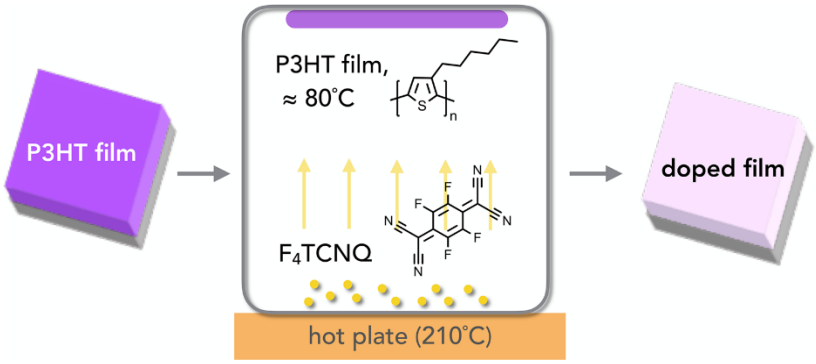

Figure 1.12 *Schematic representation of vapor doping technique using P3HT/F$_4$TCNQ as an example. Reproduced with permission from Ref.*[76] *Copyright (2018) American Chemical Society.*

Similarly, in sequential doping, the benign conjugated polymer film is casted prior to the deposition of dopant from an orthogonal solvent such as acetonitrile by spin-coating or dip-casting (Figure 1.13).[97] Note that "orthogonal" means the solvent conveying dopant is not dissolving the underlying polymer layer, which makes it possible to retain the high crystallinity of the film. In sharp contrast to the scenario of sequential doping, in solution doping, where highly doped conjugated polymer forms agglomerates in an organic solvent, it is very difficult to spin-coat a homogeneous polymer film for electrical measurements.[97-99] This explains why doped films from sequential doping are much higher in conductivity than the ones prepared by solution doping.[97] Like sequential doping, vapor doping also preserves crystallinity of initial conjugated polymer film since solid-state diffusion of a dopant such as F$_4$TCNQ has little perturbation on the microstructure.

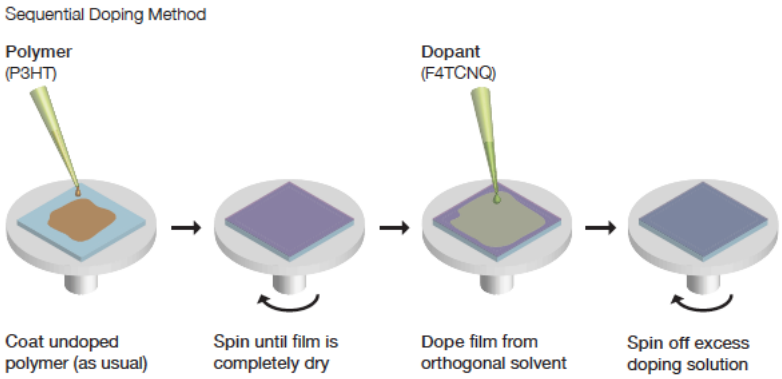

Figure 1.13 *Schematic representation of sequential doping technique using P3HT/F₄TCNQ as an example. Reproduced with permission from Ref.*[97] *Copyright (2016) Royal Society of Chemistry.*

To date, the highest conductivities of doped P3HT films are achieved either by vapor doping or sequential doping. A typical highly conductive doped P3HT film can reach a conductivity between ~1 S/cm to ~10 S/cm.[96-98]

1.4 Organic Electrochemical Transistors (OECTs): Control Doping of Conjugated Polymers by Manipulating Ion Injections

The ever-developing of biomedical research nowadays demands high performance, flexible, cost effective, and bio-compatible material solutions for various purposes such as bio-sensing, bio-signal recording, and even functional implant devices.[101] Since the original prototype based on conjugated polymers developed by White and Wrighton,[102] there is an increasing research interest in a specific kind of transistor device called organic electrochemical transistor (OECT).[103] Nowadays, OECT devices are generally composed of conductive polymer active channel, aqueous electrolyte, and a reference gate electrode. The most popular active channel choice is PEDOT:PSS. The drain-source current of the PEDOT:PSS layer can be modulated by varying gate bias and changes in the chemical environment of the electrolyte layer. Thus, they are regarded as potential candidates for

biomedical applications including disease diagnostics and cell-interfaced implants due to their flexible nature and excellent biological compatibility with biological tissues.[104-106] On the other hand, this novel OECT device configuration not only shows better biological compatibility as compared to conventional silicon-based electronic devices, but it also exhibits superior electronic properties.

1.4.1 Operation principles of OECTs devices

A typical device configuration of PEDOT:PSS based OECT is shown in Figure 1.14. After extensive lithography work, a micropattern made up of a pair of gold electrodes is created on a substrate such as parylene. A layer of PEDOT:PSS can be deposited on a patterned gap between the pair of gold electrodes. On top of PEDOT:PSS, an aqueous solution is loaded as an electrolyte layer while a reference electrode, typically Ag/AgCl, is immersed into the solution. Due to the highly doped nature of PEDOT:PSS, it is highly conductive if no gate bias is applied. Therefore, the OECT based on it operates in depletion mode. When a gate bias is not engaged, i.e $V_g = 0V$, the drain-source current is "on" since the amount of mobile hole is unchanged. When a positive gate bias is engaged, cations such as Na^+ in the electrolyte solution are expelled from the gate electrode and injected into the PEDOT:PSS film, which depletes the mobile hole in the film through the drain. The higher gate bias is applied, the more hole gets depleted, which results in a lower drain-source current.

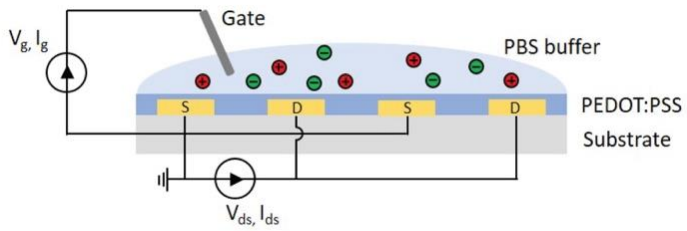

Figure 1.14 *Schematic representation of an OECT device.*

Despite this doping/de-doping mechanism seems to be unique, the outcome of it results in a resembling transfer (V_g-I_{ds}) curve as compared to conventional field-effect transistor under depletion mode. *Vice versa*, an inverted principle governs OECTs in accumulation mode. However, it is worthwhile to point out that the operating voltage of the OECT device is well below 1V. This can be attributed to the unique doping/de-doping mechanism of OECT, while at the same time, it prevents redox reaction of water above 1V, bringing additional benefit in potential *in-vivo* low voltage application.

To characterize the amplification in the drain current caused by variation of gate voltage, a figure-of-merit called transconductance $g_m = \Delta I_{ds} / \Delta V_g$ is defined as a key parameter to evaluate the performance of field-effect transistor devices. Surprisingly, the OECTs exhibit highest transconductance values on the record at about 4020 μS, surpassing any materials including newly discovered ones such as graphene.[105] Thus, it attracts more research attention to fully exploit the great potential of OECTs. In the next section, details on the device physics of OECTs will be introduced.

1.4.2 Fundamentals of Organic Electrochemical Transistors (OECTs)

The theory of OECTs derived from a medication of conventional field-effect transistor stems from the early work by Bernards et al.[107] The drain current I_{ds} flows

through a cross-section of the semiconducting active layer, where the channel width is *W* and channel thickness is *d*, can be written as follow,

$$I_{ds} = W \cdot d \cdot e \cdot \mu \cdot p(x) \cdot E = W \cdot d \cdot e \cdot \mu \cdot p(x) \cdot \frac{dV_{ds}(x)}{dx} \qquad \text{(Eq. 1.8)}$$

where *E* is the electrical field, μ is the hole mobility and p(x) represents the density of charge carrier, holes. As the most significant feature of OECTs, the hole density is originally compensated by the anions within the semiconducting layer $[A]_0$, which later can be changed by the ion injection upon applying a gate voltage V_g. Suppose the injected ions are cations, the hole density affected ion injection is as follows,

$$p(x) = [A]_0 - [C]_{injected} = [A]_0 - (\mathrm{C}^*/\mathrm{e})\left[\mathrm{V}_g - \mathrm{V}(\mathrm{x})\right] \qquad \text{(Eq. 1.9)}$$

In this expression, it is clear that the concentration of injected ions is controlled by a critical parameter, which is the volumetric capacitance of the OECTs, C^*. Combine the two equations above and integrate over the length of the channel *L*, the expression for drain current I_{ds} can be re-written as,

$$I_{ds} = \left(\frac{Wd}{L}\right)\mu\mathrm{C}^*\left(V_T - V_g + \frac{V_{ds}}{2}\right)V_{ds} \qquad \text{(Eq. 1.10)}$$

where V_T is the so-called threshold voltage and $V_T = e[A]_0/\mathrm{C}^*]$. Note that the equation only strictly works in the linear regime, where $V_{ds} << V_g - V_T$. In the saturation regime ($V_{ds} > V_g - V_T$), the drain current I_{ds} ideally remains independent from V_{ds},

$$I_{ds}^{sat} = \left(\frac{Wd}{2L}\right)\mu\mathrm{C}^*\left(V_T - V_g\right)^2 \qquad \text{(Eq. 1.11)}$$

To characterize the performance of an OECT via estimating its hole mobility μ, the first derivative of the I_{ds} with respect to V_g can be taken, resulting in the so-called transconductance (g_m),

$$g_m = \frac{\partial I_{ds}}{\partial I_g} = \frac{Wd}{L} C^* \mu \left(V_g - V_T\right) \qquad \text{(Eq. 1.12)}$$

By plotting g_m as a function of V_g, the hole mobility μ can be readily available from the interpretation of the slope.

1.5 Experimental techniques

For the study on the doping of conjugated polymers, a holistic approach is required to establish the relationship between its morphology and property. Due to the unique alternating carbon-carbon double bonds in conjugated polymers, the UV-Vis spectra of pristine CPs often show distinctive features in the visible range, which explains the sharp colors CPs often have. However, the formation of polaron/bipolaron due to the doping of the polymers can "bleach" the color of the pristine CPs. On the other hand, the spectroscopical method can be coupled with AFM techniques to study morphological evolutions upon doping. In the end, electrical measurements can be performed to test out the effect of doping on the performance of a real device and its electrical properties.

1.5.1 Fundamentals of UV-Vis Spectroscopy

To start with UV-vis spectroscopy, Beers-Lambert needs to be introduced. The law explicitly correlates optical transmittance (T) or absorbance (A) of a material with the product of the concentration of the material (c) and to the optical path length (l) by a molar extinction coefficient (ε). The expression can be shown as follow,

$$A = -Log(T) = -Log\left(\frac{T_t}{T_0}\right) = \epsilon cl \qquad \text{(Eq. 1.13)}$$

in which T_0 is the incident light intensity and T_t is the transmitted light intensity. It is clear to recognize that the higher of εcl, the larger light absorbance occurs. Generally, the product of cl is independent of material. Therefore, the key parameter for the interpretation of the UV-vis spectrum is the molar extinction coefficient ε. Fundamentally, ε is correlated to the transition dipole moment (d), which characterizes the probability amplitude of transition between initial state ψ and final state ψ'. The transition dipole moment can be defined as,

$$d = \langle \psi' | \boldsymbol{\mu} | \psi \rangle = \langle \psi' | \boldsymbol{\mu}_e + \boldsymbol{\mu}_N | \psi \rangle \qquad \text{(Eq. 1.14)}$$

where $\boldsymbol{\mu}$ is the dipole operator, which is composed of electronic dipole operator $\boldsymbol{\mu}_e$ and nuclear dipole operator $\boldsymbol{\mu}_N$. Consider the wavefunction ψ of an electron is a combination of vibrational (ψ_v), electronic (ψ_e), and spin (ψ_s) wavefunctions, it can be expressed as follows,

$$\psi = \psi_v \psi_e \psi_s \qquad \text{(Eq. 1.15)}$$

in which the electronic and vibrational wavefunctions are independent of each other under the assumption of Born–Oppenheimer approximation. The expanded expression for transition dipole moment after mathematical operations is a combination of three terms,

$$d = \langle \psi' | \boldsymbol{\mu}_e + \boldsymbol{\mu}_N | \psi \rangle = \int \psi_v'^* \psi_v dV \int \psi_e'^* \psi_e dV \int \psi_s'^* \psi_s dV \qquad \text{(Eq. 1.16)}$$

Frank-Condon factor, orbital transition integral, and spin transition integral. The latter two contributions are governed by orbital selection rules and spin selection rules, respectively.

Importantly, the Frank-Condon factor determines the strength of vibrational transition by examining the wavefunction overlapping between the ground and excited vibrational states, which often leads to the attenuation of 0-0 transition but a significant presence of 0-2 transition (Figure 1.15). It also applies when electron transition occurs from higher energy states to ground states, in another word, the fluorescence process. This is the so-called Frank-Condon principle, which is useful to explain line shapes, peak symmetries, and peak intensities shown in a typical UV-vis spectrum.

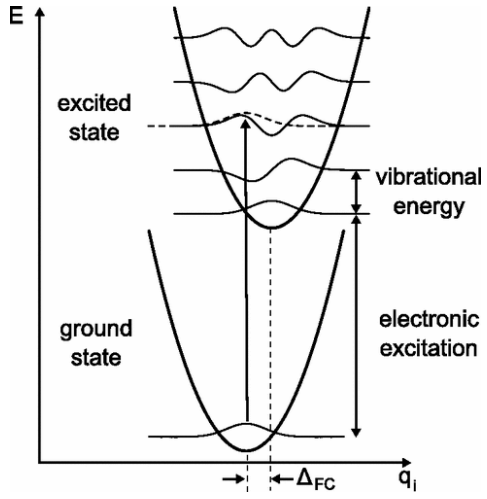

Figure 1.15 *Schematic illustration of Frank-Condon principle. Reproduced with permission from Ref.*[108] *Copyright (2013) American Physical Society.*

It is worthwhile to point out that the Frank-Condon principle cannot always provide a full explanation of the electron transition upon UV-vis excitation. The contributions from orbital and spin selection rules are often great enough to overwhelm strict compliance of the Frank-Condon principle, which challenges the interpretation of real UV-vis spectrum.

1.5.2 Fundamentals of atomic force microscope (AFM)

In 1982, Binnig and Rohrer invented the first surface probe microscope (SPM), scanning tunneling microscope (STM), which led to their awarding of the 1986 Nobel Prize

in Physics.[109-111] STM realizes the imaging of surface at an atomic level, utilizing the tunnel current to regulate the nanometer-sized gap between tip and sample. Later on, other quantities such as force, electric field, and magnetic field were used in the regulation of tip-sample gap.[112, 113] Technique based on a feedback loop regulated by atomic force on the surface was also invented by Binning and Rohrer in 1986 and they named it as "atomic force microscope" (AFM).[114] The AFM technique quickly attracted a huge amount of interest and soon became one of the most popular and successfully applied SPM techniques.[115, 116] Nowadays, it has been widely used as a robust and versatile tool in the investigation of surface properties involved in multidisciplinary topics such as surface chemistry,[117-122] polymer,[123-128] and biology.[129-134] At the same time, new AFM techniques have been developed to increase the degree of "directness of measurement",[135] which means comprehensive information of samples such as structure, dynamics, and function can be directly probed by the measurement, without excessive hypotheses and data analysis. For example, high-speed AFM can be used to study real-time dynamics of bioprocess,[136-141] single-molecule AFM is applied in probing intermolecular interactions,[142-145] while AFM-IR is capable of coupling morphological measurement with compositional measurement.[146-149] Despite the ever ongoing updates on AFM techniques, there is always some common knowledge applying. In the following sections, a short introduction to the principles of AFM imaging and general operation modes will be presented.

1.5.2.1 AFM in contact and semi-contact mode (single-pass)

An AFM includes three main parts, which are the tip, the optical (laser) system, and the piezoelectric scanner. A schematic drawing on the generic AFM set-up can be referred to in Figure 1.16. A typical AFM probe consists of a cantilever and a tip at the end of the cantilever. The other end of the cantilever is connected to a piezoelectric shaker. The tip at the end of the cantilever interacts with the sample surface during scanning. AFM tip is normally made up of abundant materials such as silicon, however, in some measurements when the conductivity of the tip needs to be assured, a noble metal such as gold and platinum or even diamond can be coated onto it. The incident laser beam is reflected by the backside of the cantilever. To enhance the laser reflectivity, the backside of the cantilever is usually coated with a reflective layer such as aluminum. The reflected laser can be recorded by a position-sensitive photodiode (PSPD). The PSPD generally is divided into four areas as shown in Figure 1.16. Before performing measurements, the PSPD is nullified. During scanning, bending or twisting motions of the cantilever due to the interaction of the tip with the sample can be sensed by the current signal change of the PSPD. Under ordinary operation modes, only normal (vertical) signal change defined as,

$$I_v = (A + C) - (B + D) \qquad \text{(Eq. 1.17)}$$

which is proportional to the bending of the cantilever. If measurements are based on lateral force, twisting of the cantilever needs to be accounted for. The twisting of the cantilever is proportional to the lateral signal changes defined as,

$$I_h = (A + B) - (C + D) \qquad \text{(Eq. 1.18)}$$

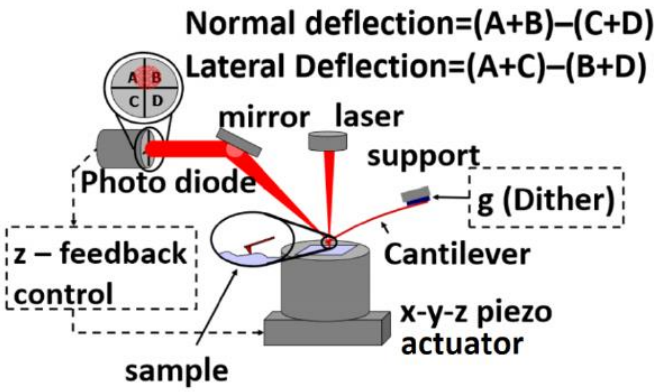

Figure 1.16 *Schematic presentation of a commercially available AFM system. Reproduced from Ref.*[150]*, with the permission from AIP publishing.*

In *contact* mode, sample surface first approach tip, which is controlled by a feedback loop on z-displacement in the piezoelectric scanner, to an arbitrary I_v level. Although I_v level can be some random values, it is important to ensure it within a suitable range, which is large enough for the tip to engage with the sample surface, but not too large so that the cantilever is over bending, breaking tip and/or sample. This tip approaching process can be denoted as tip "landing". After that, the scanner can move line-by-line along a designated x-y area while maintaining the bending of the cantilever unchanged by alternating z-displacement, which is equivalent to keeping a constant force between tip and surface. In this way, the recorded variation on the z-direction displacement of the scanner reflects the surface morphology. The automatic adjustment and recording of z-displacement during a scan is done by the feedback loop on z-displacement in a piezoelectric scanner. In addition to the piezoelectric scanner, to ensure better x-y positioning accuracy and offset thermal drifting, a separate x-y position capacitive controller is generally integrated into current commercial AFMs.

In *semi-contact* mode, the cantilever is deliberately vibrated at its intrinsic resonant frequency by a mounted piezo shaker with a suitable free vibrational amplitude. The sample then approaches the tip, but not landed on the tip. Instead, it rests below the tip with a small gap to accommodate the suitable engaging amplitude. During a *semi-contact* scan, the vibrational amplitude or frequency tends to change slightly due to the tip-sample interaction. However, the tendency of changing vibrational amplitude or frequency is again nullified by alternating z-displacement of the scanner via a feedback loop. The recorded variation on z-direction displacement of the scanner again reconstructs the surface morphology. The mode that regulates tip amplitude is named the "AM" mode while FM stands for the mode that modulates the frequency shift of the tip.

1.5.2.2 AFM in kelvin probe force microscopy mode (dual-pass)

The aforementioned *contact* and *semi-contact* mode mainly aim at obtaining morphological information on the surface. Despite the difference in imaging principles, both modes can be regarded as a single-pass mode, where the tip only scans a designated area of the surface once. To measure interfacial properties beyond morphology, sometimes a dual-pass mode is required to eliminate possible cross-talking between morphological signals and other signals. Kelvin probe force microscopy (KPFM) provides a typical dual-pass mode for the direct measurement of contact potential difference (CPD) at a nanometer scale. It was invented by Nonnenmacher et al.[151] and has been successfully applied in the characterization of organic or inorganic electronics materials.[152-157] A brief description of the imaging principles of KPFM will be shown as follows.

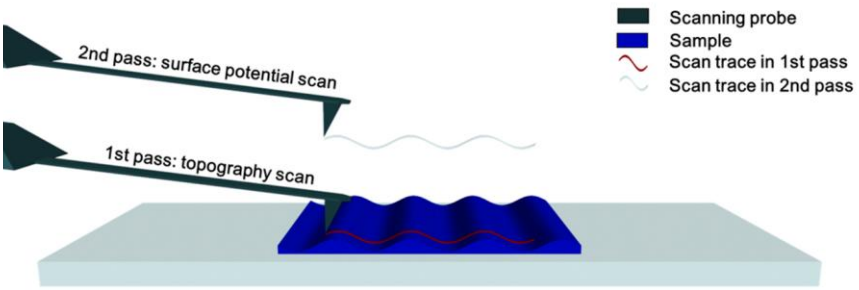

Figure 1.17 *Schematic illustration on dual-pass KPFM mode. After the first pass on topography scan, the AFM tip is lifted from the surface with a certain height and a second scan follows. Reproduced with permission from Ref.*[158] *Copyright (2016) American Physical Society.*

In dual-pass KPFM, every single line of the designated sample area will be scanned twice consecutively (Figure 1.17). The first pass is done by a typical *semi-contact* scan, acquiring morphological information of that line. Before the second pass, the AFM tip is removed from the surface by a finite distance, typically on the scale of 10 nm, to avoid any significant coupling from interactions other than electrostatic interaction such as Van der Waals attraction. This finite gap between tip and sample is maintained throughout the second pass. During the second pass, a bias with a combination of the direct and alternating components was applied to the AFM tip to probe the electrostatic interaction between tip and surface. The expression of tip voltage can be expressed as,

$$V_{tip} = V_{dc} + V_{ac}\, sin(\omega_{ac} t) \qquad \text{(Eq. 1.19)}$$

in which V_{dc} is the direct offset voltage and V_{ac} is the alternating voltage applied at a frequency of ω_{ac}. To maximize the sensitivity in this second *semi-contact* pass, ω_{ac} fulfills the resonant frequency of the tip. $\Delta\phi$ as the work function difference between tip and sample can be extracted from the nullification of electrostatic force modulated at frequency ω_{ac},

$$F_{\omega_{ac}} = (\partial C/\partial z)(V_{dc} - \Delta\phi)V_{ac}sin(\omega t) \quad \text{(Eq. 1.20)}$$

by a designated lock-in amplifier. Therefore, $\Delta\phi$ equals V_{dc}. Note that $\Delta\phi$ is more frequently referred to as contact potential difference (CPD) in KPFM literature. Theoretically, it should work out perfectly to extract absolute CPD values of samples. However, change in the work function of the tip during scanning is inevitable, and typical variations on the work function of the tip can be as large as several hundred mV, which easily distorts absolute CPD contrasts between different samples. To tackle frequently occurred tip changes, in this work the substrate was deliberately exposed by exfoliating part of the CP film so that the difference in CPD value between the CP film and substrate region can be directly interpreted as the difference in their work functions without concerning the work function variations of the tip. In summary, KPFM as a dual-pass mode provides a combination of topographical and electrical information on the sample surface, which is apparently very helpful in elucidating the structure-property correlation of CP materials or devices.

1.6 Research Scope

The research in this thesis will first focus on the chemical doping of conjugated polymers. P3HT doped by F_4TCNQ will be used as a model system for the study. To elucidate the relationship between aggregation and doping, the doping reaction upon a solution and sequential doping will be investigated by a holistic combination of different experimental techniques such as optical absorption spectroscopy, atomic force microscopy, and kelvin probe force microscopy. Hopefully, problems such as whether P3HT aggregation occurs before the charge transfer step can be resolved. Second, a higher-order

nanostructure of P3HT such as nanowires will be prepared to examine the influence of morphology and crystallinity on the chemical doping reaction of conjugated polymers. Finally, doping of conjugated polymers by ion manipulation will be involved. Given the limited access to a clean-lab facility, the original fabrication method of OECTs cannot be easily reproduced due to the extensive amount of lithography work required. Thus, novel approaches are required to prepared OECTs suitable for physiological conditions such as neutral pH and higher ionic strength.

Reference

1. Gelinck, G. H.; Huitema, H. E.; van Veenendaal, E.; Cantatore, E.; Schrijnemakers, L.; van der Putten, J. B.; Geuns, T. C.; Beenhakkers, M.; Giesbers, J. B.; Huisman, B. H.; Meijer, E. J.; Benito, E. M.; Touwslager, F. J.; Marsman, A. W.; van Rens, B. J.; de Leeuw, D. M., Flexible active-matrix displays and shift registers based on solution-processed organic transistors. *Nat. Mater.* **2004,** *3*, 106-110.
2. Lee, Y.; Zhou, H.; Lee, T.-W., One-dimensional conjugated polymer nanomaterials for flexible and stretchable electronics. *J. Mater. Chem. C* **2018,** *6* (14), 3538-3550.
3. Lussem, B.; Keum, C. M.; Kasemann, D.; Naab, B.; Bao, Z.; Leo, K., Doped Organic Transistors. *Chem. Rev.* **2016,** *116* (22), 13714-13751.
4. McQuade, D. T.; Pullen, A. E.; Swager, T. M., Conjugated polymer-based chemical sensors. *Chem. Rev.* **2000,** *100* (7), 2537-2574.
5. Sekitani, T.; Zschieschang, U.; Klauk, H.; Someya, T., Flexible organic transistors and circuits with extreme bending stability. *Nat. Mater.* **2010,** *9* (12), 1015-1022.
6. Walzer, K.; Maennig, B.; Pfeiffer, M.; Leo, K., Highly Efficient Organic Devices Based on Electrically Doped Transport Layers. *Chem. Rev.* **2007,** *107*, 1233−1271.
7. Wang, G.-J. N.; Gasperini, A.; Bao, Z., Stretchable Polymer Semiconductors for Plastic Electronics. *Adv. Electron. Mater.* **2018**, 1700429.
8. Alemu, D.; Wei, H.-Y.; Ho, K.-C.; Chu, C.-W., Highly conductive PEDOT: PSS electrode by simple film treatment with methanol for ITO-free polymer solar cells. *Energy Environ. Sci.* **2012,** *5* (11), 9662-9671.
9. Kim, Y. H.; Lee, J.; Hofmann, S.; Gather, M. C.; Müller-Meskamp, L.; Leo, K., Achieving high efficiency and improved stability in ITO-free transparent organic light-emitting diodes with conductive polymer electrodes. *Adv. Funct. Mater.* **2013,** *23* (30), 3763-3769.
10. Kim, Y. H.; Sachse, C.; Machala, M. L.; May, C.; Müller-Meskamp, L.; Leo, K., Highly conductive PEDOT: PSS electrode with optimized solvent and thermal post-treatment for ITO-free organic solar cells. *Adv. Funct. Mater.* **2011,** *21* (6), 1076-1081.
11. Dang, M. T.; Hirsch, L.; Wantz, G.; Wuest, J. D., Controlling the Morphology and Performance of Bulk Heterojunctions in Solar Cells. Lessons Learned from the Benchmark Poly(3-hexylthiophene):[6,6]-Phenyl-C61-butyric Acid Methyl Ester System. *Chem. Rev.* **2013,** *113* (5), 3734-3765.
12. Mas-Torrent, M.; Rovira, C., Role of Molecular Order and Solid-State Structure in Organic Field-Effect Transistors. *Chem. Rev.* **2011,** *111* (8), 4833-4856.
13. Sirringhaus, H., 25th Anniversary Article: Organic Field-Effect Transistors: The Path Beyond Amorphous Silicon. *Adv. Mater.* **2014,** *26* (9), 1319-1335.
14. Wang, C.; Dong, H.; Hu, W.; Liu, Y.; Zhu, D., Semiconducting π-Conjugated Systems in Field-Effect Transistors: A Material Odyssey of Organic Electronics. *Chem. Rev.* **2012,** *112* (4), 2208-2267.
15. Chiang, C. K.; Fincher Jr, C.; Park, Y. W.; Heeger, A. J.; Shirakawa, H.; Louis, E. J.; Gau, S. C.; MacDiarmid, A. G., Electrical conductivity in doped polyacetylene. *Phys. Rev. Lett.* **1977,** *39* (17), 1098.

16. Ito, T.; Shirakawa, H.; Ikeda, S., Simultaneous polymerization and formation of polyacetylene film on the surface of concentrated soluble Ziegler-type catalyst solution. *J. Polym. Sci. A Polym. Chem.* **1974,** *12* (1), 11-20.
17. Patil, A.; Heeger, A.; Wudl, F., Optical properties of conducting polymers. *Chem. Rev.* **1988,** *88* (1), 183-200.
18. Roncali, J., Conjugated poly (thiophenes): synthesis, functionalization, and applications. *Chem. Rev.* **1992,** *92* (4), 711-738.
19. Roncali, J., Synthetic principles for bandgap control in linear π-conjugated systems. *Chem. Rev.* **1997,** *97* (1), 173-206.
20. Roncali, J.; Youssoufi, H. K.; Garreau, R.; Garnier, F.; Lemaire, M., New electrogenerated conducting poly (thiophenes) containing substituted phenyl groups. *J. Chem. Soc., Chem. Commun.* **1990,** (5), 414-416.
21. Sato, M.-a.; Tanaka, S.; Kaeriyama, K., Soluble conducting polythiophenes. *J. Chem. Soc., Chem. Commun.* **1986,** (11), 873-874.
22. Yassar, A.; Roncali, J.; Garnier, F., Conductivity and conjugation length in poly (3-methylthiophene) thin films. *Macromolecules* **1989,** *22* (2), 804-809.
23. Iovu, M. C.; Sheina, E. E.; Gil, R. R.; McCullough, R. D., Experimental evidence for the quasi-"living" nature of the grignard metathesis method for the synthesis of regioregular poly (3-alkylthiophenes). *Macromolecules* **2005,** *38* (21), 8649-8656.
24. McCullogh, R. D.; Williams, S. P.; Tristam-Nagle, S.; Jayaraman, M.; Ewbank, P. C.; Miller, L., The first synthesis and new properties of regioregular, head-to-tail coupled polythiophenes. *Synth. Met.* **1995,** *69* (1-3), 279-282.
25. McCullough, R. D.; Lowe, R. D., Enhanced electrical conductivity in regioselectively synthesized poly (3-alkylthiophenes). *J. Chem. Soc., Chem. Commun.* **1992,** (1), 70-72.
26. McCullough, R. D.; Lowe, R. D.; Jayaraman, M.; Anderson, D. L., Design, synthesis, and control of conducting polymer architectures: structurally homogeneous poly (3-alkylthiophenes). *J. Org. Chem* **1993,** *58* (4), 904-912.
27. McCullough, R. D.; Tristram-Nagle, S.; Williams, S. P.; Lowe, R. D.; Jayaraman, M., Self-orienting head-to-tail poly (3-alkylthiophenes): new insights on structure-property relationships in conducting polymers. *J. Am. Chem. Soc.* **1993,** *115* (11), 4910-4911.
28. Zaumseil, J.; Sirringhaus, H., Electron and ambipolar transport in organic field-effect transistors. *Chem. Rev.* **2007,** *107* (4), 1296-1323.
29. Würthner, F.; Kaiser, T. E.; Saha-Möller, C. R., J-aggregates: from serendipitous discovery to supramolecular engineering of functional dye materials. *Angew. Chem., Int. Ed.* **2011,** *50* (15), 3376-3410.
30. Jelley, E. E., Spectral absorption and fluorescence of dyes in the molecular state. *Nature* **1936,** *138* (3502), 1009-1010.
31. Scheibe, G.; Schöntag, A.; Katheder, F., Fluoreszenz und Energiefortleitung bei reversibel polymerisierten Farbstoffen. *Naturwissenschaften* **1939,** *27* (29), 499-501.
32. Kasha, M., Energy transfer mechanisms and the molecular exciton model for molecular aggregates. *Radiat. Res.* **1963,** *20* (1), 55-70.
33. McRae, E. G.; Kasha, M., Enhancement of phosphorescence ability upon aggregation of dye molecules. *J. Chem. Phys.* **1958,** *28* (4), 721-722.

34. Spano, F. C.; Clark, J.; Silva, C.; Friend, R. H., Determining exciton coherence from the photoluminescence spectral line shape in poly (3-hexylthiophene) thin films. *J. Chem. Phys.* **2009,** *130* (7), 074904.
35. Hestand, N. J.; Spano, F. C., Expanded Theory of H-and J-Molecular Aggregates: The Effects of Vibronic Coupling and Intermolecular Charge Transfer. *Chem. Rev.* **2018**.
36. Hestand, N. J.; Spano, F. C., Molecular aggregate photophysics beyond the Kasha model: Novel design principles for organic materials. *Acc. Chem. Res.* **2017,** *50* (2), 341-350.
37. Clark, J.; Chang, J.-F.; Spano, F. C.; Friend, R. H.; Silva, C., Determining exciton bandwidth and film microstructure in polythiophene films using linear absorption spectroscopy. *Appl. Phys. Lett.* **2009,** *94* (16), 117.
38. Spano, F. C.; Silva, C., H-and J-aggregate behavior in polymeric semiconductors. *Annu. Rev. Phys. Chem.* **2014,** *65*, 477-500.
39. Spano, F. C., The spectral signatures of Frenkel polarons in H-and J-aggregates. *Acc. Chem. Res.* **2009,** *43* (3), 429-439.
40. Clark, J.; Silva, C.; Friend, R. H.; Spano, F. C., Role of intermolecular coupling in the photophysics of disordered organic semiconductors: aggregate emission in regioregular polythiophene. *Phys. Rev. Lett.* **2007,** *98* (20), 206406.
41. Spano, F. C., Modeling disorder in polymer aggregates: The optical spectroscopy of regioregular poly (3-hexylthiophene) thin films. *J. Chem. Phys.* **2005,** *122* (23), 234701.
42. Yamagata, H.; Pochas, C. M.; Spano, F. C., Designing J-and H-aggregates through wave function overlap engineering: applications to poly (3-hexylthiophene). *J. Phys. Chem. B* **2012,** *116* (49), 14494-14503.
43. Spano, F. C., The Spectral Signatures of Frenkel Polarons in H- and J-Aggregates. *Acc. Chem. Res.* **2010,** *43* (3), 429-439.
44. Kasha, M., Characterization of electronic transitions in complex molecules. *Discuss. Faraday Soc.* **1950,** *9*, 14-19.
45. Brown, P. J.; Thomas, D. S.; Köhler, A.; Wilson, J. S.; Kim, J. S.; Ramsdale, C. M.; Sirringhaus, H.; Friend, R. H., Effect of interchain interactions on the absorption and emission of poly(3-hexylthiophene). *Phys. Rev. B: Condens. Matter Mater. Phys.* **2003,** *67* (6), 1-16.
46. Brinkmann, M., Structure and morphology control in thin films of regioregular poly(3-hexylthiophene). *J. Polym. Sci., Part B: Polym. Phys.* **2011,** *49* (17), 1218-1233.
47. Niles, E. T.; Roehling, J. D.; Yamagata, H.; Wise, A. J.; Spano, F. C.; Moulé, A. J.; Grey, J. K., J-aggregate behavior in poly-3-hexylthiophene nanofibers. *J. Phys. Chem. Lett.* **2012,** *3* (2), 259-263.
48. Gryn'ova, G.; Nicolaï, A.; Prlj, A.; Ollitrault, P.; Andrienko, D.; Corminboeuf, C., Charge transport in highly ordered organic nanofibrils: lessons from modelling. *J. Mater. Chem. C* **2017,** *5* (2), 350-361.
49. Tsuzuki, S.; Honda, K.; Azumi, R., Model chemistry calculations of thiophene dimer interactions: origin of π-stacking. *J. Am. Chem. Soc.* **2002,** *124* (41), 12200-12209.
50. Ma, X.; Guo, Y.; Wang, T.; Su, Z., Scanning tunneling microscopy investigation of self-assembled poly (3-hexylthiophene) monolayer. *J. Chem. Phys.* **2013,** *139* (1), 014701.

51. Prosa, T. J.; Winokur, M. J.; Moulton, J.; Smith, P.; Heeger, A. J., X-ray Structural Studies of Poly(3-alkylthiophenes): An Example of an Inverse Comb. *Macromolecules* **1992,** *1992* (25), 4364-4372.
52. Meille, S. V.; Romita, V.; Caronna, T.; Lovinger, A. J.; Catellani, M.; Belobrzeckaja, L., Influence of Molecular Weight and Regioregularity on the Polymorphic Behavior of Poly(3-decylthiophenes). *Macromolecules* **1997,** *30*, 7898-7905.
53. Kayunkid, N.; Uttiya, S.; Brinkmann, M., Structural Model of Regioregular Poly(3-hexylthiophene) Obtained by Electron Diffraction Analysis. *Macromolecules* **2010,** *43* (11), 4961-4967.
54. Rahimi, K.; Botiz, I.; Stingelin, N.; Kayunkid, N.; Sommer, M.; Koch, F. P. V.; Nguyen, H.; Coulembier, O.; Dubois, P.; Brinkmann, M., Controllable processes for generating large single crystals of poly (3-hexylthiophene). *Angew. Chem., Int. Ed.* **2012,** *51* (44), 11131-11135.
55. Liu, J.; Sun, Y.; Gao, X.; Xing, R.; Zheng, L.; Wu, S.; Geng, Y.; Han, Y., Oriented poly(3-hexylthiophene) nanofibril with the pi-pi stacking growth direction by solvent directional evaporation. *Langmuir* **2011,** *27* (7), 4212-9.
56. Lee, Y. H.; Yang, Y. L.; Yen, W. C.; Su, W. F.; Dai, C. A., Solution self-assembly and phase transformations of form II crystals in nanoconfined poly(3-hexyl thiophene) based rod-coil block copolymers. *Nanoscale* **2014,** *6* (4), 2194-200.
57. Tsao, H. N.; Müllen, K., Improving polymer transistor performance via morphology control. *Chem. Soc. Rev.* **2010,** *39* (7), 2372-2386.
58. Kim, D. H.; Han, J. T.; Park, Y. D.; Jang, Y.; Cho, J. H.; Hwang, M.; Cho, K., Single-crystal polythiophene microwires grown by self-assembly. *Adv. Mater.* **2006,** *18* (6), 719-723.
59. Rahimi, K.; Botiz, I.; Agumba, J. O.; Motamen, S.; Stingelin, N.; Reiter, G., Light absorption of poly (3-hexylthiophene) single crystals. *RSC Adv.* **2014,** *4* (22), 11121-11123.
60. Kline, R. J.; McGehee, M. D.; Kadnikova, E. N.; Liu, J.; Frechet, J. M., Controlling the field-effect mobility of regioregular polythiophene by changing the molecular weight. *Adv. Mater.* **2003,** *15* (18), 1519-1522.
61. Kline, R. J.; McGehee, M. D.; Kadnikova, E. N.; Liu, J.; Fréchet, J. M.; Toney, M. F., Dependence of regioregular poly (3-hexylthiophene) film morphology and field-effect mobility on molecular weight. *Macromolecules* **2005,** *38* (8), 3312-3319.
62. Kline, R. J.; McGehee, M. D.; Toney, M. F., Highly oriented crystals at the buried interface in polythiophene thin-film transistors. *Nat. Mater.* **2006,** *5* (3), 222-228.
63. Yang, H.; LeFevre, S. W.; Ryu, C. Y.; Bao, Z., Solubility-driven thin film structures of regioregular poly (3-hexyl thiophene) using volatile solvents. *Appl. Phys. Lett.* **2007,** *90* (17), 172116.
64. Scavia, G.; Barba, L.; Arrighetti, G.; Milita, S.; Porzio, W., Structure and morphology optimization of poly (3-hexylthiophene) thin films onto silanized silicon oxide. *Eur. Polym. J.* **2012,** *48* (6), 1050-1061.
65. Chang, J.-F.; Sun, B.; Breiby, D. W.; Nielsen, M. M.; Sölling, T. I.; Giles, M.; McCulloch, I.; Sirringhaus, H., Enhanced mobility of poly (3-hexylthiophene) transistors by spin-coating from high-boiling-point solvents. *Chem. Mater.* **2004,** *16* (23), 4772-4776.

66. Yang, H.; Shin, T. J.; Yang, L.; Cho, K.; Ryu, C. Y.; Bao, Z., Effect of mesoscale crystalline structure on the field-effect mobility of regioregular poly (3-hexyl thiophene) in thin-film transistors. *Adv. Funct. Mater.* **2005,** *15* (4), 671-676.
67. Zen, A.; Saphiannikova, M.; Neher, D.; Grenzer, J.; Grigorian, S.; Pietsch, U.; Asawapirom, U.; Janietz, S.; Scherf, U.; Lieberwirth, I., Effect of molecular weight on the structure and crystallinity of poly (3-hexylthiophene). *Macromolecules* **2006,** *39* (6), 2162-2171.
68. Zen, A.; Pflaum, J.; Hirschmann, S.; Zhuang, W.; Jaiser, F.; Asawapirom, U.; Rabe, J. P.; Scherf, U.; Neher, D., Effect of molecular weight and annealing of poly (3-hexylthiophene) s on the performance of organic field-effect transistors. *Adv. Funct. Mater.* **2004,** *14* (8), 757-764.
69. Pingel, P.; Zen, A.; Abellón, R. D.; Grozema, F. C.; Siebbeles, L. D.; Neher, D., Temperature-resolved local and macroscopic charge carrier transport in thin P3HT layers. *Adv. Funct. Mater.* **2010,** *20* (14), 2286-2295.
70. Chen, Y.; Feng, Y.; Gao, J.; Bouvet, M., Self-assembled aggregates of amphiphilic perylene diimide–based semiconductor molecules: Effect of morphology on conductivity. *J. Colloid Interface Sci.* **2012,** *368* (1), 387-394.
71. Lüssem, B.; Keum, C.-M.; Kasemann, D.; Naab, B.; Bao, Z.; Leo, K., Doped organic transistors. *Chem. Rev.* **2016,** *116* (22), 13714-13751.
72. Reineke, S.; Lindner, F.; Schwartz, G.; Seidler, N.; Walzer, K.; Lüssem, B.; Leo, K., White organic light-emitting diodes with fluorescent tube efficiency. *Nature* **2009,** *459* (7244), 234.
73. Walzer, K.; Männig, B.; Pfeiffer, M.; Leo, K., Highly efficient organic devices based on electrically doped transport layers. *Chem. Rev.* **2007,** *107* (4), 1233-1271.
74. Hamidi-Sakr, A.; Biniek, L.; Bantignies, J. L.; Maurin, D.; Herrmann, L.; Leclerc, N.; Lévêque, P.; Vijayakumar, V.; Zimmermann, N.; Brinkmann, M., A Versatile Method to Fabricate Highly In-Plane Aligned Conducting Polymer Films with Anisotropic Charge Transport and Thermoelectric Properties: The Key Role of Alkyl Side Chain Layers on the Doping Mechanism. *Adv. Funct. Mater.* **2017,** *27* (25), 1700173.
75. Kiefer, D.; Yu, L.; Fransson, E.; Gómez, A.; Primetzhofer, D.; Amassian, A.; Campoy-Quiles, M.; Müller, C., A Solution-Doped Polymer Semiconductor: Insulator Blend for Thermoelectrics. *Adv. Sci.* **2017,** *4* (1), 1600203.
76. Lim, E.; Peterson, K. A.; Su, G. M.; Chabinyc, M. L., Thermoelectric properties of poly (3-hexylthiophene)(P3HT) doped with 2, 3, 5, 6-Tetrafluoro-7, 7, 8, 8-tetracyanoquinodimethane (F4TCNQ) by vapor-phase infiltration. *Chem. Mater.* **2018,** *30* (3), 998-1010.
77. Sun, J.; Yeh, M.-L.; Jung, B.; Zhang, B.; Feser, J.; Majumdar, A.; Katz, H., Simultaneous increase in seebeck coefficient and conductivity in a doped poly (alkylthiophene) blend with defined density of states. *Macromolecules* **2010,** *43* (6), 2897-2903.
78. Duong, D. T.; Phan, H.; Hanifi, D.; Jo, P. S.; Nguyen, T. Q.; Salleo, A., Direct observation of doping sites in temperature-controlled, p-doped p3ht thin films by conducting atomic force microscopy. *Adv. Mater.* **2014,** *26* (35), 6069-6073.

79. Gao, J.; Niles, E. T.; Grey, J. K., Aggregates promote efficient charge transfer doping of Poly(3- hexylthiophene). *J. Phys. Chem. Lett.* **2013,** *4* (17), 2953-2957.
80. Gao, J.; Roehling, J. D.; Li, Y.; Guo, H.; Moulé, A. J.; Grey, J. K., The effect of 2,3,5,6-tetrafluoro-7,7,8,8-tetracyanoquinodimethane charge transfer dopants on the conformation and aggregation of poly(3-hexylthiophene). *J. Mater. Chem. C* **2013,** *1* (36), 5638-5646.
81. Duong, D. T.; Wang, C.; Antono, E.; Toney, M. F.; Salleo, A., The chemical and structural origin of efficient p-type doping in P3HT. *Org. Electron.* **2013,** *14* (5), 1330-1336.
82. Kivala, M.; Boudon, C.; Gisselbrecht, J.-P.; Enko, B.; Seiler, P.; Müller, I. B.; Langer, N.; Jarowski, P. D.; Gescheidt, G.; Diederich, F., Organic Super-Acceptors with Efficient Intramolecular Charge-Transfer Interactions by [2+2] Cycloadditions of TCNE, TCNQ, and F4-TCNQ to Donor-Substituted Cyanoalkynes. *Chem. - Eur. J.* **2009,** *15* (16), 4111-4123.
83. Tsoi, W. C.; Spencer, S. J.; Yang, L.; Ballantyne, A. M.; Nicholson, P. G.; Turnbull, A.; Shard, A. G.; Murphy, C. E.; Bradley, D. D.; Nelson, J., Effect of crystallization on the electronic energy levels and thin film morphology of P3HT: PCBM blends. *Macromolecules* **2011,** *44* (8), 2944-2952.
84. Pingel, P.; Neher, D., Comprehensive picture of p-type doping of P3HT with the molecular acceptor F 4 TCNQ. *Phys. Rev. B* **2013,** *87* (11), 115209.
85. Aziz, E. F.; Vollmer, A.; Eisebitt, S.; Eberhardt, W.; Pingel, P.; Neher, D.; Koch, N., Localized charge transfer in a molecularly doped conducting polymer. *Adv. Mater.* **2007,** *19* (20), 3257-3260.
86. Méndez, H.; Heimel, G.; Opitz, A.; Sauer, K.; Barkowski, P.; Oehzelt, M.; Soeda, J.; Okamoto, T.; Takeya, J.; Arlin, J. B., Doping of organic semiconductors: impact of dopant strength and electronic coupling. *Angew. Chem.* **2013,** *125* (30), 7905-7909.
87. Méndez, H.; Heimel, G.; Winkler, S.; Frisch, J.; Opitz, A.; Sauer, K.; Wegner, B.; Oehzelt, M.; Röthel, C.; Duhm, S.; Többens, D.; Koch, N.; Salzmann, I., Charge-transfer crystallites as molecular electrical dopants. *Nat. Commun.* **2015,** *6*, 1-11.
88. Salzmann, I.; Heimel, G., Toward a comprehensive understanding of molecular doping organic semiconductors. *J. Electron Spectrosc. Relat. Phenom.* **2015,** *204*, 208-222.
89. Neelamraju, B.; Watts, K. E.; Pemberton, J. E.; Ratcliff, E. L., Correlation of Coexistent Charge Transfer States in F4TCNQ-Doped P3HT with Microstructure. *J. Phys. Chem. Lett.* **2018,** *9* (23), 6871-6877.
90. Bao, Q.; Liu, X.; Braun, S.; Gao, F.; Fahlman, M., Energetics at doped conjugated polymer/electrode interfaces. *Adv. Mater. Interfaces* **2015,** *2* (2), 1400403.
91. Pingel, P.; Schwarzl, R.; Neher, D., Effect of molecular p-doping on hole density and mobility in poly (3-hexylthiophene). *Appl. Phys. Lett.* **2012,** *100* (14), 87.
92. Müller, L.; Nanova, D.; Glaser, T.; Beck, S.; Pucci, A.; Kast, A. K.; Schröder, R. R.; Mankel, E.; Pingel, P.; Neher, D., Charge-transfer–solvent interaction predefines doping efficiency in p-doped P3HT films. *Chem. Mater.* **2016,** *28* (12), 4432-4439.
93. Kang, K.; Watanabe, S.; Broch, K.; Sepe, A.; Brown, A.; Nasrallah, I.; Nikolka, M.; Fei, Z.; Heeney, M.; Matsumoto, D., 2D coherent charge transport in highly ordered conducting polymers doped by solid state diffusion. *Nat. Mater.* **2016,** *15* (8), 896-902.

94. Patel, S. N.; Glaudell, A. M.; Peterson, K. A.; Thomas, E. M.; O'Hara, K. A.; Lim, E.; Chabinyc, M. L., Morphology controls the thermoelectric power factor of a doped semiconducting polymer. *Sci. Adv.* **2017,** *3* (6), e1700434.
95. Glaudell, A. M.; Cochran, J. E.; Patel, S. N.; Chabinyc, M. L., Impact of the Doping Method on Conductivity and Thermopower in Semiconducting Polythiophenes. *Adv. Energy. Mater.* **2015,** *5* (4), 1401072.
96. Hynynen, J.; Kiefer, D.; Yu, L.; Kroon, R.; Munir, R.; Amassian, A.; Kemerink, M.; Müller, C., Enhanced Electrical Conductivity of Molecularly p-Doped Poly(3-hexylthiophene) through Understanding the Correlation with Solid-State Order. *Macromolecules* **2017,** *50* (20), 8140-8148.
97. Jacobs, I. E.; Aasen, E. W.; Oliveira, J. L.; Fonseca, T. N.; Roehling, J. D.; Li, J.; Zhang, G.; Augustine, M. P.; Mascal, M.; Moulé, A. J., Comparison of solution-mixed and sequentially processed P3HT:F4TCNQ films: effect of doping-induced aggregation on film morphology. *J. Mater. Chem. C* **2016,** *4* (16), 3454-3466.
98. Scholes, D. T.; Hawks, S. A.; Yee, P. Y.; Wu, H.; Lindemuth, J. R.; Tolbert, S. H.; Schwartz, B. J., Overcoming Film Quality Issues for Conjugated Polymers Doped with F4TCNQ by Solution Sequential Processing: Hall Effect, Structural, and Optical Measurements. *J. Phys. Chem. Lett.* **2015,** *6* (23), 4786-4793.
99. Scholes, D. T.; Yee, P. Y.; Lindemuth, J. R.; Kang, H.; Onorato, J.; Ghosh, R.; Luscombe, C. K.; Spano, F. C.; Tolbert, S. H.; Schwartz, B. J., The Effects of Crystallinity on Charge Transport and the Structure of Sequentially Processed F4TCNQ-Doped Conjugated Polymer Films. *Adv. Funct. Mater.* **2017,** *27* (44), 1702654.
100. Shirakawa, H.; Louis, E. J.; MacDiarmid, A. G.; Chiang, C. K.; Heeger, A. J., Synthesis of electrically conducting organic polymers: halogen derivatives of polyacetylene,(CH) x. *J. Chem. Soc., Chem. Commun.* **1977,** (16), 578-580.
101. Rivnay, J.; Inal, S.; Salleo, A.; Owens, R. M.; Berggren, M.; Malliaras, G. G., Organic electrochemical transistors. *Nat. Rev. Mater.* **2018,** *3* (2), 17086.
102. White, H. S.; Kittlesen, G. P.; Wrighton, M. S., Chemical derivatization of an array of three gold microelectrodes with polypyrrole: fabrication of a molecule-based transistor. *J. Am. Chem. Soc.* **1984,** *106* (18), 5375-5377.
103. Rivnay, J.; Leleux, P.; Sessolo, M.; Khodagholy, D.; Hervé, T.; Fiocchi, M.; Malliaras, G. G., Organic electrochemical transistors with maximum transconductance at zero gate bias. *Adv. Mater.* **2013,** *25* (48), 7010-7014.
104. Berggren, M.; Richter-Dahlfors, A., Organic bioelectronics. *Adv. Mater.* **2007,** *19* (20), 3201-3213.
105. Khodagholy, D.; Rivnay, J.; Sessolo, M.; Gurfinkel, M.; Leleux, P.; Jimison, L. H.; Stavrinidou, E.; Herve, T.; Sanaur, S.; Owens, R. M., High transconductance organic electrochemical transistors. *Nat. Commun.* **2013,** *4*, 2133.
106. Owens, R. M.; Malliaras, G. G., Organic electronics at the interface with biology. *MRS bulletin* **2010,** *35* (6), 449-456.
107. Bernards, D. A.; Malliaras, G. G., Steady-state and transient behavior of organic electrochemical transistors. *Adv. Funct. Mater.* **2007,** *17* (17), 3538-3544.

108. Pittner, S.; Lehmann, D.; Zahn, D. R.; Wagner, V., Charge transport analysis of poly (3-hexylthiophene) by electroreflectance spectroscopy. *Phys. Rev. B* **2013,** *87* (11), 115211.
109. Binnig, G.; Rohrer, H.; Gerber, C.; Weibel, E., 7× 7 reconstruction on Si (111) resolved in real space. *Phys. Rev. Lett.* **1983,** *50* (2), 120.
110. Binnig, G.; Rohrer, H.; Gerber, C.; Weibel, E., Surface studies by scanning tunneling microscopy. *Phys. Rev. Lett.* **1982,** *49* (1), 57.
111. Binnig, G.; Rohrer, H., Scanning tunneling microscopy—from birth to adolescence. *Rev. Mod. Phys.* **1987,** *59* (3), 615.
112. Martin, Y.; Wickramasinghe, H. K., Magnetic imaging by ‘‘force microscopy’’with 1000 Å resolution. *Appl. Phys. Lett.* **1987,** *50* (20), 1455-1457.
113. Rugar, D.; Mamin, H.; Guethner, P.; Lambert, S.; Stern, J.; McFadyen, I.; Yogi, T., Magnetic force microscopy: General principles and application to longitudinal recording media. *J. Appl. Phys.* **1990,** *68* (3), 1169-1183.
114. Binnig, G.; Quate, C. F.; Gerber, C., Atomic force microscope. *Phys. Rev. Lett.* **1986,** *56* (9), 930.
115. Giessibl, F. J., Advances in atomic force microscopy. *Rev. Mod. Phys.* **2003,** *75* (3), 949.
116. Garcıa, R.; Perez, R., Dynamic atomic force microscopy methods. *Surf. Sci. Rep.* **2002,** *47* (6-8), 197-301.
117. Butt, H.-J.; Cappella, B.; Kappl, M., Force measurements with the atomic force microscope: Technique, interpretation and applications. *Surf. Sci. Rep.* **2005,** *59* (1-6), 1-152.
118. Butt, H.-J., Measuring electrostatic, van der Waals, and hydration forces in electrolyte solutions with an atomic force microscope. *Biophys. J.* **1991,** *60* (6), 1438-1444.
119. Boland, T.; Ratner, B., Direct measurement of hydrogen bonding in DNA nucleotide bases by atomic force microscopy. *Proc. Natl. Acad. Sci. U.S.A.* **1995,** *92* (12), 5297-5301.
120. Ducker, W. A.; Senden, T. J.; Pashley, R. M., Direct measurement of colloidal forces using an atomic force microscope. *Nature* **1991,** *353* (6341), 239.
121. Frisbie, C. D.; Rozsnyai, L. F.; Noy, A.; Wrighton, M. S.; Lieber, C. M., Functional group imaging by chemical force microscopy. *Science* **1994,** *265* (5181), 2071-2074.
122. Sugimoto, Y.; Pou, P.; Abe, M.; Jelinek, P.; Pérez, R.; Morita, S.; Custance, O., Chemical identification of individual surface atoms by atomic force microscopy. *Nature* **2007,** *446* (7131), 64.
123. Yamamoto, S.; Ejaz, M.; Tsujii, Y.; Fukuda, T., Surface interaction forces of well-defined, high-density polymer brushes studied by atomic force microscopy. 2. Effect of graft density. *Macromolecules* **2000,** *33* (15), 5608-5612.
124. Yamamoto, S.; Ejaz, M.; Tsujii, Y.; Matsumoto, M.; Fukuda, T., Surface interaction forces of well-defined, high-density polymer brushes studied by atomic force microscopy. 1. Effect of chain length. *Macromolecules* **2000,** *33* (15), 5602-5607.
125. Yoon, J. A.; Kamada, J.; Koynov, K.; Mohin, J.; Nicolaÿ, R.; Zhang, Y.; Balazs, A. C.; Kowalewski, T.; Matyjaszewski, K., Self-healing polymer films based on thiol–

disulfide exchange reactions and self-healing kinetics measured using atomic force microscopy. *Macromolecules* **2011,** *45* (1), 142-149.
126. Ortiz, C.; Hadziioannou, G., Entropic elasticity of single polymer chains of poly (methacrylic acid) measured by atomic force microscopy. *Macromolecules* **1999,** *32* (3), 780-787.
127. Lavalle, P.; Gergely, C.; Cuisinier, F.; Decher, G.; Schaaf, P.; Voegel, J.; Picart, C., Comparison of the structure of polyelectrolyte multilayer films exhibiting a linear and an exponential growth regime: An in situ atomic force microscopy study. *Macromolecules* **2002,** *35* (11), 4458-4465.
128. Bar, G.; Thomann, Y.; Brandsch, R.; Cantow, H.-J.; Whangbo, M.-H., Factors affecting the height and phase images in tapping mode atomic force microscopy. Study of phase-separated polymer blends of poly (ethene-co-styrene) and poly (2, 6-dimethyl-1, 4-phenylene oxide). *Langmuir* **1997,** *13* (14), 3807-3812.
129. Kasas, S.; Thomson, N. H.; Smith, B. L.; Hansma, H. G.; Zhu, X.; Guthold, M.; Bustamante, C.; Kool, E. T.; Kashlev, M.; Hansma, P. K., Escherichia coli RNA polymerase activity observed using atomic force microscopy. *Biochemistry* **1997,** *36* (3), 461-468.
130. Haase, K.; Pelling, A. E., Investigating cell mechanics with atomic force microscopy. *J. R. Soc. Interface* **2015,** *12* (104), 20140970.
131. Hoh, J. H.; Hansma, P. K., Atomic force microscopy for high-resolution imaging in cell biology. *Trends Cell Biol.* **1992,** *2* (7), 208-213.
132. Hansma, H. G., Surface biology of DNA by atomic force microscopy. *Annu. Rev. Phys. Chem.* **2001,** *52* (1), 71-92.
133. Hansma, P.; Elings, V.; Marti, O.; Bracker, C., Scanning tunneling microscopy and atomic force microscopy: application to biology and technology. *Science* **1988,** *242* (4876), 209-216.
134. Touhami, A.; Nysten, B.; Dufrêne, Y. F., Nanoscale mapping of the elasticity of microbial cells by atomic force microscopy. *Langmuir* **2003,** *19* (11), 4539-4543.
135. Ando, T.; Uchihashi, T.; Scheuring, S., Filming biomolecular processes by high-speed atomic force microscopy. *Chem. Rev.* **2014,** *114* (6), 3120-3188.
136. Minne, S.; Yaralioglu, G.; Manalis, S.; Adams, J.; Zesch, J.; Atalar, A.; Quate, C., Automated parallel high-speed atomic force microscopy. *Appl. Phys. Lett.* **1998,** *72* (18), 2340-2342.
137. Humphris, A.; Miles, M.; Hobbs, J., A mechanical microscope: High-speed atomic force microscopy. *Appl. Phys. Lett.* **2005,** *86* (3), 034106.
138. Fantner, G. E.; Barbero, R. J.; Gray, D. S.; Belcher, A. M., Kinetics of antimicrobial peptide activity measured on individual bacterial cells using high-speed atomic force microscopy. *Nat. Nanotechnol.* **2010,** *5* (4), 280.
139. Rajendran, A.; Endo, M.; Sugiyama, H., State-of-the-art high-speed atomic force microscopy for investigation of single-molecular dynamics of proteins. *Chem. Rev.* **2013,** *114* (2), 1493-1520.
140. Uchihashi, T.; Iino, R.; Ando, T.; Noji, H., High-speed atomic force microscopy reveals rotary catalysis of rotorless F1-ATPase. *Science* **2011,** *333* (6043), 755-758.

141. Kodera, N.; Yamamoto, D.; Ishikawa, R.; Ando, T., Video imaging of walking myosin V by high-speed atomic force microscopy. *Nature* **2010,** *468* (7320), 72.
142. Rief, M.; Oesterhelt, F.; Heymann, B.; Gaub, H. E., Single molecule force spectroscopy on polysaccharides by atomic force microscopy. *Science* **1997,** *275* (5304), 1295-1297.
143. Gross, L.; Mohn, F.; Moll, N.; Liljeroth, P.; Meyer, G., The chemical structure of a molecule resolved by atomic force microscopy. *Science* **2009,** *325* (5944), 1110-1114.
144. Hugel, T.; Holland, N. B.; Cattani, A.; Moroder, L.; Seitz, M.; Gaub, H. E., Single-molecule optomechanical cycle. *Science* **2002,** *296* (5570), 1103-1106.
145. Li, H.; Rief, M.; Oesterhelt, F.; Gaub, H. E., Single-molecule force spectroscopy on xanthan by AFM. *Adv. Mater.* **1998,** *10* (4), 316-319.
146. Dazzi, A.; Prater, C. B., AFM-IR: technology and applications in nanoscale infrared spectroscopy and chemical imaging. *Chem. Rev.* **2016,** *117* (7), 5146-5173.
147. Morsch, S.; Liu, Y.; Lyon, S. B.; Gibbon, S. R., Insights into epoxy network nanostructural heterogeneity using AFM-IR. *ACS Appl. Mater. Interfaces* **2015,** *8* (1), 959-966.
148. Barlow, D. E.; Biffinger, J. C.; Cockrell-Zugell, A. L.; Lo, M.; Kjoller, K.; Cook, D.; Lee, W. K.; Pehrsson, P. E.; Crookes-Goodson, W. J.; Hung, C.-S., The importance of correcting for variable probe–sample interactions in AFM-IR spectroscopy: AFM-IR of dried bacteria on a polyurethane film. *Analyst* **2016,** *141* (16), 4848-4854.
149. Mayet, C.; Dazzi, A.; Prazeres, R.; Ortega, J.-M.; Jaillard, D., In situ identification and imaging of bacterial polymer nanogranules by infrared nanospectroscopy. *Analyst* **2010,** *135* (10), 2540-2545.
150. Baranwal, M.; Gorugantu, R. S.; Salapaka, S. M., Robust atomic force microscopy using multiple sensors. *Rev. Sci. Instrum.* **2016,** *87* (8), 083704.
151. Nonnenmacher, M.; o'Boyle, M.; Wickramasinghe, H. K., Kelvin probe force microscopy. *Appl. Phys. Lett.* **1991,** *58* (25), 2921-2923.
152. Xie, H.; Zhang, H.; Hussain, D.; Meng, X.; Song, J.; Sun, L., Multiparametric Kelvin Probe Force Microscopy for the Simultaneous Mapping of Surface Potential and Nanomechanical Properties. *Langmuir* **2017,** *33* (11), 2725-2733.
153. Palermo, V.; Ridolfi, G.; Talarico, A. M.; Favaretto, L.; Barbarella, G.; Camaioni, N.; Samori, P., A Kelvin probe force microscopy study of the photogeneration of surface charges in all-thiophene photovoltaic blends. *Adv. Funct. Mater.* **2007,** *17* (3), 472-478.
154. Panchal, V.; Pearce, R.; Yakimova, R.; Tzalenchuk, A.; Kazakova, O., Standardization of surface potential measurements of graphene domains. *Sci. Rep.* **2013,** *3*, 2597.
155. Liscio, A.; Veronese, G. P.; Treossi, E.; Suriano, F.; Rossella, F.; Bellani, V.; Rizzoli, R.; Samorì, P.; Palermo, V., Charge transport in graphene–polythiophene blends as studied by Kelvin Probe Force Microscopy and transistor characterization. *J. Mater. Chem.* **2011,** *21* (9), 2924-2931.
156. Hu, Y.; Pecunia, V.; Jiang, L.; Di, C. A.; Gao, X.; Sirringhaus, H., Scanning Kelvin probe microscopy investigation of the role of minority carriers on the switching characteristics of organic field-effect transistors. *Adv. Mater.* **2016,** *28* (23), 4713-4719.

157. Fuchs, F.; Caffy, F.; Demadrille, R.; Mélin, T.; Grévin, B., High-Resolution Kelvin Probe Force Microscopy Imaging of Interface Dipoles and Photogenerated Charges in Organic Donor–Acceptor Photovoltaic Blends. *ACS Nano* **2016,** *10* (1), 739-746.
158. Li, S.; Zhou, Y.; Zi, Y.; Zhang, G.; Wang, Z. L., Excluding contact electrification in surface potential measurement using kelvin probe force microscopy. *ACS Nano* **2016,** *10* (2), 2528-2535.

CHAPTER II - Aggregation of P3HT as a Preferred Pathway for its Chemical Doping by F_4-TCNQ

(This chapter is adapted with permission from *Chem. Comm*, 2018, 54, 11925–11928).

In Chapter II, the chemical doping reaction of P3HT by F4-TCNQ is studied by optical absorption spectroscopy, atomic force microscopy, and kelvin probe force microscopy. We demonstrate that the P3HT aggregation step is highly preferred before the actual charge transfer step takes place, emphasizing the impacts of morphology on chemical doping reaction of conjugated polymers at molecular level.

2.1 Introduction

Recent years have witnessed an ascending research attention on organic electronics based on conjugated polymers due to its potential advantages in flexibility, cost and processing convenience compared to traditional inorganic materials.[1-4] Despite the ongoing development of organic electronic materials, their electrical properties such as charge mobilities still lag behind inorganic materials such as crystalline silicon. Thus, chemical doping is brought into practice to improve the electronic performance of conjugated polymers. For example, the electrical conductivity of poly(3-hexylthiophene) (P3HT) is several orders of magnitude higher after being p-doped with 7,7,8,8-tetracyano-2,3,5,6-tetrafluoroquinodimethane (F_4-TCNQ).[5, 6] Among all the chemical doing methods, solution doping is widely applied for conjugated polymer due to its compatibility for various large-scale printing and spraying techniques. [7-11]

In general, P3HT adopts two basic morphological forms in solution, solubilized form (s-P3HT) and aggregated nanowhisker form (nw-P3HT) that can adopt H-type or J-type aggregation form based on sample preparation conditions.[12, 13] The aggregation process in solution, or the conversion of s-P3HT to nw-P3HT, is typically solubility-driven. Our previous study revealed a clear dependence of P3HT/F_4-TCNQ p-doping reaction kinetics on the morphological forms of P3HT.[14] The doping reaction rate constant of nw-P3HT is about 1000 times larger than that of s-P3HT likely due to promoted initial charge transfer and/or the quick charge delocalization immediately following the charge transfer step. One question remains to be addressed for this doping reaction is that there are two possible mechanisms for the p-doping reaction of s-P3HT by F_4-TCNQ that could lead to same final doping products of $P3HT^+$ and F_4-$TCNQ^-$, as shown in Figure 2.1. In Mechanism I, fully solubilized s-P3HT undergoes an initial charge transfer (C.T.) with F_4-TCNQ, then the bound ion pair is separated in the charge separation step. In this mechanism, either step can be the rate determining step (R.D.S.). In Mechanism II, the s-P3HT will first aggregate into nw-P3HT, which will then react with F_4-TCNQ. In Mechanism II the first aggregation step will likely be the R.D.S. because our previous studies have demonstrated the quick reaction kinetics between nw-P3HT and F_4-TCNQ within a time of scale of several minutes.[14]

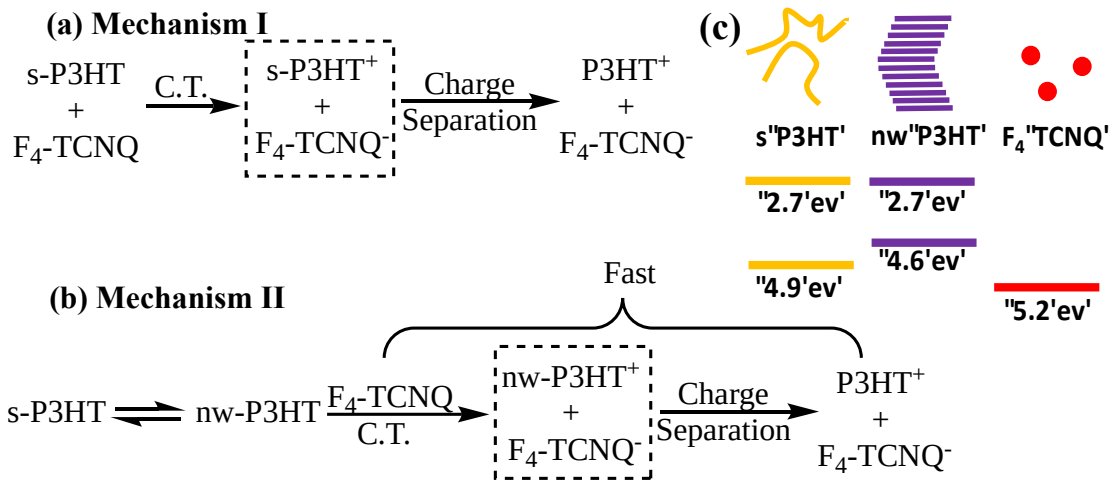

Figure 2.1 *Possible doping pathways and energetics of donor and acceptor. Dotted boxes indicate the intermediate states in doping reactions before charge separation.*

Note: (a-b) Possible reaction pathways for p-doping reaction of s-P3HT by F_4-TCNQ. (c) HOMO and LUMO levels of the s-P3HT, nw-P3HT, and F_4-TCNQ, values are adopted from references.[15, 16]

For the P3HT used in our previous studies (Mn = 70.5 kDa), elevated temperature such as 90^{o}C is required to fully dissolve a moderate concentration (> 0.1 mg/mL) of it in a marginal solvent such as toluene. After cooled down to room temperature, fully solubilized s-P3HT chains would start aggregating into nw-P3HT through π–π stacking between polythiophene segments. This aging process results in the coexistence of s-P3HT and nw-P3HT in P3HT solution at room temperature. However, we have shown that the doping reaction by F_4-TCNQ would simultaneously induce the formation of P3HT aggregates in toluene,[17] which means the final doping product $P3HT^+$ would almost always adopt the aggregated form. Therefore, it would be difficult to distinguish the two mechanisms listed in Figure 2.1 unless the formation of nw-P3HT can be excluded with the addition of F_4-TCNQ.

2.2 Materials and Methods

2.2.1 Materials

Regioregular (rr) low molecular weight (LMW) P3HT (Mw=31.3 kDa, Mn=15.6kDa, H-T regioregularity = 93.6 %) was purchased from Ossila. Dopant F_4-TCNQ (>98%) was purchased from TCI America. The indium tin oxide (ITO) glass substrate was purchased from Colorado Concept Coating, LLC, USA and the glass slide was purchased from Fisher Scientific. The organic solvents in reagent grade were used as received.

2.2.2 UV-vis Sample Preparation.

A 1 mg/mL LMW P3HT in toluene solution was prepared by heating it at 90 °C until a transparent orange solution is formed. This stock solution was stable at room temperature over weeks. A 225 μg/mL F_4-TCNQ in toluene solution was also prepared. The P3HT solutions for UV-vis/UV-vis-NIR measurements were diluted from the stock solution by additions of appropriate amount of toluene, decane and dopant solution and transferred into air-sealed custom-made 2 mm cuvettes for UV-Vis and UV-Vis-NIR measurements. Decane fractions were in volume percentages. Doping ratio was calculated as (mass of F_4-TCNQ / mass of P3HT) x 100wt%. All preparations and handling of solution samples were carried out in a N_2 filled glovebox.

2.2.3 Film Sample Preparation

ITO substrate was cleaned by ultrasonication for 15 mins in a mixture of 1:1:1 acetone/chlorobenzene/toluene solution. After sonication, it was blown dry under compressed ultrahigh-purity (>99.99%) N_2 flow.

For AFM measurements, LMW-P3HT was deposited by spin-coating 5 μL of 1 mg/mL LMW-P3HT stock solution on a 10x10 mm ITO substrate at 2000 rpm for 120s. The doped sample was obtained by dipping the as-deposited substrate in acetonitrile for 60 s and subsequently immersing the substrate into 225 μg/mL F_4-TCNQ in acetonitrile for 60 s. The undoped film sample was also dipped into acetonitrile solvent for 120 s as a control to eliminate the solvent effect. The partially dedoped sample was prepared by dipping the as-deposited substrate into 225 μg/mL F_4-TCNQ in acetonitrile for 60 s and subsequently rinsing in acetonitrile for 60 s. The prepared sample substrates were blown dry by N_2 flow.

For film UV-Vis study, ultrathin P3HT film was also prepare on thin glass slide following the procedure of P3HT film on ITO mentioned above. The preparation of undoped, doped and partially dedoped samples on glass slides also followed the same procedure. The prepared glass slides were blown dry by N_2 flow.

2.2.4 Characterizations

UV-vis spectroscopy was performed on a Cary 60 UV−vis spectrometer. AFM and Kelvin Probe Force Microscopy (KPFM) measurements were carried out on a NTEGRA Prima AFM from NT-MDT. Topography measurements were taken under semi-contact mode using microfabricated Pt-coated silicon tips (μMasch NSC18-Pt) with a typical resonant frequency of 75 kHz and a spring force constant of 1.2−5.5 N/m. To partially expose the ITO substrate as an internal reference, same AFM tips were employed in lithography mode to impact the surface. KPFM images were recorded in two-pass mode using Pt-coated tips. The first pass of KPFM was performed in tapping mode, recording

the topography. A second pass with a lift height of 10 nm followed the obtained topography. A bias was applied to the AFM tip during the second pass, V_{tip} = Vdc + V_{ac} sin(ω_{ac}t), where Vdc is the dc offset voltage and V_{ac} is the ac voltage applied at frequency of ω_{ac}. Typically ω_{ac} is selected at the tip resonant frequency in the second pass to maximize the sensitivity. A lock-in amplifier is used to extract the electrostatic force modulated at frequency ω_{ac}, $F\omega_{ac} = (\partial C/\partial z)(Vdc - \Delta\phi)Vac \sin(\omega t)$, where $\Delta\phi$ is the contact potential difference (CPD), or namely the work function difference between tip and sample due to the equilibrium of Fermi levels. Fωac is nullified when the feedback controller sets $V_{dc} = \Delta\phi$, which equals local CPD. Since in this work, ITO substrate was deliberately exposed, the difference in CPD value between film and ITO region can be directly interpreted as the difference in their work functions without concerning the work function variations of Pt-Coated silicon tip.

2.2.5 Device Fabrication and Charge Transport Measurements

Quartz substrates were cleaned using detergent in deionized water, acetone, then isopropyl alcohol for 15 min sequentially under sonication and dried in an oven. Gold electrodes (40 nm) were thermally evaporated at 1×10^{-7} torr using a shadow mask on top of the quartz. The defined channel was 30 μm long and 1 mm wide. 40 μL of 1 mg mL^{-1} P3HT stock solution in toluene was spin-coated at 2000 rpm for 120 s to give a ~2.5 nm thick film, proving the formation of an ultrathin film. Doped samples were made by applying a 225 μg mL^{-1} F4-TCNQ solution in acetonitrile on the P3HT-coated substrate for 60 s. After this time, the substrate was spun at 1500 rpm for 30 s, resulting in a ~3.5 nm thick film. Devices were tested on a Signatone 1160 series probe station inside a

nitrogen glovebox. Data was collected by a Keithley 4200 semiconductor characterization system.

2.3 Results and Discussion

2.3.1 Doping in solution: aggregation induced doping

To properly elucidate the mechanism of P3HT p-doped by F_4-TCNQ, herein a low molecular weight (LMW) P3HT (Mw=31.3 kDa) is used. This LMW-P3HT has better solubility in toluene, so within a reasonable concentration range (0.03 – 1 mg/mL), its toluene solution is free of nw-P3HT components (or at least below the detecting limit of optical absorption spectroscopy). In order to induce the aggregation of LMW-P3HT, a poor solvent, such as decane, needs to be added. This anti-solvent addition method is one of the most common crystallization techniques for the formation of conjugated polymer nanostructures in solution.[18-24] By controlling the exact morphological form of P3HT in solution, we will elucidate the reaction pathway for s-P3HT p-doped with F_4-TCNQ. In addition, the aggregation of LMW-P3HT can also occur during the drying process on a substrate. Atomic force microscopy (AFM) and kelvin probe force microscopy (KPFM) are used to characterize the LMW-P3HT film before and after doping by F_4-TCNQ to provide a microscopic understanding on the morphology-electronic property relationship of P3HT film.

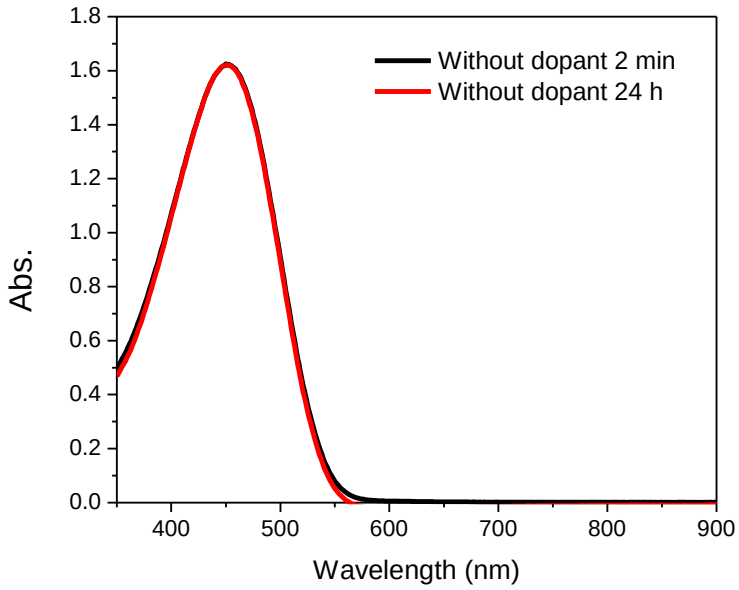

Figure 2.2 *UV-Vis spectra of 167 μg/mL LMW-P3HT in toluene.*

Note: single absorbance peaks at 450nm attributed to the π–π* transition peak of s-P3HT in solution are observed both in freshly made and aged samples, indicating LMW-P3HT in toluene remains in solubilized state without any aggregation.

The UV-vis spectra of a LMW-P3HT in toluene (167 μg/mL) is shown in Figure 2.2. There is only one major absorption peak at 450 nm, which is the π–π* transition peak of s-P3HT in solution.[25-27] After aging of 24 h the polymer remains exclusively in s-P3HT state. Upon the addition of F_4-TCNQ dopant and sequent 24 h aging, no emergence of characteristic absorbance peaks attributed to either P3HT aggregates (565 nm and 615 nm) or doping products (768 nm and 850 nm) could be observed, shown as the red spectra in Figure 2.3(a). This result shows that s-P3HT will not undergo noticeable integer charge transfer (ICT) reaction with F_4-TCNQ when remaining in s-P3HT state, which means the Mechanism I proposed in Figure 2.1 that fully solubilized P3HT undergoes doping is likely invalid. When 45% decane was added into the freshly prepared LMW-P3HT toluene solution, absorbance peaks centered at 615nm and 565nm formed immediately (shown as

the blue spectra in Figure 2.3(a)), which are attributed to 0−0 and 0−1 vibronic transitions of π−π stacked P3HT aggregates.[25-27] Interestingly, when 45% decane was added into the freshly prepared LMW-P3HT toluene solution with F_4-TCNQ (similar to the no-doping reaction sample shown as the red spectra in Figure 2.3(a)), there are immediate emergence of aggregation peaks (565 nm and 615 nm) and absorbance bands centered at 768 nm and 850 nm that can be assigned to the doping products of P3HT polaron / bipolaron and F_4-TCNQ anion, as shown by the green spectra in Figure 2.3(a). This result indicates that once the P3HT form aggregates, the resulting nw-P3HT will undergo a quick ICT with F_4-TCNQ to generate the doping products, consistent with the Mechanism II. Furthermore, compared with toluene (ε = 2.38), decane (ε = 2.00) is even less non-polar, so this observed anti-solvent induced doping phenomenon probably does not have a charge-transfer step as its R.D.S., which is inconsistent with Mechanism I.

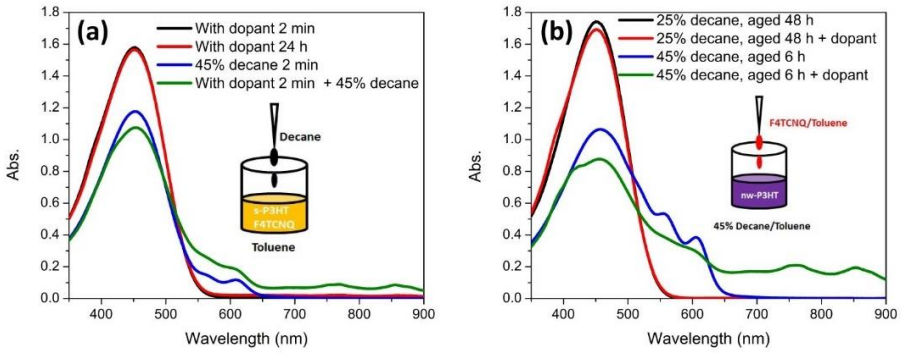

Figure 2.3 *UV-vis spectra of LMW-P3HT solutions (167 μg/mL). 3.7 wt% F_4-TCNQ is added in all doping scenario.*

Note: (a) Black and red solid lines are for LMW-P3HT in toluene after adding F_4-TCNQ for 2 min and 24 h, respectively. Blue and green solid lines are for LMW-P3HT in toluene with and without F_4-TCNQ after adding 45% decane for 2 min, respectively. (b) Black solid line is for LMW-P3HT in a binary solvent (25% decane in toluene) after aging for 48 h. The UV-vis spectra of the same solution immediately after adding F_4-TCNQ dopant is shown as the red solid line. Blue solid line is LMW-P3HT in a 45% decane in toluene after aging for 6 h. Green solid line is the spectra of the same aged sample immediately after adding F_4-TCNQ dopant. Inset: Schematic drawings on the scenarios in which doping occur are presented.

To further consolidate the priority of aggregation on this doping reaction, pre-aggregated P3HT in a 45% decane in toluene was also investigated (Figure 2.3(b)). After aging for 6h without dopant in 45% decane, significant amount of aggregation had been developed in LMW P3HT solution, indicating that 45% decane in toluene could be regarded as a rather poor binary solvent for LMW P3HT. Upon the addition of F_4-TCNQ, doping products immediately formed, indicated by the formation of 768 nm and 850 nm peaks in the adsorption band. On the contrast, there was absence of aggregation formation for the LMW P3HT in 25% decane case even after 48h of aging. In turn, there was no immediate proceeding of ICT doping reactions when F_4-TCNQ is added because no P3HT aggregates were presented in solution.

In summary, this observation confirmed that aggregation of P3HT is a prerequisite of doping by F_4-TCNQ, which is consistent with Mechanism II. This means that for the reaction pathway in Mechanism I, either the initial C.T. step or the following charge separation step has a large activation barrier that prevents the reaction from taking place. After converting s-P3HT to nw-P3HT, either the redox potential of P3HT is lower to provide more overall driving force or the charge injection/charge delocalization can be promoted because the nw-P3HT has more efficient charge transport characteristics.[16, 28-31] Both factors could potentially lower the activation energy of the reaction. So, in the case of pre-aggregated nw-P3HT, its charge transfer reaction with F_4-TCNQ can proceed readily.

Despite the confirmation on the priority of aggregation, it would still be worthwhile to elucidate the effect of aging on the doping products because aging is an important

measure to manipulate the electronic properties of processed conjugated polymeric materials. Therefore, aging scenarios on doped LMW P3HT in 45% decane in toluene was also investigated with both the dopant and anti-solvent added before any aging or doping starts. In Figure 2.4, even when there was no dopant presented, absorbance peaks at 615nm and 565nm emerged shortly after the addition of P3HT into binary solvent mixture. The absorbance intensities of these aggregation vibronic peaks increased by at least three folds after 6h, indicating a further development of P3HT aggregates. When dopant F_4-TCNQ is added to the P3HT in 45% decane before the aging process starts, doping reaction immediately occurred because the P3HT molecules readily aggregate into nw-P3HT form. Interestingly, the absorbance bands of doping products centred at 768 and 850 nm remained unchanged after 2 minutes of doping reaction, indicating the fast kinetics of doping reaction on aggregated P3HT in poor solvent. In another word, doping reaction can be mostly finished within 2 minutes. The intensities of absorbance peaks (565 nm and 615 nm) of P3HT aggregates after 2 minutes of doping were much larger than those in the undoped case after 2 minutes of aging, suggesting a faster initial aggregation rate, which is consistent with our previous report of doping-induced aggregation of P3HT.[13, 17, 28, 32] After 6 h of aging, the aggregation absorption intensities are comparable for both cases of with or without the F_4-TCNQ dopant. The slower increase of P3HT aggregates absorption bands after the initial 2 min could be partially due to the conversion of some P3HT aggregates into doping products and the precipitation of P3HT doping products.[5, 33, 34]

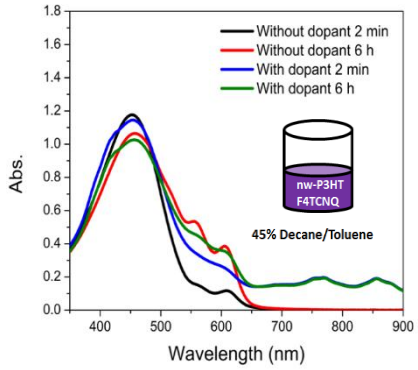

Figure 2.4 *Evolution of UV-Vis spectra of 167 μg/mL LMW P3HT in binary solvent (45% decane in toluene).*

Note: Both scenario with (blue and olive lines) and without (black and red lines) addition of 3.7wt% F_4-TCNQ dopant are shown. Inset: Schematic drawing on the scenario in which doping occur is presented.

Aging scenarios on doped LMW P3HT in 25% and 30% decane in toluene were also examined (Figure 2.5). Both anti-solvent induced and doping induced aggregation in those cases are much less prominent and slower (~hours) than it in the 45% decane case.

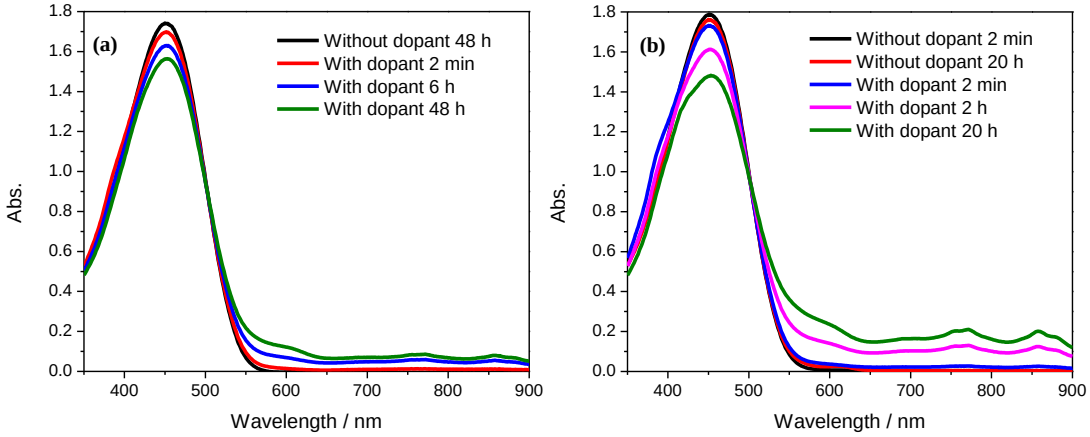

Figure 2.5 *Evolution of UV-Vis spectra of 167 μg/mL LMW P3HT in binary solvents.*

Note: 25% decane in toluene (a) and 30% decane in toluene (b) before and after addition of 3.7 wt% F_4-TCNQ dopant. After the addition of dopant, the absorbance bands centered at 768 and 850 nm emerged gradually, which corresponded to the doping products of P3HT polaron/bipolaron and F_4-TCNQ anion. The doping reaction proceeds faster in 30% decane in toluene than in 25% decane in toluene.

Therefore, a new strategy can be developed to control doping rate or morphology of conjugated polymer by fine-tuning of solvent quality and aging.

2.3.2 Doping on a solid surface: a KPFM and conductivity measurement combined study

Doping in a solid film by sequential deposition of dopant has attracted ascending research because it provides a promising way of fabricating OSC devices with controlled morphology. In this technique, a suitable orthogonal solvent such as acetonitrile is used so that it only dissolves the dopant but not the host polymer. Film made from this "orthogonal doping" technique shows superior charge transport performance with higher in-plane conductivity due to well-connected crystalline host polymer domains.[35] Despite some pioneering study on the conductivity of doped P3HT film,[5, 6, 15, 36] there is still lack of a microscopic understanding on the work function (W) change of conjugated polymer films after "orthogonal doping" by F_4-TCNQ.

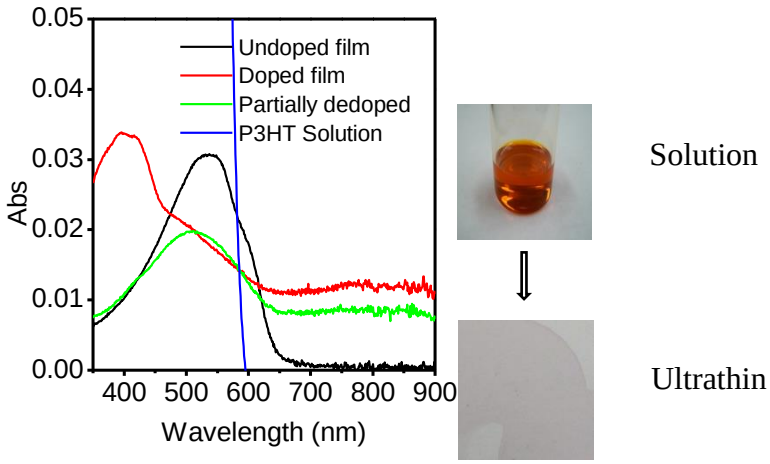

Figure 2.6 *UV-Vis spectra of 1mg/mL LMW P3HT in toluene stock solution, ultrathin film prepared from spin-coating of the stock solution.*

Note: the doped ultrathin film and the partially dedoped ultrathin film. No observable absorbance peaks at 615 nm and 565 nm associated with the vibronic 0−0 and 0−1 vibronic transitions can be observed, indicating 1 mg/mL P3HT toluene solution is free from forming π−π stacking aggregates. Peak at 450 nm of s-P3HT in solution is not shown here because its intensity is out of range of the instrument. The purple P3HT film prepared from drop-casting of the stock solution shows characteristic absorbance of P3HT aggregates at 565nm and 615nm. After "orthogonal doping" by F_4-TCNQ solution, absorption bands of doping product emerge along with a drastic decrease of the vibronic 0−0 and 0−1 peaks. This indicates the transition of undoped aggregates into doped polarons.

Pristine LMW P3HT film is prepared by spin-coating 10 μL of 1 mg/mL P3HT/toluene solution at 2000 rpm for 120 s. This 1 mg/mL P3HT solution is free of detectable aggregates, evidenced by no presence of adsorption peaks attributed to P3HT aggregates (Figure 2.6). The thickness of the film is determined by AFM measurements (Figure 2.7) to be about 2.7 nm. F_4-TCNQ was applied to the pristine film using "orthogonal doping" method, i.e. immersed in 225 μg/mL F_4-TCNQ in acetonitrile for 60 s followed by 60 s acetonitrile rinsing to remove the possible leftover F_4-TCNQ.

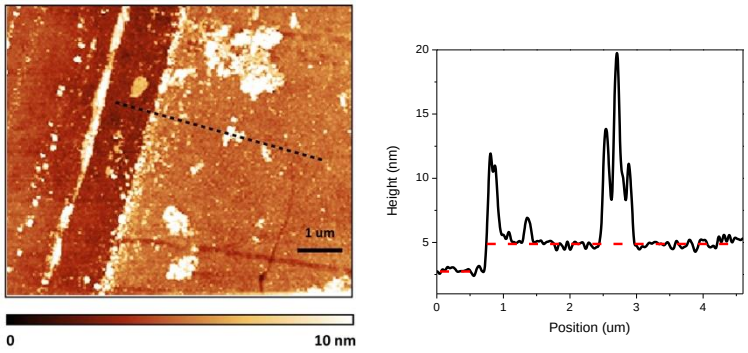

Figure 2.7 *AFM height image of an area of P3HT deposited ITO with a tweezer-made scratch.*

Note: P3HT film is on the right and exposed ITO is on the left. (b) Height profile as marked in (a). The height difference between ITO and P3HT film is about 2.5 nm.

Figure 2.8 shows the morphological AFM images of pristine P3HT film (a) and doped P3HT film (b). Both show characteristics of uniform thin film with surface roughness Ra ~0.5 nm although the thickness of the doped film is increased to 3.7 nm. This is consistent with previous studies showing that "orthogonal doping" does not alter the morphology of the host polymer films.[35] To probe the electronic properties of the films with and without doping, micro-scratches were deliberately made on both films by indentation of an AFM tip. The features of two scratches in Figure 2.8(a) and (b) are similar and the resulting height profiles are shown in Figure 2.8(e) exhibiting the same extent of penetration into the films with a depth of about 4 nm. Since the penetration depth is larger than the film thickness, it can be concluded that those two "scratches" can be regarded as exposed ITO substrate.

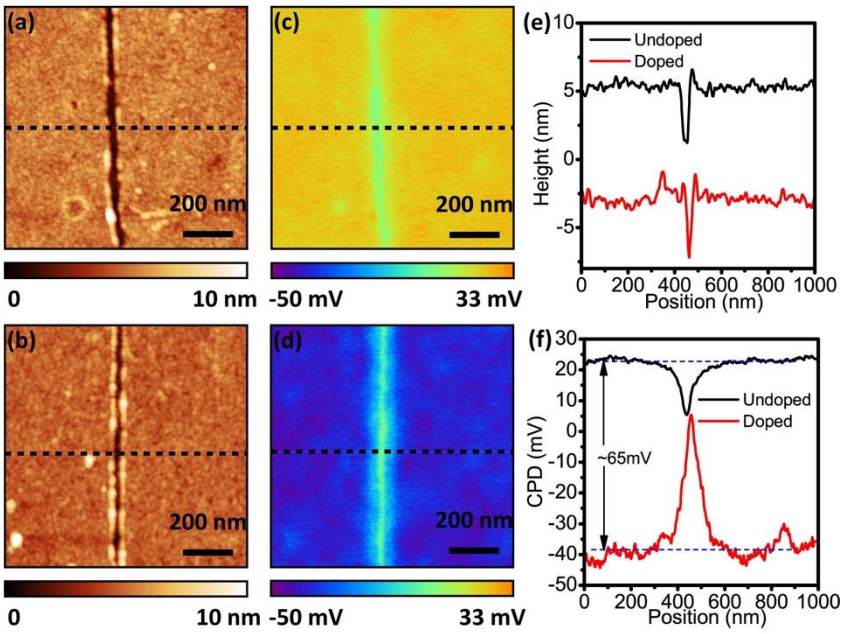

Figure 2.8 *AFM-KPFM results on solid P3HT films before and after doping.*

Note: films are prepared from spin-coating 1 mg/ml LMW P3HT in toluene on ITO substrate with and without subsequent doping in 225 μg/mL F_4-TCNQ acetonitrile solution. Scratch was deliberately made on each film by an AFM tip to expose an ITO slit for sequential height and contact potential difference measurements in semicontact mode. The height profiles of two scratches marked in panel (a) and (b) are shown in panel (e), exhibiting similar penetration depth of about 4nm. However, contact potential difference (CPD) of undoped film and doped film (d) show significant difference referring to the exposed ITO substrate. Panel (f) shows the CPD profiles of both undoped and doped P3HT film as marked in panel (c) and (d). Height profiles were vertically shifted for reading convenience while CPD profiles were not shifted.

In KPFM measurements, an abrupt "dip" in contact potential difference (CPD) can be clearly observed due to the exposure of ITO substrate in undoped P3HT film as shown in Figure 2.8(c). The CPD of undoped P3HT film is about 15 mV higher than that of exposed ITO, which results in the dramatic dip in the CPD profile displayed in Figure 2.8(f). After orthogonal doping by F_4-TCNQ, the CPD of doped P3HT film appear to be relatively homogeneous at microscopic scale, as shown in Figure 2.8(d). This is opposite to isolated dopant sites observed in solution mixed doping samples by conductive AFM.[36] The CPD profile of the doped film in Figure 2.8(f) shows that the CPD of the doped film

is about 50 mV lower than the exposed ITO. This means that the work function of doped P3HT film increases by about 65 mV compared to undoped film, indicating that its Fermi level is mainly decreased by the lowering of HOMO level of the doped film. In addition, the surface dipole induced by F atoms in F_4-TCNQ might also increase the work function of the doped film. The presence of 0-0 and 0-1 vibronic peaks of undoped film in UV-vis (Figure 2.6) confirms the formation of aggregated LMW P3HT from s-P3HT in solution during the drying process of the film. After dipping this pre-aggregated film into a 225 ug/mL F_4-TCNQ solution, the absorption bands of P3HT polaron/bipolaron and F_4-TCNQ anion centred at 768nm and 850 nm appear. Additionally, significant improvement on the conductivity of the P3HT film after sequential doping was demonstrated (Table 2.1). The measured conductivity of doped film is about 0.1 S/cm, which is higher than undoped one ($\sim 10^{-6}$ S/cm) by an order of 10^5. This example demonstrates the effectiveness of sequential doping on pre-aggregated P3HT film by transforming P3HT aggregates into P3HT polarons. This approach apparently follows Mechanism II in Figure 2.1. Herein we have shown films derived from fully solubilized P3HT can undergo aggregation during drying process, which leads to effective doping upon exposure to orthogonal solvent containing dopant molecules.

Table 2.1 *Summary of film Thickness (d) and conductivity (σ) between undoped and doped samples.*

t	d (nm)	σ (S/cm)
	Undoped film	
Device 1	2.65 ± 0.20	4.71×10^{-6}
Device 2		9.14×10^{-6}
Device 3		4.96×10^{-5} (excluded*)
Device 4		9.45×10^{-6}
		Average 7.7×10^{-6}
	Doped film	
Device 1	3.73 ± 0.45	1.24×10^{-1}
Device 2		1.27×10^{-1}
Device 3		1.17×10^{-1}
		Average 1.2×10^{-1}

*This piece of σ data failed in Student's *t*-test with a two-sided 95% confidence level, n=3.

However, it is worthwhile to point out that the doped P3HT film can undergo partial de-doping if it is exposed to a good solvent for F_4-TCNQ, such as acetonitrile. Despite negligible change on the morphology after acetonitrile wash (Figure 2.9(e)), the P3HT film has a significant shift in its CPD value before and after acetonitrile wash. As shown in Figure 2.9(f), the CPD value of the film increases by ~50 mV after wash, which makes it almost indistinguishable as compared to the ITO "scratch". This sharp difference in CPD values of film before and after acetonitrile wash clearly shows that some dopant can be washed away by a good solvent. In another word, doped P3HT film is susceptible to a good solvent of F_4-TCNQ. Thus, from a practical point of view, to preserve good conductive property of a doped P3HT film, it is important to keep it away from good solvents of F_4-TCNQ.

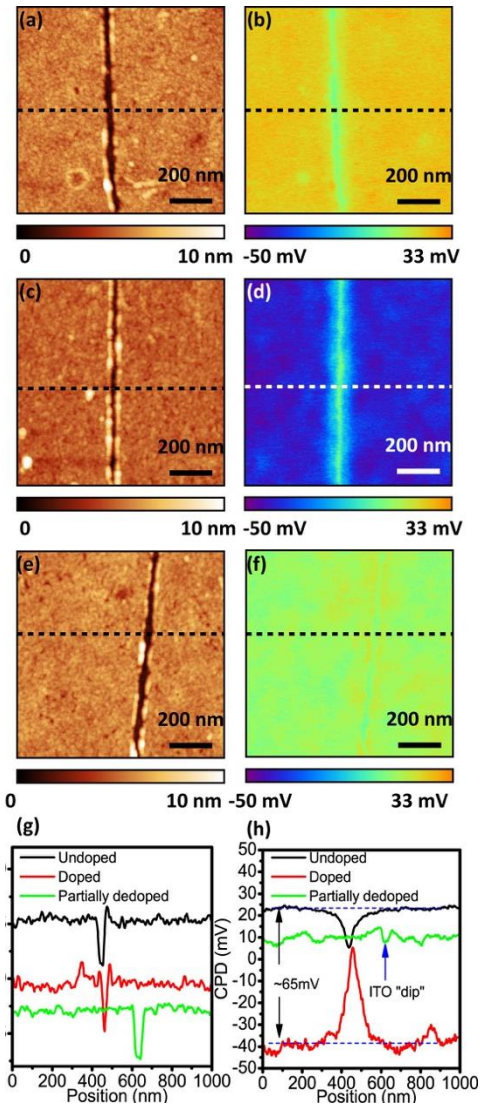

Figure 2.9 *AFM and KPFM results on undoped, doped and partially dedoped P3HT films.*

Note: films are prepared from spin-coating 1 mg/ml LMW P3HT in toluene on ITO substrate with and without subsequent doping in 225 μg/mL F_4-TCNQ acetonitrile solution. AFM morphology of pristine P3HT film (a), doped film (c) and partially dedoped film (e) resembles each other, showing features of a uniform film. Contact potential difference (CPD) of undoped film (b), doped film (d) show significant contrast referring to the exposed ITO substrate. However, "scratch" in the CPD of partially dedoped film (f) is almost indistinguishable. Panel (g) shows the CPD profiles of undoped, doped and partially dedoped P3HT film as marked in panel (b), (d) and (f). CPD of undoped P3HT film (h) is 65 mV higher than doped film and 15 mV higher than ITO. While partially dedoped film (h) has a similar CPD compared to ITO, which is in consist with the lower "visibility" of the scratch in Panel (f). Height profiles were vertically shifted for reading convenience while CPD profiles were not shifted. Arrow in Panel (h) marks the ITO "dip" in the CPD profile for partially dedoped film.

2.4 Conclusion

In conclusion, regioregular LMW-P3HT was used as a model conjugated polymer in a systematic investigation to elucidate the sequence of aggregation and charge transfer in the doping reaction between P3HT and F_4-TCNQ. By excluding possible P3HT aggregation via spontaneous self-assembly and dopant-induced aggregation, we have showed that doping of LMW-P3HT immediately occurs after introducing of an anti-solvent, decane, into a dopant containing P3HT toluene solution. Thus, P3HT aggregation should be regarded as a preferred step for its doping reaction by F_4-TCNQ, which is consistent with the Mechanism II in Figure 2.1. This result was further strengthened by a control experiment on the comparison between pre-aggregated and aggregation free P3HT solutions. By altering antisolvent/solvent ratio, the time scales on accomplishing doping reaction can be easily tuned between minutes and hours. Fully solubilized P3HT can be transformed into aggregated form in a film after drying. The sequential doping of pre-aggregated film leads to little change on the morphology of the film, but a higher work function of doped P3HT film. We hope the results presented here would resolve the real contribution of aggregated P3HT form on its doping reaction and be used in the rational and insightful planning of doping process of conjugated polymer in the applications of organic electronics.

Reference

1. Lüssem, B.; Keum, C. M.; Kasemann, D.; Naab, B.; Bao, Z.; Leo, K., Doped Organic Transistors. *Chem. Rev.* **2016,** *116* (22), 13714-13751.
2. Sekitani, T.; Zschieschang, U.; Klauk, H.; Someya, T., Flexible organic transistors and circuits with extreme bending stability. *Nat. Mater.* **2010,** *9* (12), 1015-1022.
3. Walzer, K.; Männig, B.; Pfeiffer, M.; Leo, K., Highly efficient organic devices based on electrically doped transport layers. *Chem. Rev.* **2007,** *107* (4), 1233-1271.
4. Gelinck, G. H.; Huitema, H. E. A.; Veenendaal, E. V.; Cantatore, E.; Schrijnemakers, L.; Van Der Putten, J. B. P. H.; Geuns, T. C. T.; Beenhakkers, M.; Giesbers, J. B.; Huisman, B. H.; Meijer, E. J.; Benito, E. M.; Touwslager, F. J.; Marsman, A. W.; Van Rens, B. J. E.; De Leeuw, D. M., Flexible active-matrix displays and shift registers based on solution-processed organic transistors. *Nat. Mater.* **2004,** *3* (2), 106-110.
5. Scholes, D. T.; Hawks, S. A.; Yee, P. Y.; Wu, H.; Lindemuth, J. R.; Tolbert, S. H.; Schwartz, B. J., Overcoming Film Quality Issues for Conjugated Polymers Doped with F4TCNQ by Solution Sequential Processing: Hall Effect, Structural, and Optical Measurements. *J. Phys. Chem. Lett.* **2015,** *6* (23), 4786-4793.
6. Aziz, E. F.; Vollmer, A.; Eisebitt, S.; Eberhardt, W.; Pingel, P.; Neher, D.; Koch, N., Localized charge transfer in a molecularly doped conducting polymer. *Adv. Mater.* **2007,** *19* (20), 3257-3260.
7. Wang, G.; Huang, W.; Eastham, N. D.; Fabiano, S.; Manley, E. F.; Zeng, L.; Wang, B.; Zhang, X.; Chen, Z.; Li, R.; Chang, R. P. H.; Chen, L. X.; Bedzyk, M. J.; Melkonyan, F. S.; Facchetti, A.; Marks, T. J., Aggregation control in natural brush-printed conjugated polymer films and implications for enhancing charge transport. *Proc. Natl. Acad. Sci. U.S.A.* **2017,** *114* (47), E10066-E10073.
8. Xu, Y.; Liu, C.; Khim, D.; Noh, Y.-Y., Development of high-performance printed organic field-effect transistors and integrated circuits. *Phys. Chem. Chem. Phys.* **2015,** *17* (40), 26553-26574.
9. Baeg, K. J.; Khim, D.; Kim, D. Y.; Jung, S. W.; Koo, J. B.; You, I. K.; Yan, H.; Facchetti, A.; Noh, Y. Y., High speeds complementary integrated circuits fabricated with all-printed polymeric semiconductors. *J. Polym. Sci., Part B: Polym. Phys.* **2011,** *49* (1), 62-67.
10. Voigt, M. M.; Cuite, A.; Chung, D. Y.; Khan, R. U. A.; Campbell, A. J.; Bradley, D. D. C.; Meng, F.; Steinke, J. H. G.; Tierney, S.; McCulloch, L.; Penxten, H.; Luisen, L.; Douheret, O.; Manca, J.; Brokmann, U.; Sönnichsen, K.; Hülsenberg, D.; Bock, W.; Barron, C.; Blanckaert, N.; Springer, S.; Grupp, J.; McSley, A., Polymer field-effect transistors fabricated by the sequential gravure printing of polythiophene, two insulator layers, and a metal ink gate. *Adv. Funct. Mater.* **2010,** *20* (2), 239-246.
11. Yan, H.; Chen, Z.; Zheng, Y.; Newman, C.; Quinn, J. R.; Dötz, F.; Kastler, M.; Facchetti, A., A high-mobility electron-transporting polymer for printed transistors. *Nature* **2009,** *457* (7230), 679-686.
12. McFarland, F. M.; Brickson, B.; Guo, S., Layered poly(3-hexylthiophene) nanowhiskers studied by atomic force microscopy and Kelvin probe force microscopy. *Macromolecules* **2015,** *48* (9), 3049-3056.

13. Gao, J.; Stein, B. W.; Thomas, A. K.; Garcia, J. A.; Yang, J.; Kirk, M. L.; Grey, J. K., Enhanced Charge Transfer Doping Efficiency in J-Aggregate Poly(3-hexylthiophene) Nanofibers. *J. Phys. Chem. C* **2015,** *119* (28), 16396-16402.
14. McFarland, F. M.; Bonnette, L. R.; Acres, E. A.; Guo, S., The impact of aggregation on the p-doping kinetics of poly(3-hexylthiophene). *J. Mater. Chem. C* **2017,** *5* (23), 5764-5771.
15. Méndez, H.; Heimel, G.; Winkler, S.; Frisch, J.; Opitz, A.; Sauer, K.; Wegner, B.; Oehzelt, M.; Röthel, C.; Duhm, S.; Többens, D.; Koch, N.; Salzmann, I., Charge-transfer crystallites as molecular electrical dopants. *Nat. Commun.* **2015,** *6*, 1-11.
16. Tsoi, W. C.; Spencer, S. J.; Yang, L.; Ballantyne, A. M.; Nicholson, P. G.; Turnbull, A.; Shard, A. G.; Murphy, C. E.; Bradley, D. D.; Nelson, J., Effect of crystallization on the electronic energy levels and thin film morphology of P3HT: PCBM blends. *Macromolecules* **2011,** *44* (8), 2944-2952.
17. McFarland, F. M.; Ellis, C. M.; Guo, S., The Aggregation of Poly(3-hexylthiophene) into Nanowires: With and without Chemical Doping. *J. Phys. Chem. C* **2017,** *121* (8), 4740-4746.
18. Newbloom, G. M.; de la Iglesia, P.; Pozzo, L. D., Controlled gelation of poly(3-alkylthiophene)s in bulk and in thin-films using low volatility solvent/poor-solvent mixtures. *Soft Matter* **2014,** *10* (44), 8945-8954.
19. Chang, M.; Choi, D.; Fu, B.; Reichmanis, E., Solvent based hydrogen bonding: Impact on poly(3-hexylthiophene) nanoscale morphology and charge transport characteristics. *ACS Nano* **2013,** *7* (6), 5402-5413.
20. Oh, J. Y.; Shin, M.; Lee, T. I.; Jang, W. S.; Min, Y.; Myoung, J. M.; Baik, H. K.; Jeong, U., Self-seeded growth of poly(3-hexylthiophene) (P3HT) nanofibrils by a cycle of cooling and heating in solutions. *Macromolecules* **2012,** *45* (18), 7504-7513.
21. Xu, W.; Li, L.; Tang, H.; Li, H.; Zhao, X.; Yang, X., Solvent-Induced crystallization of poly(3-dodecylthiophene): Morphology and kinetics. *J. Phys. Chem. B* **2011,** *115* (20), 6412-6420.
22. He, M.; Zhao, L.; Wang, J.; Han, W.; Yang, Y.; Qiu, F.; Lin, Z., Self-Assembly of All-Conjugated Poly(3- alkylthiophene) Diblock Copolymer Nanostructures from Mixed Selective Solvents. *ACS Nano* **2010,** *4* (6), 3241-3247.
23. Samitsu, S.; Shimomura, T.; Heike, S.; Hashizume, T.; Ito, K., Effective Production of Poly (3-alkylthiophene) Nanofibers by means of Whisker Method using Anisole Solvent : Structural , Optical , and Electrical Properties Effective Production of Poly (3-alkylthiophene) Nanofibers by means of Whisker Method using. *Macromolecules* **2008,** *41* (21), 8000-8010.
24. Kiriy, N.; Jähne, E.; Adler, H. J.; Schneider, M.; Kiriy, A.; Gorodyska, G.; Minko, S.; Jehnichen, D.; Simon, P.; Fokin, A. A.; Stamm, M., One-dimensional aggregation of regioregular polyalkylthiophenes. *Nano Lett.* **2003,** *3* (6), 707-712.
25. Wang, C.; Duong, D. T.; Vandewal, K.; Rivnay, J.; Salleo, A., Optical measurement of doping efficiency in poly(3-hexylthiophene) solutions and thin films. *Phys. Rev. B* **2015,** *91* (8), 1-7.

26. Clark, J.; Silva, C.; Friend, R. H.; Spano, F. C., Role of intermolecular coupling in the photophysics of disordered organic semiconductors: Aggregate emission in regioregular polythiophene. *Phys. Rev. Lett.* **2007,** *98* (20), 1-4.
27. Brown, P. J.; Thomas, D. S.; Köhler, A.; Wilson, J. S.; Kim, J. S.; Ramsdale, C. M.; Sirringhaus, H.; Friend, R. H., Effect of interchain interactions on the absorption and emission of poly(3-hexylthiophene). *Phys. Rev. B: Condens. Matter Mater. Phys.* **2003,** *67* (6), 1-16.
28. Gao, J.; Niles, E. T.; Grey, J. K., Aggregates promote efficient charge transfer doping of Poly(3- hexylthiophene). *J. Phys. Chem. Lett.* **2013,** *4* (17), 2953-2957.
29. Duong, D. T.; Wang, C.; Antono, E.; Toney, M. F.; Salleo, A., The chemical and structural origin of efficient p-type doping in P3HT. *Org. Electron.* **2013,** *14* (5), 1330-1336.
30. Savenije, T. J.; Kroeze, J. E.; Yang, X.; Loos, J., The formation of crystalline P3HT fibrils upon annealing of a PCBM: P3HT bulk heterojunction. *Thin Solid Films* **2006,** *511*, 2-6.
31. Skompska, M.; Szkurłat, A., The influence of the structural defects and microscopic aggregation of poly (3-alkylthiophenes) on electrochemical and optical properties of the polymer films: discussion of an origin of redox peaks in the cyclic voltammograms. *Electrochim. Acta* **2001,** *46* (26-27), 4007-4015.
32. Thomas, A. K.; Johnson, R.; Stein, B. W.; Kirk, M. L.; Guo, H.; Grey, J. K., Charge Transfer Doping Induced Conformational Ordering of a Non-Crystalline Conjugated Polymer. *J. Phys. Chem. C* **2017,** *121* (42), 23817-23826.
33. Cochran, J. E.; Junk, M. J. N.; Glaudell, A. M.; Miller, P. L.; Cowart, J. S.; Toney, M. F.; Hawker, C. J.; Chmelka, B. F.; Chabinyc, M. L., Molecular interactions and ordering in electrically doped polymers: Blends of PBTTT and F4TCNQ. *Macromolecules* **2014,** *47* (19), 6836-6846.
34. Gao, J.; Roehling, J. D.; Li, Y.; Guo, H.; Moulé, A. J.; Grey, J. K., The effect of 2,3,5,6-tetrafluoro-7,7,8,8-tetracyanoquinodimethane charge transfer dopants on the conformation and aggregation of poly(3-hexylthiophene). *J. Mater. Chem. C* **2013,** *1* (36), 5638-5646.
35. Jacobs, I. E.; Aasen, E. W.; Oliveira, J. L.; Fonseca, T. N.; Roehling, J. D.; Li, J.; Zhang, G.; Augustine, M. P.; Mascal, M.; Moulé, A. J., Comparison of solution-mixed and sequentially processed P3HT:F4TCNQ films: effect of doping-induced aggregation on film morphology. *J. Mater. Chem. C* **2016,** *4* (16), 3454-3466.
36. Duong, D. T.; Phan, H.; Hanifi, D.; Jo, P. S.; Nguyen, T. Q.; Salleo, A., Direct observation of doping sites in temperature-controlled, p-doped p3ht thin films by conducting atomic force microscopy. *Adv. Mater.* **2014,** *26* (35), 6069-6073.

CHAPTER III - Chemical Doping of Well-Dispersed P3HT Thin-Film Nanowire Networks

In Chapter III, we demonstrate the preparation of uniformly distributed poly(3-hexylthiophene) (P3HT) nanowire (NW) networks on a variety of substrates. We studied changes in the optical, electronic, and morphological properties upon sequential doping by 2,3,5,6-tetrafluoro-7,7,8,8-tetracyanoquinodimethane (F4TCNQ) by UV-Vis spectroscopy, atomic force microscopy (AFM), Kelvin probe force microscopy (KPFM), and electrical conductivity measurements. At a moderate dopant concentration of 250 μg/mL, the P3HT NW networks retain their morphological features with a clear evolution of an absorption band corresponding to doping products. Higher dopant concentrations (~1 mg/mL) lead to the accumulation of dopant molecules on the surface of the film forming "dot-like" features. KPFM measurements show a clear difference in the contact potential difference (CPD) of the P3HT NWs with varying doping concentration regimes. Moreover, an increase in the electrical conductivity by four orders of magnitude from 10^{-5} S/cm to 10^{-1} S/cm is observed after moderate doping demonstrating that significant doping effects can be achieved for a mostly crystalline phase of P3HT such as its nanowire form.

3.1 Introduction

The chemical doping of conjugated polymers (CPs) remains one of the most widely utilized methods to manipulate the optical and electronic properties of these materials and

increase the electrical conductivity. This has resulted in a diversity of technologies such as field effect transistors (FETs),[1-3] organic light-emitting diodes (OLEDs)[4], and sensors[5] with numerous new applications continually emerging. Among methods of chemically doping CPs, solution-based methods offer low-cost, convenience, and compatibility with solution-processing methods most commonly utilized for device fabrication.[1-3] There are generally two solution-based approaches used to dope CPs. The first, mixed solution doping, constitutes the mixing of dopant molecules with the polymers before the formation of the active layer. However, due to the complex intermolecular interactions resulting from charge transfer between dopant molecules and CPs, and the decreased solubility of the doped products, this method often leads to non-ideal morphological characteristics upon film formation.[6, 7] Another method, sequential doping, relies on the application of a dopant solution to the surface of the CP film. Sequential doping provides a valuable route to overcome the difficulties associated with processing doped poly(3-hexylthiophene) (P3HT) from solution and results in better film quality and enhanced electrical conductivity.[6-8]

Despite the extensive studies carried out with P3HT as a semiconductor in a variety of applications, there are still a relatively limited number of studies related to P3HT nanowire (NW) structures. These structures can be accessed via controlled seeding,[9-11] electric field-assisted alignment[12-16] or electrospinning.[17-22] The "whisker method" provides high-aspect-ratio P3HT nanofibers, which crystallize from "poor" solvents.[23] P3HT NW samples can be prepared via solution deposition of aggregated P3HT nanowhiskers onto a suitable substrate by solution casting methods,[24-32] which often lead

to heterogeneous coverage of NWs on surfaces. The characterization of isolated P3HT NWs has been previously reported.[33-37] Despite the significance of understanding the fundamental electrical properties of isolated NWs, the extensive lithographic techniques involved in accessing these structures hinder practical device applications and provide a limited understanding of their ensemble optoelectronic properties. In order to utilize P3HT NW networks in optoelectronic devices, a more uniform distribution of P3HT NWs on the surface is preferred.[38, 39]

Here, we demonstrate that P3HT NW networks can be prepared by spin-coating a P3HT nanowhisker solution formed at a low P3HT concentration of 60 μg/mL. Doping of the nanowire network is carried out using 7,7,8,8-tetracyano-2,3,5,6-tetrafluoroquinodimethane (F4TCNQ), a prototypical p-type dopant for P3HT.[40-44] Results from atomic force microscopy (AFM) and Kelvin probe force microscopy (KPFM) measurements are used to distinguish undoped, moderately doped, and excessively doped P3HT NW networks and offer insight into their electronic properties. Furthermore, an increase in the electrical conductivity by four orders of magnitude from 10^{-5} S/cm to 10^{-1} S/cm is observed after moderate chemical doping of the P3HT NW networks.

3.2 Materials and Methods

3.2.1 Materials

Solvents, unless otherwise specified, were purchased from Fisher Scientific and used without additional purification. Regioregular (RR) P3HT (M_n = 70.5 kDa, Dispersity ($Đ$) = 1.7, head-to-tail (H-T) regioregularity > 98%) was purchased from Sigma-Aldrich. F4TCNQ (> 98%) was purchased from TCI America and used as received. Indium tin oxide

(ITO) coated glass substrates were purchased from Colorado Concept Coating, LLC, USA. Glass slides (2 cm × 2 cm × 0.17 mm) were purchased from Fisher Scientific, USA. Quartz substrates (S151) for conductivity measurements were purchased from Ossila, Ltd., UK.

3.2.2 Nanowire preparation

2.4 mg of RR-P3HT was added to 40 mL of an 4:1 (v/v) anisole/chloroform mixture .[38, 39] The resultant 60 μg/mL P3HT solution was heated at 90 °C for 15 minutes until an orange solution was obtained. The P3HT solution was subsequently cooled to 25 °C at a rate of 25 °C/h controlled by a Quantum Northwest TC1 temperature controller and then aged at that temperature for 18 h. After aging, the orange-colored P3HT solution became purple indicating the formation of NWs.

3.2.3 Characterization

UV-Vis absorption spectra were recorded on an Agilent Cary 60 UV-Vis spectrometer. For solution absorption measurements, P3HT was dissolved in a 4:1 (v/v) anisole/chloroform mixture at a concentration of 60 μg/mL and transferred into airtight custom-made cuvettes (2 mm optical path length). For solid-state absorption experiments, glass slides (0.17 mm thick) were cleaned by dipping in hot concentrated HNO_3 for 15 min, followed by rinsing in deionized water before use. An aged 60 μg/mL P3HT solution was spin-coated at 3000 rpm for 120 s to form P3HT NW networks. Doped samples were prepared by covering the P3HT-coated substrate with solutions of F4TCNQ in acetonitrile for 15 s. The liquid was subsequently removed from the surface by spinning at 2000 rpm for 30 s.

The 1 × 1 cm ITO substrates were ultrasonicated in a 1:1:1 mixture of chlorobenzene, toluene, and acetone for 15 minutes and then heated at 90°C for 15 min. Next, the substrates were soaked in toluene, which was previously filtered through a 0.25 μm pore size membrane filter and subsequently blown dry under a flow of nitrogen before use. The preparation of pristine and doped P3HT NWs on ITO substrates follows the same protocol as previously described on a glass substrate. AFM and KPFM measurements were performed on an NTEGRA Prima AFM from NT-MDT Spectrum Instruments. Both topography and KPFM images were collected using Pt-coated silicon tips (NSC18-Pt) from μMasch with a typical resonant frequency of 75 kHz and a spring force constant of 1.2−5.5 N/m. Topography imaging was performed using semi-contact mode. Two-pass lift mode was used in KPFM measurements. The first KPFM pass was performed in semi-contact mode. Tracing the recorded topography scan, a second pass with a lift height of 10 nm could resolve the contact potential difference (CPD) between the tip and surface features. The surface coverage (ϕ) of P3HT NW networks on the ITO substrate is determined by using the mark grains module in Gwyddion software (http://gwyddion.net/, Czech Metrology Institute). The difference in CPD values between P3HT NWs and the ITO region can be regarded as the difference in their work functions without concerning work function variations of the AFM tip.

3.2.4 Device Fabrication and Charge Transport Measurements

Quartz substrates were sequentially cleaned by ultrasonication in detergent (2% Hellmanex in deionized water), deionized water, acetone, and isopropyl alcohol for 15 min each followed by drying in an oven. Gold (Au) electrodes (60 nm) were thermally

deposited on quartz at 10^{-6} torr using a patterned shadow mask, resulting in a well-defined channel length (L) of 30 μm and width (W) of 1 mm. Undoped and doped P3HT NW networks were prepared following the same protocol that was used for glass and ITO substrates. Devices were tested on a Signatone 1160 series probe station coupled to a Keithley 4200 semiconductor characterization system inside a nitrogen-filled glovebox. The conductivity of the P3HT NW networks was calculated from following expression,

$$\sigma = G\frac{L}{\phi W h_a} \qquad \text{(Eq. 3.1)}$$

where G is the conductance, L is the channel length, W is the channel width, and h_a is the average thickness/height of the NW network, respectively. G of each device is interpreted from the slope of its current-voltage (I-V) characteristic curve. ϕ is defined as the surface coverage of the P3HT nanowire networks. Note that the product ϕW can be regarded as the effective width of the network W_{eff} between two 30 μm-channel length Au electrodes. For the undoped and doped sample, the reported conductivity was averaged from 10 devices.

3.3 Results and Discussion

3.3.1 Aggregation type and crystallinity of P3HT nanowires

As shown in Figure 3.1(a), an absorption maximum (λ_{max}) at 445 nm was observed for P3HT in a 4:1 (v/v) anisole/chloroform mixture corresponding to fully solubilized P3HT.[45-47] Following controlled aging at 25 °C, there is a bathochromic shift in the absorption profile with two peaks at 603 nm and 553 nm in the adsorption band, which can be assigned as the 0-0 and 0-1 vibronic transitions of the P3HT aggregate, respectively.[48-50] After aging, no significant absorption peak can be observed at 445 nm. The $A_{0\text{-}0}/A_{0\text{-}1}$

ratio indicates whether aggregates show H- or J-type character.[48-50] Here, a ratio of 0.66 corresponds to the formation of H-aggregates as $A_{0\text{-}0}/A_{0\text{-}1} < 1$. By assuming a Huang−Rhys factor of 1, the free exciton bandwidth (*W*) of the H-aggregate can be determined from the following expression,[48-50]

$$\frac{A_{0-0}}{A_{0-1}} \approx \left(\frac{1 - \frac{0.24W}{\hbar\omega_0}}{1 + \frac{0.073W}{\hbar\omega_0}} \right)^2 \qquad \text{(Eq. 1.5)}$$

where Ep is the energy of dominating intramolecular *C=C* vibrations that are assumed to be at 0.18 eV.[51, 52] The calculated *W* for the P3HT aggregate in this binary solvent is about 113 meV, comparable to the value of solid-state P3HT films prepared from low boiling point solvents such as chloroform.[47, 53, 54] The absorbance at 445 nm is reduced in intensity by 55% when compared to the fully solubilized P3HT, indicating the formation of 45% crystalline P3HT.

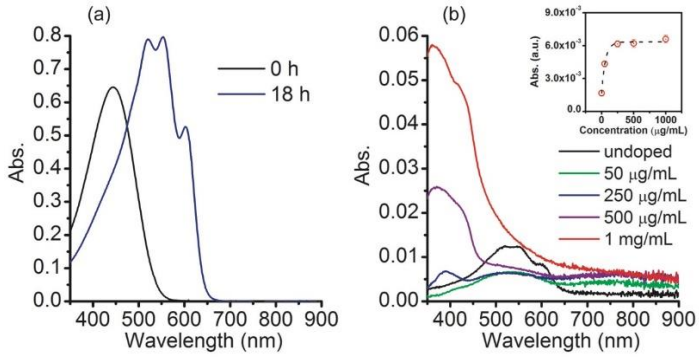

Figure 3.1 *UV-Vis absorption spectra of undoped and doped P3HT nanowires in solution and solid states.*

Note: (a) UV-Vis absorption spectra of P3HT in 4:1 (v/v) anisole/chloroform solvent in the fully solubilized state (t = 0 h, T = 90 °C) and aggregated state (t = 18 h, T = 25 °C). The cooling rate was 25 °C/h and the temperature was held constant once 25 °C was reached. (b) UV-Vis absorption spectra of P3HT NWs on glass slides. F4TCNQ solutions in acetonitrile with concentrations from 0 to 1 mg/mL were applied to the surface, resulting in the formation of a wide absorbance band above 650 nm that is attributed to P3HT polarons and F4TCNQ anions. Inset: Absorbance at 768 nm as a function of dopant concentration.

Alternatively, the absorption spectra of aged P3HT solution can be deconvoluted into a combination of fully solubilized absorption band $A_{s\text{-}P3HT}$ and aggregate absorption $A_{NW\text{-}P3HT}$ following previously reported methods.[45, 55, 56] The analysis shows that 48% P3HT is converted into the H-aggregate state after aging (Figure 3.2), which is comparable to previously reported values of approximately 50%.[11, 54] The disappearance of the peak at 450 nm has been used as an indicator of the formation of purely (~100%) crystalline P3HT and as a reference to estimate the crystallinity of less crystalline samples.[57] Despite the discrepancy on the precise determination of P3HT crystallinity in solution, it is reasonable to conclude that aged P3HT formed following this approach shows significant crystallinity.

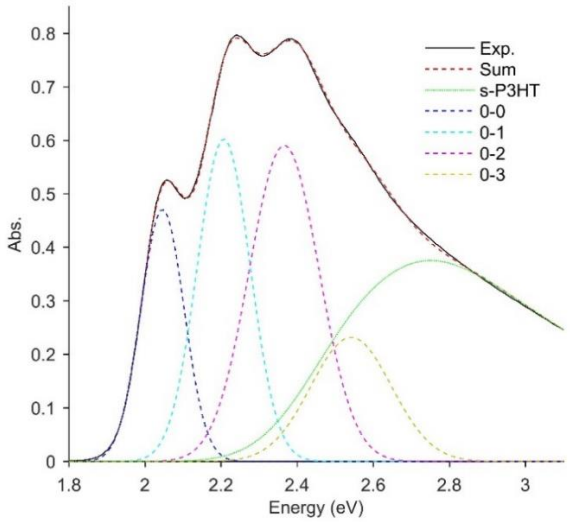

Figure 3.2 *Deconvolution of the spectrum of the aged P3HT solution.*

Note: blue curve in Figure 3.1(a) can be decomposed into fully solubilized s-P3HT and 4 vibronic transitions associated with H aggregates of P3HT. The total absorbance can be expressed using the following formula: $A_{total} = A_{S-P3HT} + A_{NW-P3HT} = F_{S-P3HT}A^0_{S-P3HT} + A_{0-0} + A_{0-1} + A_{0-2} + A_{0-3}$.[1] A^0_{S-P3HT} is the absorbance of solubilized P3HT solution, and F_{S-P3HT} is the fraction of s-P3HT in the aged solution. $A_{nw-P3HT}$ is decomposed into 4 Gaussian peaks with non-uniform widths representing the 0-0, 0-1, 0-2, and 0-3 vibronic transitions of P3HT NWs.[2-4] The vibronic peaks are centered at 2.05 eV, 2.21 eV, 2.37 eV, and 2.54 eV. After fitting, $F_{S-P3HT} = 0.52$, indicating a crystallinity of 0.48 in the aged solution. The fitting is carried out with Curve Fitting Toolbox in MATLAB 2016a.

3.3.2 Doping of P3HT nanowires on surface: a UV-vis study

The P3HT NWs formed can be deposited onto glass substrates for solid-state UV-Vis measurements through spin-coating (Figure 3.1(b)). Due to the dramatic reduction of the absorbance of P3HT NWs on the surface as compared to solution samples, the signal to noise ratio of the spectra decreases. Meanwhile, the absorption peaks of the undoped P3HT NWs assigned to the 0-0 and 0-1 transition are slightly shifted to 602 nm and 546 nm, respectively. The $A_{0\text{-}0}/A_{0\text{-}1}$ ratio is 0.67, which is very close to the ratio in solution implying that the H-aggregate character remains after deposition. Upon sequential doping with a 50 μg/mL F4TCNQ solution, the aggregate absorption peaks decrease, accompanied by the emergence of a broad absorption band above 650 nm. This is due to the formation of P3HT polarons as a result of integer charge transfer between P3HT and F4TCNQ.[45, 58] The 768 nm and 850 nm peaks associated with absorption by F4TCNQ anions cannot be resolved as a result of the sensitivity limits of the instrumentation.[45, 46, 58, 59]

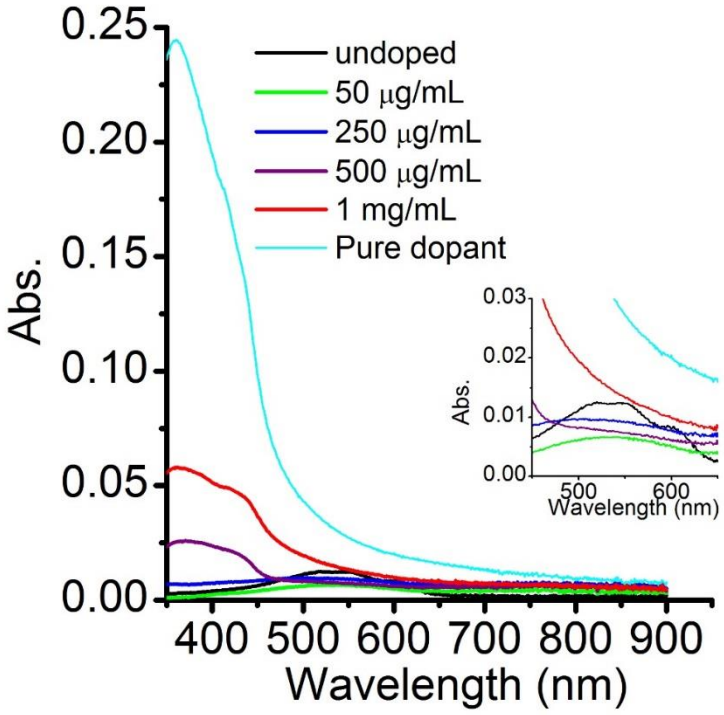

Figure 3.3 *UV-Vis spectrum of pure F_4-TCNQ dopant presented together with P3HT NWs under different doping conditions as described in Figure 3.1(b).*

Note: pure F_4-TCNQ film was deposited on a glass slide by drop-casting. Inset shows amplified spectra from 450 nm to 650 nm.

Despite this limitation, the progress of sequential doping upon increasing dopant concentration can be tracked by monitoring the absorbance at 768 nm, which can be attributed to doping products. In the inset of Figure 3.1(b), the absorbance at 768 nm sharply increases as a function of F4TCNQ concentration and saturates at a solution concentration greater than 250 μg/mL. As the dopant concentration further increases above 500 μg/mL, the absorbance between 550 nm and 615 nm increases. This is likely due to the absorbance attributed to excess neutral F4TCNQ (λ_{max} = 380 nm, Figure 3.3).

3.3.3 Doping of P3HT nanowires on surface: a KPFM study

P3HT NWs were spin-coated onto ITO substrates for a detailed analysis of these nanostructures using AFM. In Figure 3.4(a), a 5 × 5 μm overview of pristine P3HT NWs shows high aspect ratio P3HT NWs on the order of several μm in length that are uniformly distributed on the surface, and which form an interconnected NW network. According to statistical analyses, the average height of undoped P3HT NWs is around 3.3 nm with a surface coverage around 33% (Table 3.1).

Table 3.1 *Statistical quantities of undoped and doped P3HT nanowire networks.*

Note that in 1 mg/mL doped cases, a significant presence of excessive dopant was observed on the surface. Therefore, surface coverage is from the P3HT NW network and excessive dopant.

Statistics	NWs			Excessive dopant		
	Average height (nm)	RMS (nm)	Surface coverage %	Average height (nm)	RMS (nm)	Surface coverage %
undoped	3.3	1.8	33	-	-	-
250 μg/mL	4.3	2.1	34	-	-	-
1 mg/mL	4.8	2.9	31	18.4	5.5	10

A similar morphology with evenly dispersed P3HT NWs is shown in the first pass topography results obtained using KPFM (Figure 3.4(b)), while the higher resolution image highlights the areas where multiple NWs overlap.

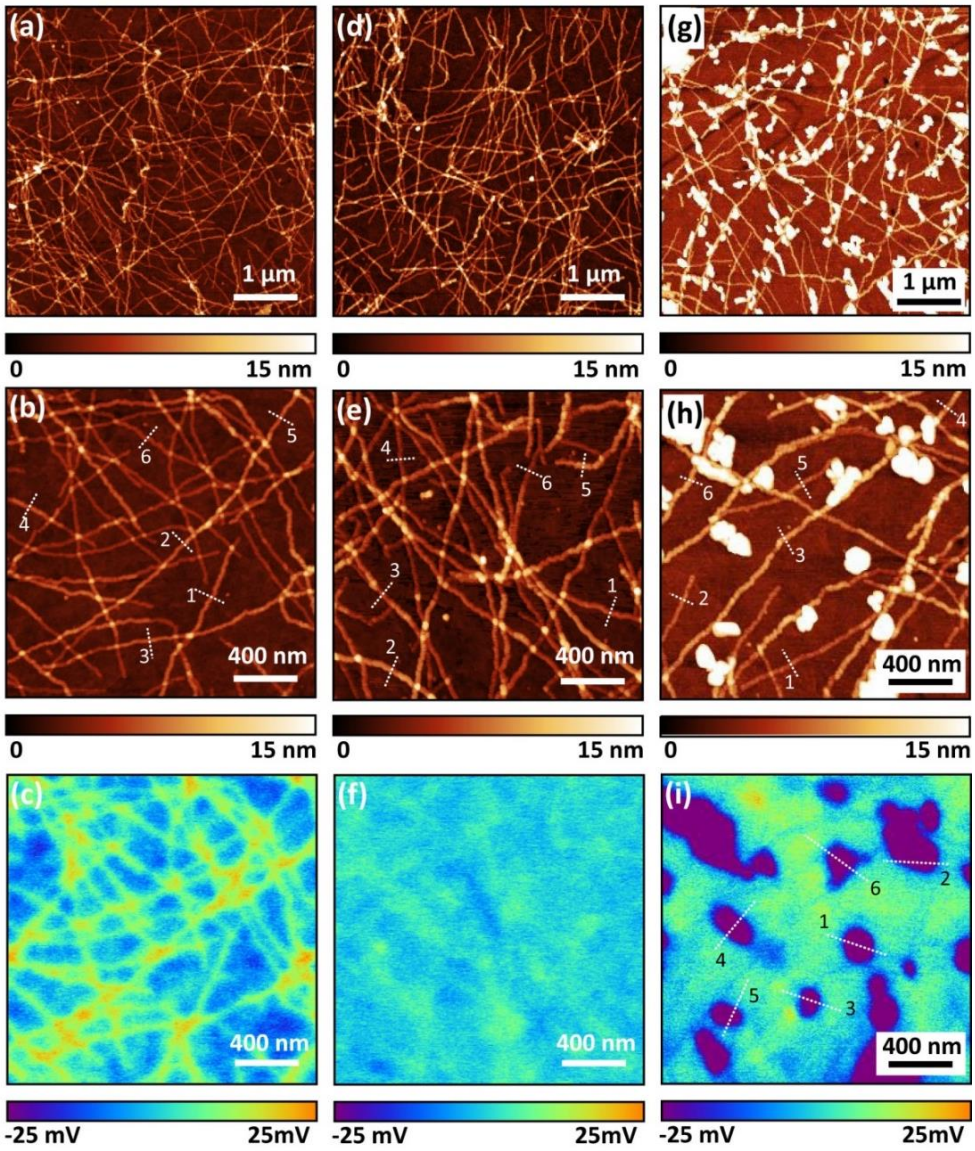

Figure 3.4 *AFM and KPFM results of undoped and doped P3HT nanowires on surface.*

Note: (a) AFM topography image of P3HT nanowires on ITO. A magnified 2 × 2 µm image is shown in the panel (b). The KPFM image of pristine P3HT NW network (c) presents a distinguishable 10 mV CPD contrast between NWs and the ITO substrate. Sequentially doped P3HT NWs with 250 µg/mL F4TCNQ retain the morphology of pristine NWs (d, e) while the average thickness of NWs increases. Noticeably, KPFM result in panel (f) shows CPD of NWs and ITO becomes indistinguishable. Upon 1 mg/mL F4TCNQ sequential doping of P3HT, irregular dot-like features associated with excessive neutral dopant emerge (g,h), showing significantly lower CPD values as compared to the doped NWs and the ITO substrate. The height profiles of marked cross-sections (1-6) in panel (b), (e) are summarized and can be found in Figure 3.5. While the CPD profiles of marked cross-sections (1-6) in panel (i) can be referred to Figure 3.6.

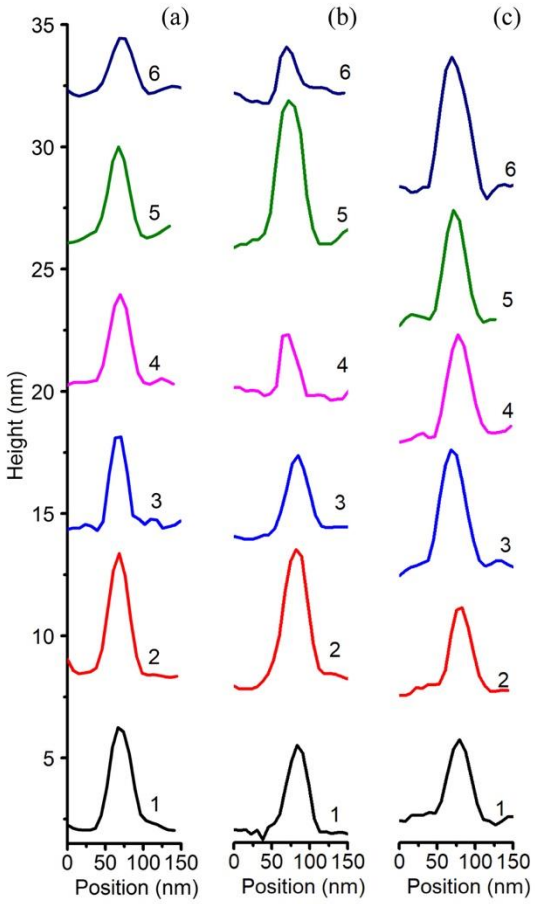

Figure 3.5 *Typical cross-section height profiles of P3HT NWs on ITO substrate.*

Note: profiles as marked by dotted lines in Figure 3.4(b), (e) and (h), associated with panel (a) as-deposited, (b) sequentially doped with 250 μg/mL F4TCNQ and (c) sequentially doped with 1 mg/mL F4TCNQ, respectively.

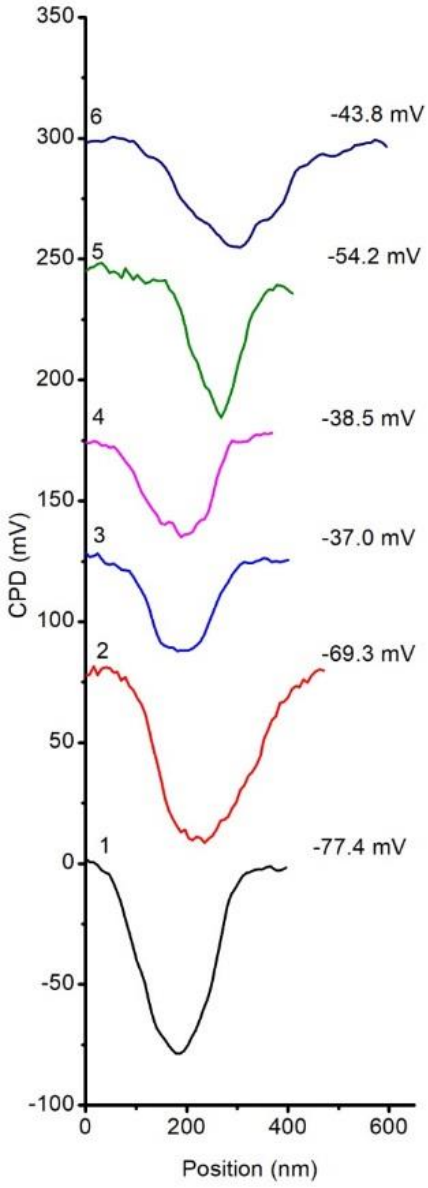

Figure 3.6 *Contact potential difference (CPD) profiles of corresponding marked cross-sections 1-6 in the KPFM image (Figure 3.4(f)) of doped P3HT nanowires (NWs).*

Six cross-sectional height profiles of random isolated NWs marked with dotted lines were sampled (Table 3.2). Since the statistical average thickness of P3HT NWs is around 3.3 nm, the NW network largely consists of double and triple layers. Interestingly,

unlike our previous report on P3HT nanowhiskers where P3HT monolayers were more common,[25] no monolayer is observed here. This phenomenon can likely be attributed to the relatively long aging time of 18 hours during which P3HT monolayers aggregate into more stable multilayered structures. No multilayered structures thicker than quadruple layers are observed, which may originate from the low P3HT concentration of 60 μg/mL.

Table 3.2 *Summary on the heights of P3HT NWs on ITO substrate as marked by dotted lines in Figure 3.4(b), (e) and (h).*

	Height (nm)					
NWs sampling	1	2	3	4	5	6
undoped	4.0	4.9	3.7	3.6	3.8	2.3
250 μg/mL	3.6	5.2	3.0	2.5	5.8	2.6
1 mg/mL	3.3	3.4	4.7	4.2	4.5	5.4

When a moderate amount of F4TCNQ (i.e. 250 μg/mL) was applied to the pristine P3HT NWs, the overall network-like morphology remains intact (Figure 3.4(d)). Therefore, sequential doping does not drastically interfere with the structure of the nanostructures, which helps to preserve the crystallinity and domain orientation.[6-8] From the data in Table 3.1, the average thickness of the moderately doped P3HT NWs is about 4.3 nm, which is about 1 nm larger than the pristine NWs. Upon applying a larger amount of F4TCNQ (i.e. 1 mg/mL), dot-like features with sub-micrometer size can be observed on the surface (Figure 3.4(g)), which are attributed to neutral dopant. The excess dopant on the surface not only increases the average thickness of the NWs by about 1.5 nm, but also introduces an additional surface coverage of about 10% (Table 3.1). Despite the drastic difference in

the overall morphology between moderately doped and excessively doped surfaces, the surface coverage of the P3HT NWs remains at about 33%, confirming the minor effect associated with sequential doping on the existing structures. However, due to dopant deposition, the sampled cross-section heights of NWs increase in both doped cases (Table 3.2), resulting in an increase of layer thicknesses when compared to undoped NWs. The precise location where the F4TCNQ dopant resides within P3HT film remains elusive. From grazing-incidence wide-angle X-ray scattering (GIWAXS) studies on P3HT films derived from conventional mixed solution doping, Duong et al. first reported that the in-plane (010) peak at q ~1.65 $Å^{-1}$, which corresponds to π-π spacing of 3.81 Å, splits into two peaks when sufficiently high doping of P3HT is achieved in solution.[59] Méndez et al. suggested the shifts of the (010) peaks can be attributed to the intercalation of dopant into the π-π stacks of the P3HT backbones as a result of the formation of P3HT/F4TCNQ mixed co-crystallite phase from mixed solution doping.[60] However, according to Scholes et al., the intercalation of F4TCNQ into the P3HT π-stacks is not evident in both mixed solution and sequential doping methods.[7] Instead, they claimed that the change in π-π spacing is due to the incorporation of the dopant into lamellar domains regardless of doping methods (solution mixing or sequential doping), which not only shifts side chain packing but also alters the π-π stacking due to the dopant-induced inter-chain delocalization of polarons, which results in pulling adjacent polymer chains closer.[7] Despite the ongoing discussion on whether the dopant intercalates into π-π stacks in P3HT films, the doping approach in this work may not lead to the infiltration of P3HT NWs into π-stacks because orthogonal solvents such as acetonitrile have a minimal swelling effect on the crystalline phase of

P3HT.[8] Thus, intercalation of dopants into π-stacks of P3HT NWs during sequential doping seems unlikely. Additionally, upon doping, the shift of (100) peaks to the lower *q* region (increased lamellar *d* spacing) in GIWAXS indicates the possible incorporation of dopants into the lamellar region.[7, 46, 59, 60] Based on this, the F4TCNQ dopant could reside in the internal lamellar regions of P3HT NWs through lateral diffusion or on the top surface of the NWs. The accurate determation of the dopant position with respect to the well-dispersed P3HT NWs is beyond the spatial resolving capability of our instrumentation.

Figure 3.4(c) highlights the CPD of undoped P3HT NWs. The imaging contrast presents a distinguishable separation of CPD values of NWs and the ITO background, resulting in a bimodal distribution in the CPD histogram as shown in Figure 3.7(a). However, the CPD peak of P3HT NWs is 10 mV higher than the peak of the ITO reference (Figure 3.7(a)), indicating a slightly higher work function of the undoped P3HT NWs on ITO. Upon moderate doping (i.e. 250 μg/mL), CPD imaging of the doped P3HT NWs becomes featureless (Figure 3.4(f)). The CPD peak of P3HT NWs shifts to lower values and becomes indistinguishable to the ITO substrate (Figure 3.7(b)). When the P3HT NWs are excessively doped (i.e. 1 mg/mL), the CPD of P3HT NWs remains featureless while the excessive neutral dopant shows significantly reduced CPD readings (Figure 3.4(i)). These lower CPD values result in an extended tail in the CPD histogram in the excessively doped case (Figure 3.7(c)). CPD profiles of marked cross-sections in Figure 3.4(i) confirm the lower CPD values ranging from −20 mV to around −100 mV (Figure 3.6). This observation is qualitatively consistent with our previous report on the doping of ultrathin P3HT films,[61] in which KPFM imaging shows lower CPD values of −50 mV throughout

the doped film in the presence of an excessive amount of dopant, while the CPD value of the film approaches that of the ITO reference when excessive dopant is removed by acetonitrile.

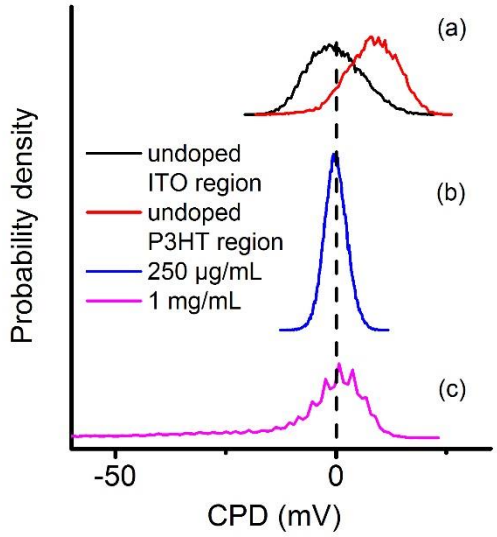

Figure 3.7 *CPD histograms of undoped and doped P3HT.*

Note: (a) undoped P3HT NWs, (b) NWs sequentially doped with 250 µg/mL F4TCNQ and (c) P3HT NWs sequentially doped with 1 mg/mL F4TCNQ, which corresponding to the CPD image as shown in Figure 3.4(c), 2(f), and 2(i), respectively. The average CPD value of ITO is deliberately shifted to zero in all scenarios as an internal reference.

3.3.4 Conductivity of well-dispersed P3HT thin-film nanowire networks

P3HT NWs can be deposited on quartz substrates for the measurements of conductivity by the same spin-coating method used in the preparation of AFM samples. In the inset of Figure 3.8, a similar morphology of P3HT NWs with a surface coverage of ~30% can be achieved. A summary on the statistics on the morphological parameters of undoped and doped P3HT NWs on quartz substrates can be found in Table 3.3. The average thickness of P3HT NWs on quartz substrates is 3.3 nm, close to that on ITO substrates.

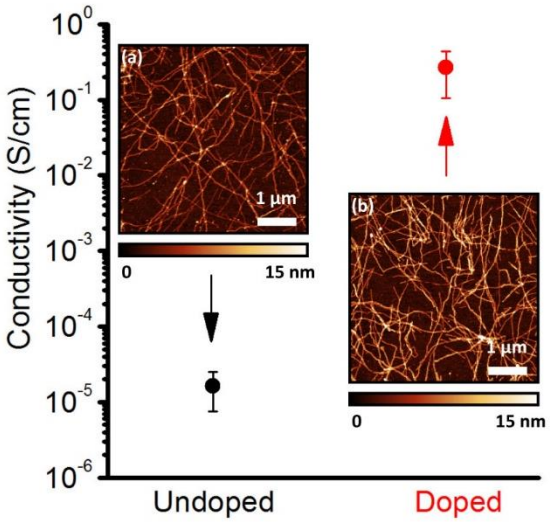

Figure 3.8 *Conductivity of undoped and moderately doped P3HT NW network on a quartz substrate with pre-fabricated interdigitated Au electrodes.*

Note: Inset (a) represents a 5 × 5 μm scan of undoped P3HT network while inset (b) reveals the morphology of the doped network. Note that the moderately doped P3HT network can be prepared by spin-coating a 250 μg/mL F4TCNQ onto a pristine pre-formed P3HT NW film at 3000 rpm.

Upon doping by 250 μg/mL F4TCNQ, the thickness increases by 2 nm, larger than the ~1 nm increment on ITO. While this difference might originate from differences in the substrate, it is within the 2 nm RMS of both undoped and doped P3HT.

Table 3.3 *Statistical quantities on undoped and doped P3HT NW networks on quartz wafers.*

Statistics	NW		
	Average height (nm)	RMS (nm)	Surface coverage (%)
undoped	3.3	1.8	30
250 μg/mL	5.2	2.3	33

The *I-V* curves of both undoped and doped samples are shown in Figure 3.9. The average conductivity of moderately doped P3HT is about 0.27 S/cm, which is significantly

higher than 1.64×10^{-5} S/cm of undoped P3HT. Depending on molecular weight, regioregularity, solvent or preparation methods, the electrical conductivity of pristine P3HT films is around 10^{-6} to 10^{-4} S/cm.[8, 53, 58, 59, 61, 62]

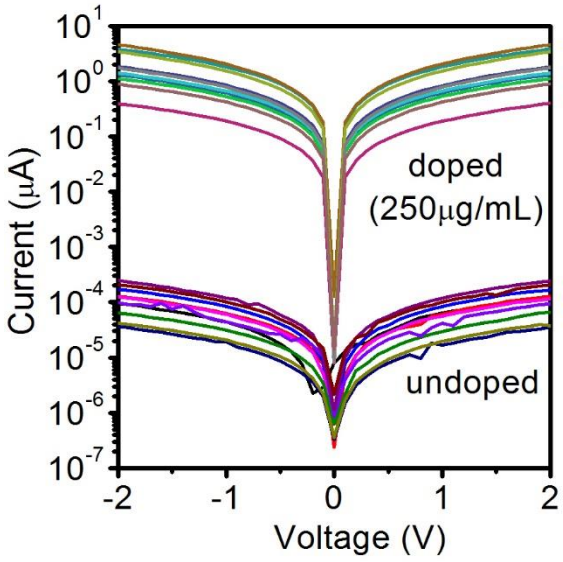

Figure 3.9 *I-V curves of undoped and moderately doped (250 μg/mL) F_4TCNQ P3HT NW network on a quartz substrate with pre-fabricated interdigitated Au electrodes.*

Note: on average, the doped samples show a four orders of magnitude increase in current under the same bias.

The conductivity of the pristine P3HT NW networks is within the range of values reported in the literature. For doped P3HT, the conductivity of films prepared from mixed solution doping ranges from 0.1 S/cm to 1 S/cm,[59, 62-64] and that of sequentially doped P3HT films is shown to be 1−10 S/cm.[6, 8, 53] The conductivity of moderately doped P3HT NW networks is lower compared to a typical sequentially doped film.[61] It has been suggested that the infiltration of F4TCNQ into the amorphous region of P3HT film facilitates the segregation of dopant anions and charge transport pathways of P3HT polarons, which may account for the higher conductivity of sequentially doped P3HT film compared to mixed solution doping, particularly at lower doping levels.[8] Owing to

insignificant presence of amorphous P3HT regions in the NW networks, infiltration of F4TCNQ into highly ordered P3HT NW networks might be limited. In addition, because most of the nanowires are only a few nanometers thick, the diffusion of dopant in the doping of P3HT nanowires will play a much smaller role than in the doping for bulk films, where dopant molecules need to diffuse through thicknesses up to hundreds of nanometers or higher with substantial amount of amorphous domains. As previously mentioned, the most probable location of the dopant may be restricted to the lamellar region in the side chain direction or the top layer. This might hamper the overall doping level of P3HT NWs, which is consistent with the relatively lower conductivity as compared to the values obtained from typical sequential doping of a P3HT thin film.

3.4 Conclusion

A well-dispersed P3HT NW network was successfully prepared using an ultra-low concentration of P3HT on a variety of substrates with approximately 33% coverage. The average thickness of is approximately 3.3 nm, indicating that the majority of P3HT NWs are double- or triple-layer. The overall thickness of NW feature upon moderate doping (i.e. 250 μg/mL F4TCNQ) increases by 1−2 nm. A high concentration of dopant results in dot-like features on the surface of the film, which can be associated with excessive neutral dopant dried out after the sequential doping process. These dot-like features have a broad distribution of CPD values well below the value of ITO, which is significantly different from the CPD of undoped NWs (~10 mV) and moderately doped NWs (~0 mV). The in-plane conductivities of undoped (1.64×10^{-5} S/cm) and doped P3HT NW networks (0.27 S/cm) demonstrate four orders of magnitude increase upon moderate doping of the highly

ordered P3HT NW network. This proved that effective doping is still possible without significant presence of amorphous domains that typically exist in P3HT thin films. However, this result is still lagging behind conducting nanofibers based on small molecules that shows metallic charge transport behavior with a conductivity significantly above 10 S/cm.[65, 66] The possible locations of the dopant molecules include the lamellar region of the side chains or on the top layer. These results strengthen the understanding of doping of P3HT NW networks and shed light on improved design guidelines toward nanowire based conjugated polymer devices.

Reference

1. Lüssem, B.; Keum, C.-M.; Kasemann, D.; Naab, B.; Bao, Z.; Leo, K., Doped organic transistors. *Chem. Rev.* **2016,** *116* (22), 13714-13751.
2. Xu, Y.; Sun, H.; Liu, A.; Zhu, H.-H.; Li, W.; Lin, Y.-F.; Noh, Y.-Y., Doping: A Key Enabler for Organic Transistors. *Adv. Mater.* **2018,** *30* (46), 1801830.
3. Yoo, S. J.; Kim, J. J., Charge transport in electrically doped amorphous organic semiconductors. *Macromol. Rapid Commun.* **2015,** *36* (11), 984-1000.
4. Reineke, S.; Lindner, F.; Schwartz, G.; Seidler, N.; Walzer, K.; Lüssem, B.; Leo, K., White organic light-emitting diodes with fluorescent tube efficiency. *Nature* **2009,** *459* (7244), 234.
5. Kao, C. Y.; Lee, B.; Wielunski, L. S.; Heeney, M.; McCulloch, I.; Garfunkel, E.; Feldman, L. C.; Podzorov, V., Doping of conjugated polythiophenes with alkyl silanes. *Adv. Funct. Mater.* **2009,** *19* (12), 1906-1911.
6. Scholes, D. T.; Hawks, S. A.; Yee, P. Y.; Wu, H.; Lindemuth, J. R.; Tolbert, S. H.; Schwartz, B. J., Overcoming Film Quality Issues for Conjugated Polymers Doped with F4TCNQ by Solution Sequential Processing: Hall Effect, Structural, and Optical Measurements. *J. Phys. Chem. Lett.* **2015,** *6* (23), 4786-4793.
7. Scholes, D. T.; Yee, P. Y.; Lindemuth, J. R.; Kang, H.; Onorato, J.; Ghosh, R.; Luscombe, C. K.; Spano, F. C.; Tolbert, S. H.; Schwartz, B. J., The Effects of Crystallinity on Charge Transport and the Structure of Sequentially Processed F4TCNQ-Doped Conjugated Polymer Films. *Adv. Funct. Mater.* **2017,** *27* (44), 1702654.
8. Jacobs, I. E.; Aasen, E. W.; Oliveira, J. L.; Fonseca, T. N.; Roehling, J. D.; Li, J.; Zhang, G.; Augustine, M. P.; Mascal, M.; Moulé, A. J., Comparison of solution-mixed and sequentially processed P3HT:F4TCNQ films: effect of doping-induced aggregation on film morphology. *J. Mater. Chem. C* **2016,** *4* (16), 3454-3466.
9. Hourani, W.; Rahimi, K.; Botiz, I.; Koch, F. P. V.; Reiter, G.; Lienerth, P.; Heiser, T.; Bubendorff, J.-L.; Simon, L., Anisotropic charge transport in large single crystals of π-conjugated organic molecules. *Nanoscale* **2014,** *6* (9), 4774-4780.
10. Rahimi, K.; Botiz, I.; Agumba, J. O.; Motamen, S.; Stingelin, N.; Reiter, G., Light absorption of poly (3-hexylthiophene) single crystals. *RSC Adv.* **2014,** *4* (22), 11121-11123.
11. Rahimi, K.; Botiz, I.; Stingelin, N.; Kayunkid, N.; Sommer, M.; Koch, F. P. V.; Nguyen, H.; Coulembier, O.; Dubois, P.; Brinkmann, M., Controllable processes for generating large single crystals of poly (3-hexylthiophene). *Angew. Chem., Int. Ed.* **2012,** *51* (44), 11131-11135.
12. Lobov, G. S.; Zhao, Y.; Marinins, A.; Yan, M.; Li, J.; Sugunan, A.; Thylén, L.; Wosinski, L.; Östling, M.; Toprak, M. S.; Popov, S., Size Impact of Ordered P3HT Nanofibers on Optical Anisotropy. *Macromol. Chem. Phys.* **2016,** *217* (9), 1089-1095.
13. Lobov, G. S.; Zhao, Y.; Marinins, A.; Yan, M.; Li, J.; Toprak, M. S.; Sugunan, A.; Thylen, L.; Wosinski, L.; Östling, M.; Popov, S., Electric field induced optical anisotropy of P3HT nanofibers in a liquid solution. *Opt. Mater. Express* **2015,** *5* (11), 2642-2647.

14. McFarland, F. M.; Liu, X.; Zhang, S.; Tang, K.; Kreis, N. K.; Gu, X.; Guo, S., Electric field induced assembly of macroscopic fibers of poly (3-hexylthiophene). *Polymer* **2018,** *151*, 56-64.
15. Xi, Y.; Pozzo, L. D., Electric field directed formation of aligned conjugated polymer fibers. *Soft Matter* **2017,** *13* (21), 3894-3908.
16. Ye, Z.; Yang, X.; Cui, H.; Qiu, F., Nanowires with unusual packing of poly(3-hexylthiophene)s induced by electric fields. *J. Mater. Chem. C* **2014,** *2* (33), 6773-6780.
17. Chen, J.-Y.; Kuo, C.-C.; Lai, C.-S.; Chen, W.-C.; Chen, H.-L., Manipulation on the morphology and electrical properties of aligned electrospun nanofibers of poly (3-hexylthiophene) for field-effect transistor applications. *Macromolecules* **2011,** *44* (8), 2883-2892.
18. Chen, J.-Y.; Wu, H.-C.; Chiu, Y.-C.; Lin, C.-J.; Tung, S.-H.; Chen, W.-C., Electrospun Poly(3-hexylthiophene) Nanofibers with Highly Extended and Oriented Chains Through Secondary Electric Field for High-Performance Field-Effect Transistors. *Adv. Electron. Mater.* **2015,** *1* (1-2), 1400028.
19. González, R.; Pinto, N. J., Electrospun poly(3-hexylthiophene-2,5-diyl) fiber field effect transistor. *Synth. Met.* **2005,** *151* (3), 275-278.
20. Lee, S.; Moon, G. D.; Jeong, U., Continuous production of uniform poly(3-hexylthiophene) (P3HT) nanofibers by electrospinning and their electrical properties. *J. Mater. Chem.* **2009,** *19* (6), 743-748.
21. Lee, S. W.; Lee, H. J.; Choi, J. H.; Koh, W. G.; Myoung, J. M.; Hur, J. H.; Park, J. J.; Cho, J. H.; Jeong, U., Periodic Array of Polyelectrolyte-Gated Organic Transistors from Electrospun Poly(3-hexylthiophene) Nanofibers. *Nano Lett.* **2010,** *10* (1), 347-351.
22. Liu, H.; Reccius, C. H.; Craighead, H. G., Single electrospun regioregular poly(3-hexylthiophene) nanofiber field-effect transistor. *Appl. Phys. Lett.* **2005,** *87* (25), 253106.
23. Samitsu, S.; Shimomura, T.; Ito, K., Nanofiber preparation by whisker method using solvent-soluble conducting polymers. *Thin Solid Films* **2008,** *516* (9), 2478-2486.
24. Sarker, B. K.; Liu, J.; Zhai, L.; Khondaker, S. I., Fabrication of Organic Field Effect Transistor by Directly Grown Poly(3 Hexylthiophene) Crystalline Nanowires on Carbon Nanotube Aligned Array Electrode. *ACS Appl. Mater. Interfaces* **2011,** *3* (4), 1180-1185.
25. McFarland, F. M.; Brickson, B.; Guo, S., Layered poly (3-hexylthiophene) nanowhiskers studied by atomic force microscopy and kelvin probe force microscopy. *Macromolecules* **2015,** *48* (9), 3049-3056.
26. Han, Y.; Guo, Y.; Chang, Y.; Geng, Y.; Su, Z., Chain Folding in Poly(3-hexylthiophene) Crystals. *Macromolecules* **2014,** *47* (11), 3708-3712.
27. Guo, Y.; Ma, X.; Su, Z., Interfacial interactions between poly (3-hexylthiophene) and substrates. *Macromolecules* **2013,** *46* (7), 2733-2739.
28. Guo, Y.; Jiang, L.; Ma, X.; Hu, W.; Su, Z., Poly (3-hexylthiophene) monolayer nanowhiskers. *Polym. Chem.* **2013,** *4* (16), 4308-4311.
29. Liu, J.; Zou, J.; Zhai, L., Bottom-up Assembly of Poly(3-hexylthiophene) on Carbon Nanotubes: 2D Building Blocks for Nanoscale Circuits. *Macromol. Rapid Commun.* **2009,** *30* (16), 1387-1391.

30. Liu, J.; Arif, M.; Zou, J.; Khondaker, S. I.; Zhai, L., Controlling Poly(3-hexylthiophene) Crystal Dimension: Nanowhiskers and Nanoribbons. *Macromolecules* **2009,** *42* (24), 9390-9393.
31. Arif, M.; Liu, J.; Zhai, L.; Khondaker, S. I., Poly(3-hexylthiophene) crystalline nanoribbon network for organic field effect transistors. *Appl. Phys. Lett.* **2010,** *96* (24), 243304.
32. Ma, X.; Guo, Y.; Wang, T.; Su, Z., Scanning tunneling microscopy investigation of self-assembled poly (3-hexylthiophene) monolayer. *J. Chem. Phys.* **2013,** *139* (1), 014701.
33. Merlo, J. A.; Frisbie, C. D., Field effect transport and trapping in regioregular polythiophene nanofibers. *J. Phys. Chem. B* **2004,** *108* (50), 19169-19179.
34. Merlo, J. A.; Frisbie, C. D., Field effect conductance of conducting polymer nanofibers. *J. Polym. Sci., Part B: Polym. Phys.* **2003,** *41* (21), 2674-2680.
35. Dierckx, W.; Oosterbaan, W. D.; Bolsée, J.-C.; Cardinaletti, I.; Maes, W.; Boyen, H.-G.; D'Haen, J.; Nesladek, M.; Manca, J., Organic phototransistors using poly (3-hexylthiophene) nanofibres. *Nanotechnology* **2015,** *26* (6), 065201.
36. Bolsée, J.-C.; Oosterbaan, W. D.; Lutsen, L.; Vanderzande, D.; Manca, J., CAFM on conjugated polymer nanofibers: Capable of assessing one fiber mobility. *Org. Electron.* **2011,** *12* (12), 2084-2089.
37. Bolsée, J. C.; Oosterbaan, W. D.; Lutsen, L.; Vanderzande, D.; Manca, J., The importance of bridging points for charge transport in webs of conjugated polymer nanofibers. *Adv. Funct. Mater.* **2013,** *23* (7), 862-869.
38. Samitsu, S.; Shimomura, T.; Heike, S.; Hashizume, T.; Ito, K., Field-effect carrier transport in poly (3-alkylthiophene) nanofiber networks and isolated nanofibers. *Macromolecules* **2010,** *43* (19), 7891-7894.
39. Samitsu, S.; Shimomura, T.; Heike, S.; Hashizume, T.; Ito, K., Effective production of poly (3-alkylthiophene) nanofibers by means of whisker method using anisole solvent: structural, optical, and electrical properties. *Macromolecules* **2008,** *41* (21), 8000-8010.
40. Zhou, X.; Pfeiffer, M.; Blochwitz, J.; Werner, A.; Nollau, A.; Fritz, T.; Leo, K., Very-low-operating-voltage organic light-emitting diodes using a p-doped amorphous hole injection layer. *Appl. Phys. Lett.* **2001,** *78* (4), 410-412.
41. Pfeiffer, M.; Beyer, A.; Fritz, T.; Leo, K., Controlled doping of phthalocyanine layers by cosublimation with acceptor molecules: A systematic Seebeck and conductivity study. *Appl. Phys. Lett.* **1998,** *73* (22), 3202-3204.
42. Kivala, M.; Boudon, C.; Gisselbrecht, J.-P.; Enko, B.; Seiler, P.; Müller, I. B.; Langer, N.; Jarowski, P. D.; Gescheidt, G.; Diederich, F., Organic Super-Acceptors with Efficient Intramolecular Charge-Transfer Interactions by [2+2] Cycloadditions of TCNE, TCNQ, and F4-TCNQ to Donor-Substituted Cyanoalkynes. *Chem. - Eur. J.* **2009,** *15* (16), 4111-4123.
43. Gao, Z. Q.; Mi, B. X.; Xu, G. Z.; Wan, Y. Q.; Gong, M. L.; Cheah, K. W.; Chen, C. H., An organic p-type dopant with high thermal stability for an organic semiconductor. *Chem. Commun.* **2008,** (1), 117-119.

44. Gao, W.; Kahn, A., Controlled p-doping of zinc phthalocyanine by coevaporation with tetrafluorotetracyanoquinodimethane: A direct and inverse photoemission study. *Appl. Phys. Lett.* **2001,** *79* (24), 4040-4042.
45. Wang, C.; Duong, D. T.; Vandewal, K.; Rivnay, J.; Salleo, A., Optical measurement of doping efficiency in poly(3-hexylthiophene) solutions and thin films. *Phys. Rev. B* **2015,** *91* (8), 085205.
46. Müller, L.; Nanova, D.; Glaser, T.; Beck, S.; Pucci, A.; Kast, A. K.; Schröder, R. R.; Mankel, E.; Pingel, P.; Neher, D., Charge-transfer–solvent interaction predefines doping efficiency in p-doped P3HT films. *Chem. Mater.* **2016,** *28* (12), 4432-4439.
47. Clark, J.; Silva, C.; Friend, R. H.; Spano, F. C., Role of Intermolecular Coupling in the Photophysics of Disordered Organic Semiconductors: Aggregate Emission in Regioregular Polythiophene. *Phys. Rev. Lett.* **2007,** *98* (20), 206406.
48. Spano, F. C.; Silva, C., H- and J-Aggregate Behavior in Polymeric Semiconductors. *Annu. Rev. Phys. Chem.* **2014,** *65* (1), 477-500.
49. Spano, F. C., The Spectral Signatures of Frenkel Polarons in H- and J-Aggregates. *Acc. Chem. Res.* **2010,** *43* (3), 429-439.
50. Spano, F. C., Modeling disorder in polymer aggregates: The optical spectroscopy of regioregular poly(3-hexylthiophene) thin films. *J. Chem. Phys.* **2005,** *122* (23), 234701.
51. Louarn, G.; Trznadel, M.; Buisson, J. P.; Laska, J.; Pron, A.; Lapkowski, M.; Lefrant, S., Raman Spectroscopic Studies of Regioregular Poly(3-alkylthiophenes). *J. Phys. Chem.* **1996,** *100* (30), 12532-12539.
52. Botta, C.; Luzzati, S.; Tubino, R.; Borghesi, A., Optical excitations of poly-3-alkylthiophene films and solutions. *Phys. Rev. B* **1992,** *46* (20), 13008-13016.
53. Hynynen, J.; Kiefer, D.; Yu, L.; Kroon, R.; Munir, R.; Amassian, A.; Kemerink, M.; Müller, C., Enhanced Electrical Conductivity of Molecularly p-Doped Poly(3-hexylthiophene) through Understanding the Correlation with Solid-State Order. *Macromolecules* **2017,** *50* (20), 8140-8148.
54. Clark, J.; Chang, J.-F.; Spano, F. C.; Friend, R. H.; Silva, C., Determining exciton bandwidth and film microstructure in polythiophene films using linear absorption spectroscopy. *Appl. Phys. Lett.* **2009,** *94* (16), 163306.
55. McFarland, F. M.; Bonnette, L. R.; Acres, E. A.; Guo, S., The impact of aggregation on the p-doping kinetics of poly(3-hexylthiophene). *J. Mater. Chem. C* **2017,** *5* (23), 5764-5771.
56. Turner, S. T.; Pingel, P.; Steyrleuthner, R.; Crossland, E. J. W.; Ludwigs, S.; Neher, D., Quantitative Analysis of Bulk Heterojunction Films Using Linear Absorption Spectroscopy and Solar Cell Performance. *Adv. Funct. Mater.* **2011,** *21* (24), 4640-4652.
57. Oh, J. Y.; Shin, M.; Lee, T. I.; Jang, W. S.; Min, Y.; Myoung, J.-M.; Baik, H. K.; Jeong, U., Self-Seeded Growth of Poly(3-hexylthiophene) (P3HT) Nanofibrils by a Cycle of Cooling and Heating in Solutions. *Macromolecules* **2012,** *45* (18), 7504-7513.
58. Pingel, P.; Neher, D., Comprehensive picture of p-type doping of P3HT with the molecular acceptor F4TCNQ. *Phys. Rev. B* **2013,** *87* (11), 115209.
59. Duong, D. T.; Wang, C.; Antono, E.; Toney, M. F.; Salleo, A., The chemical and structural origin of efficient p-type doping in P3HT. *Org. Electron.* **2013,** *14* (5), 1330-1336.

60. Méndez, H.; Heimel, G.; Winkler, S.; Frisch, J.; Opitz, A.; Sauer, K.; Wegner, B.; Oehzelt, M.; Röthel, C.; Duhm, S.; Többens, D.; Koch, N.; Salzmann, I., Charge-transfer crystallites as molecular electrical dopants. *Nat. Commun.* **2015,** *6*, 8560.
61. Tang, K.; McFarland, F. M.; Travis, S.; Lim, J.; Azoulay, J. D.; Guo, S., Aggregation of P3HT as a preferred pathway for its chemical doping with F4-TCNQ. *Chem. Commun.* **2018,** *54* (84), 11925-11928.
62. Yim, K.-H.; Whiting, G. L.; Murphy, C. E.; Halls, J. J. M.; Burroughes, J. H.; Friend, R. H.; Kim, J.-S., Controlling Electrical Properties of Conjugated Polymers via a Solution-Based p-Type Doping. *Adv. Mater.* **2008,** *20* (17), 3319-3324.
63. Kiefer, D.; Yu, L.; Fransson, E.; Gómez, A.; Primetzhofer, D.; Amassian, A.; Campoy-Quiles, M.; Müller, C., A Solution-Doped Polymer Semiconductor:Insulator Blend for Thermoelectrics. *Adv. Sci.* **2017,** *4* (1), 1600203.
64. Glaudell, A. M.; Cochran, J. E.; Patel, S. N.; Chabinyc, M. L., Impact of the Doping Method on Conductivity and Thermopower in Semiconducting Polythiophenes. *Adv. Energy. Mater.* **2015,** *5* (4), 1401072.
65. Faramarzi, V.; Niess, F.; Moulin, E.; Maaloum, M.; Dayen, J.-F.; Beaufrand, J.-B.; Zanettini, S.; Doudin, B.; Giuseppone, N., Light-triggered self-construction of supramolecular organic nanowires as metallic interconnects. *Nature Chemistry* **2012,** *4*, 485.
66. Zhen, Y.; Inoue, K.; Wang, Z.; Kusamoto, T.; Nakabayashi, K.; Ohkoshi, S.-i.; Hu, W.; Guo, Y.; Harano, K.; Nakamura, E., Acid-Responsive Conductive Nanofiber of Tetrabenzoporphyrin Made by Solution Processing. *J. Am. Chem. Soc.* **2018,** *140* (1), 62-65.

CHAPTER IV – Crosslinked PEDOT:PSS Organic Electrochemical Transistors on Interdigitated Electrodes with Improved Stability

(This chapter is adapted with permission from *ACS Appl. Polym. Mater.*, 2021, 3, 1436–1444).

In this chapter, the influence of gate voltage in the off state ($V_{g, off}$) on the stability of the transfer curve of an organic electrochemical transistor (OECT) based on interdigitated electrodes (IDEs) is studied in this work. When a high $V_{g, off}$ such as +0.5 V is used, a larger amount of Na^+ ion injection is promoted as compared to lower $V_{g, off}$, and a noticeable decay of drain current is observed in the transfer characteristics of the OECTs upon consecutive measurements. After the crosslinking of PEDOT:PSS, the decay of drain current can be significantly reduced, indicating the improved stability of transfer characteristic in the crosslinked OECTs. The mitigation effect after crosslinking of PEDOT:PSS on the decay of drain current is also observed in the pulsed gate bias stress experiment, which allows the usage of a higher pulse gate voltage in the off state. The decay of drain current is likely attributed to the repetitive injection-extraction of cations (i.e. Na^+) under cycling gate bias.

4.1 Introduction

Organic electrochemical transistors (OECTs) based on intrinsically doped conjugated polymers (CPs) such as PEDOT:PSS have been developed recently as a promising candidate for biosensing and bioelectronics.[1-5] By controlling the ion injection into the CP film via gate voltage, it can be partially de-doped or re-doped, resulting in the

modulation of drain current. In contrast to a conventional semiconductor transistor, OECT is compatible with water and operates under the sub 1 V regime, which makes it naturally suitable for low-voltage biosensing applications in aqueous environments. Therefore, OECTs open a new avenue for the sensing of various analytes in aqueous solutions such as glucose,[6-9] metabolites,[10-12] neurotransmitters,[13, 14] and proteins.[15-18] Furthermore, many successful attempts have been made to adopt OECT devices in the detection and tracing of neural signals in the brain, showing great promises in the *in vivo* electrophysiological recordings.[19, 20]

To make a film suitable for OECT biosensing applications, it must (1) be physically stable in an aqueous environment without degradation, decomposition, or delamination, and (2) be physically and electrically stable under the stress of repetitive ion injection-extraction. The preparation of PEDOT:PSS film is rather facile, which can be done by simply spin-coating a PEDOT:PSS solution onto a substrate. To fulfill the demand of flexible electronics, PEDOT:PSS can also be deposited on a soft substrate such as PDMS by spray-coating method.[21, 22] After the deposition of PEDOT:PSS, an annealing step at an elevated temperature (i.e., 140 ^{o}C) is needed to increase the as-deposited film's water stability, meeting the first requirement listed above.[23-26] In biosensing measurements, a stable drain current is typically required to establish a reliable baseline or a calibration curve. This requirement for device stability can be more challenging under repeated electrical measurements, due to possible degradation or decomposition of organic semiconducting materials resulting from bias-induced stresses. To further increase the stability of the PEDOT:PSS OECT device against dissolution and delamination in an

aqueous environment, organosilane compounds, such as (3-glycidyloxypropyl)trimethoxysilane (GOPS), can be introduced to crosslink the PEDOT:PSS layer.[20, 27-30] Recently, the implementation of more novel crosslinkers such as divinyl sulfone (DVS) have been reported to obtain water-stable PEDOT:PSS films at a lower annealing temperature without sacrificing their conductivity and mechanical flexibility.[30, 31]

Despite the extensive use of crosslinked PEDOT:PSS as OECT devices, there is still a lack of fundamental understanding of how crosslinking of PEDOT:PSS films could improve their electrical stability. Furthermore, the conventional fabrication method of PEDOT:PSS OECTs generally involves rather complicated lithography work.[20, 25, 32] Using a prefabricated substrate with interdigitated electrodes (IDEs), Zeglio et al devised a lithography free method for the fabrication of OECTs based on a blend of two anionic conjugated polyelectrolytes, which is capable of switching between depletion and accumulation modes.[33] Meanwhile, Flagg et al. prepared IDE based OECTs in accumulation mode using p-type CPs like P3HT as active layer for more accessible biochemical applications.[34, 35] There seems to be a lack of examples on IDE based depletion mode OECTs. In this work, we will try to establish the relationship between the decay of transfer characteristics of IDEs based PEDOT:PSS OECTs with gate voltage stress and crosslinking, since transfer characteristics of OECTs, as a direct indication of drain current at “off” and “on” states, is extensively used in a variety of biosensing applications.[9, 16, 36] Meanwhile, the research on OECTs gated with a presynaptic mimicking pulse as an artificial synapse has recently been developed,[37-40] which shows great promise in the

control or sensing of neurophysiological processes.[2, 4, 41] Given the importance of application of OECTs based on the pulse technique, the scope of our work will be extended to examine the on/off cycling stability of both pristine and crosslinked OECT devices as well. The knowledge gained for the crosslinking induced stabilization in this work will help the design and utilization of better water-compatible OECT devices in the future.

4.2 Materials and Methods

4.2.1 Materials

PEDOT:PSS aqueous dispersion (1.3 wt%) and (3-glycidyloxypropyl)trimethoxysilane (GOPS) were purchased from Sigma-Aldrich. Electrolytes such as disodium phosphate (Na_2HPO_4), monosodium phosphate (NaH_2PO_4), and sodium chloride (NaCl) were also purchased from Sigma-Aldrich. The concentrations of NaH_2PO_4 and Na_2HPO_4 were 1.8 mM and 10 mM, respectively, resulting in a pH of 7.4 phosphate buffer solution (PBS). The concentration of NaCl for OECT experiments was 0.1 M. Note that the only alkali cation presented in this PBS buffer is Na^+. DI water was used for the preparation of PBS buffer. Organic solvents in reagent grade were purchased from Fisher Scientific. Ag wire (dia. 0.5 mm) was purchased from Alfa Aesar. Commercially available prefabricated interdigitated electrodes (IDEs) were obtained from NanoSPR, LLC, IL, USA. The dimensions of the electrodes: channel length L = 20 μm, total channel width W = 20 mm (1 mm each × 20 pairs). Glass substrates coated with fluorine-tin-oxide (FTO) were purchased from MTI Corporation, USA.

4.2.2 OECT Device Fabrication and Characterization

A mixture of 1:1 (v/v) of PEDOT:PSS aqueous dispersion and isopropanol was prepared to increase the wettability of PEDOT:PSS film on the substrate.[42-44] For crosslinked PEDOT:PSS, 2 v% of (3-glycidyloxypropyl)trimethoxysilane (GOPS) was added into the mixture solution before spin-coating. Prior to spin-coating, prefabricated substrates were sonicated in acetone for 15 min. After blown dry under a flow of nitrogen, prefabricated substrates were treated with UV ozone for 10 minutes in a UV ozone cleaner (Ossila, Ltd., UK). Then, the PEDOT:PSS mixture solution was spun on a prefabricated substrate at 3000 rpm. In general, the fabrication method of OECTs on interdigitated electrodes followed the reported procedures.[34, 35] Excess PEDOT:PSS was removed by Q-tips soaked with DI water, after which only PEDOT:PSS on the interdigitated electrode region remained. Then the substrate was placed on a hotplate and subsequently annealed at 140 ^{o}C for 1 h. After annealing, the PEDOT:PSS-free region was insulated from potential contact with electrolyte solution by applying an insulating layer (Sally Hansen, Insta-Dri).

OECT devices were measured in a PBS buffer (pH = 7.4) containing 0.1 M NaCl. The PBS buffer was bubbled with N_2 for 15 min prior to any measurement and a N_2 flow was maintained on top of the solution during OECT measurements. The PEDOT:PSS covered IDEs region was immersed in water during all OECT measurements. An Ag wire was used as the gate electrode for OECTs. The OECT characterizations were carried out with a dual-channel Keithley 2612B source measure unit that was controlled by Keithley ACS software. When no gate bias was applied, *I-V* characteristics of the films can be

measured. For the pulsed gate bias technique, the output of pulse trains and the recording of current response were performed in Keithley TSB builder.

4.2.3 Atomic Force Microscopy (AFM)

AFM topography measurements were performed using semi-contact mode on an NTEGRA Prima AFM from NT-MDT Spectrum Instruments. Tips (NSC18-Pt) from μMasch with a typical resonant frequency of 75 kHz and a spring force constant of 1.2−5.5 N/m were equipped. To measure the thickness of the PEDOT:PSS film, a slit on the film was exposed by scratching the film with a tweezer.

4.3 Results and Discussion

4.3.1 Morphology and *I-V* Characteristics

The film morphology of pristine PEDOT:PSS shows a surface roughness (RMS) of about 12 nm (Figure 4.1a). The roughness of GOPS-crosslinked PEDOT:PSS increases to 20 nm (Figure 4.1b). The thickness of both films is close to 60 nm as shown in Figure 4.1c and d. The enhanced height variations can be observed in the height profile of the crosslinked film shown in Figure 4.1d. The mechanism of the crosslinking reaction between PEDOT:PSS, GOPS, and the glass substrate is still under debate. PEDOT:PSS might be linked with GOPS by a reaction between the sulfonic acid group of the PSS and the epoxy group of GOPS at elevated temperature (i.e. 140 ^{o}C).[29, 30, 45] Meanwhile, in the presence of moisture, the methoxysilane groups can undergo self-condensation or condensation with the hydroxyl group on the glass substrate to form interconnecting siloxane bonds.[29, 45] These two reactions likely take place simultaneously, leading to the incorporation of PEDOT:PSS into a siloxane network.

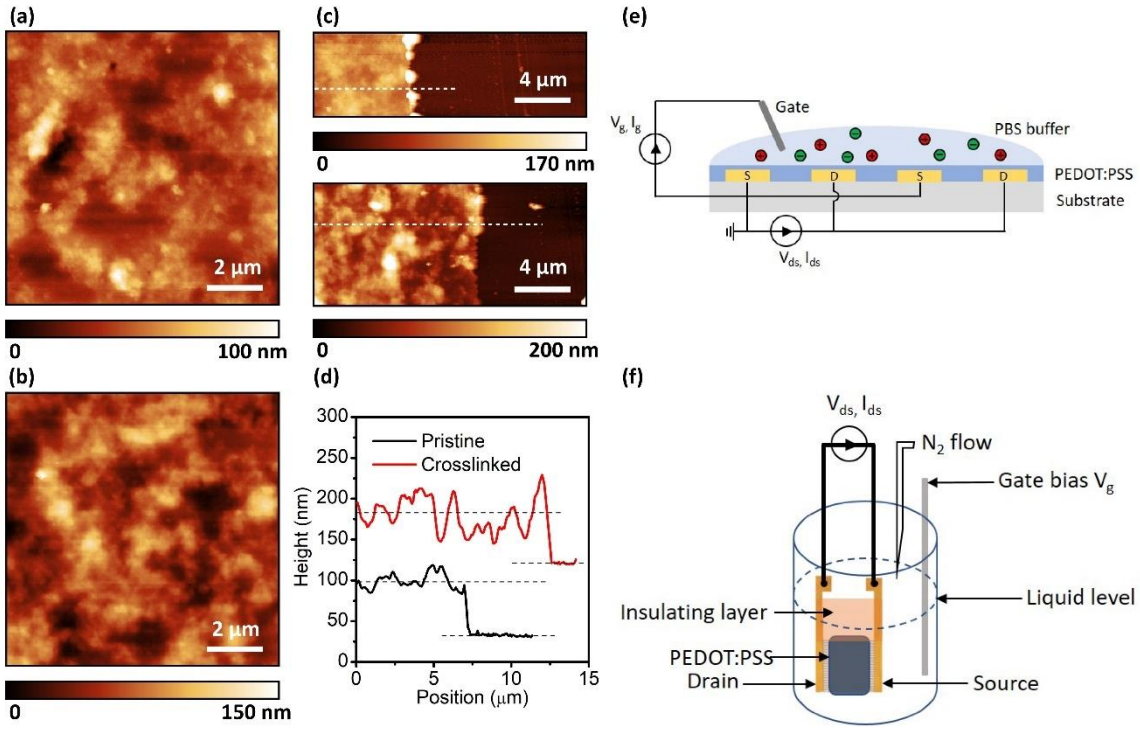

Figure 4.1 *Morphology of pristine (a) and crosslinked (b) PEDOT:PSS film before immersion in PBS buffer for OECT measurements.*

Note: The film thickness of pristine, top figure in panel (c), is determined as 65 ± 12 nm. The crosslinked film, as shown in the bottom of panel (c), has a thickness of 60 ± 20 nm. The height profiles of marked cross sections in Panel (c) are presented in panel (d). Panel (e) shows the schematic representation of a PEDOT:PSS OECT device using interdigitated electrodes. Only two pairs of electrode fingers are shown. The real electrode has 20 pairs. Panel (f) is the configuration of OECT based on a prefabricated substrate with interdigitated electrodes. A N_2 flow is maintained on top of the liquid to prevent parasitic reactions with oxygen.

It is frequently observed that the in-plane conductivity of crosslinked PEDOT:PSS is inferior to pristine PEDOT:PSS without crosslinking.[29, 45, 46] Similar results can be seen in Figure 4.2 as the conductivity of crosslinked PEDOT:PSS is lower than that of the pristine ones. This is possibly due to a reduced hole concentration and/or carrier mobility. So far, the dominating factor for the reduced conductivity of crosslinked PEDOT:PSS has not been fully elucidated. Through direct measurement of transient drift current dominated by holes at t = 0 s, Stavrinidou *et al*. concluded that the hole mobility is unchanged before

and after GOPS crosslinking.[46] On the other hand, Fabiano *et al*. suggested the hole density in GOPS-treated PEDOT:PSS is unaffected via UV-vis polaron analysis.[45] Despite the discrepancy in the explanation on the reduced conductivity of crosslinked PEDOT:PSS films, their *I-V* characteristics in PBS buffer remain unchanged upon consecutive runs, showing good water stability of both pristine and crosslinked PEDOT:PSS. As shown in Figure 4.2a and b, consecutive *I-V* curves measured every 10 s overlap each other without noticeable differences for both pristine and crosslinked devices. The *I-V* curves measured every five minutes (Figure 4.2c and d) show similar observations, no significant drop of the drain current is seen within ~1 h duration of the measurement, which provides good stability for typical biosensing applications.

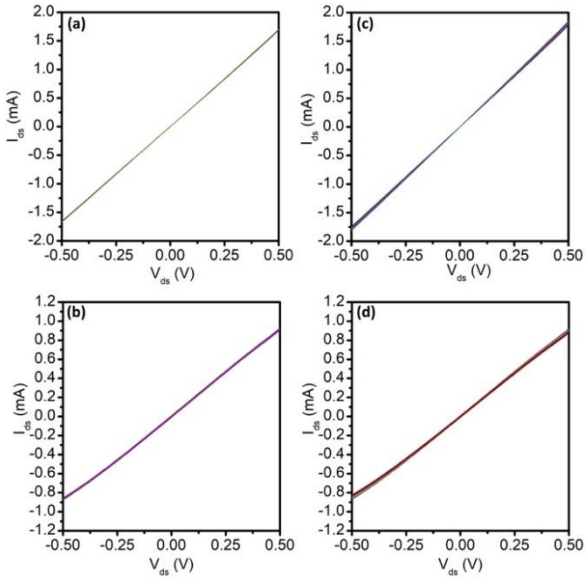

Figure 4.2 *I-V curves of PEDOT:PSS films in PBS buffer containing 0.1 M NaCl for 10 consecutive measurements.*

Note: (a) Pristine PEDOT:PSS measured every 10 s.(b) Pristine PEDOT:PSS measured every 5 minutes. (c) Crosslinked PEDOT:PSS measured every 10 s. (d) Crosslinked PEDOT:PSS measured every 5 minutes.

4.3.2 OECT Characteristics

As mentioned earlier, transfer curve measurement can be used as a conventional platform for biosensing, because it provides important information on the change of "off" and "on" state of the OECTs upon the addition of analytes. A schematic drawing of a typical PEDOT: PSS OECTs based on interdigitated electrodes (IDEs) is shown in Figure 4.1e. Off current (I_{off}) can be achieved when the most positive gate potential $V_{g,\ off}$ is accessed, which represents the scenario of maximal Na^+ ion injection and maximal de-doping of PEDOT:PSS film. When the most negative gate potential $V_{g,\ on}$ is reached, the extraction of Na^+ ions is maximized, resulting in the highest doping level of the film within the sweep of V_g. The drain current at this moment can be denoted as the on current (I_{on}). In the measurements of IDEs based OECTs of this study, the substrate region with IDEs is immersed in water, while maintaining a nitrogen flow on top of the liquid to eliminate the re-dissolving of oxygen (Figure 4.1f).

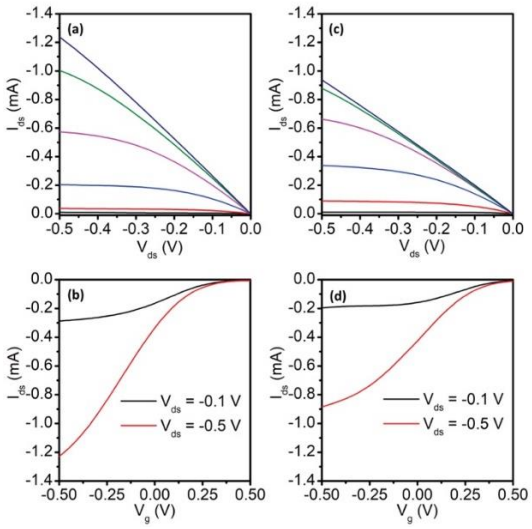

Figure 4.3 *OECT characteristics of pristine (a, b) and GOPS crosslinked (c, d) PEDOT:PSS. (a, c) Output curves for V_g from +0.5 V (bottom curve) to –0.5 V (top curve), stepped by –0.2 V. (b, d) Transfer curves for V_{ds} = –0.1 V and –0.5 V.*

As shown in Figure 4.3a, IDEs based PEDOT:PSS substrates (channel width, W = 1 mm × 20 pairs, channel length, L = 20 μm) show typical output characteristics of electrolyte gated low-voltage OECTs with V_g varying from +0.5 V to –0.5 V. Because PEDOT:PSS operates in depletion mode, the magnitude of the drain current I_{ds} decreases with an increase of gate voltage from negative to positive. The corresponding transfer curves for both V_{ds} = –0.1 V and –0.5 V are presented in Figure 4.3b, which can be referred as the linear regime and saturation regime, respectively. The highest transconductance g_m of the pristine PEDOT:PSS is around 2000 μS and the crosslinked one is around 1500 μS (Figure 4.4), similar to the reported values for a typical PEDOT:PSS OECT device.[20, 25, 32]

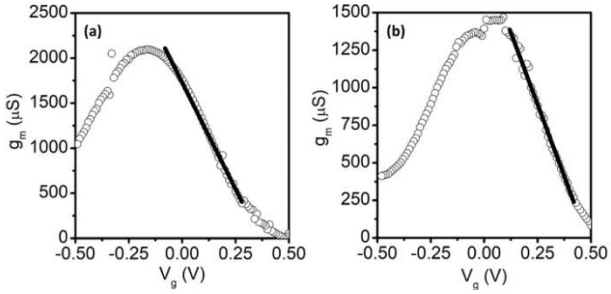

Figure 4.4 *Transconductance of PEDOT:PSS OECTs as a function of gate bias (V_g).*

Note: Mobility estimations of both pristine (a) and crosslinked (b) OECTs can be achieved by fitting the slopes of transconductance curves.

The mobility of the devices (μ) can be estimated from the transconductance g_m in the saturation regime, which is governed by,[5, 20, 32]

$$g_{\mathrm{m}} = \frac{\partial I_{\mathrm{ds}}}{\partial I_{\mathrm{g}}} = \frac{Wd}{L} C^{*} \mu \left(V_{\mathrm{g}} - V_{\mathrm{th}}\right) \qquad \text{(Eq. 4.21)}$$

in which C^* is the capacitance per unit volume and V_{th} is a threshold voltage. A C^* value of 39.3 F/cm^3 is adopted from reported results.[20, 32] The width (W) and length (L)of IDE channel are 20 mm and 20 μm, respectively, resulting in W/L ratio of 1000. The thickness

of the film (*d*) is 60 nm. From the slope of g_m as a function of V_g, the mobilities of pristine and crosslinked OECTs are around 2×10^{-2} cm^2 V^{-1} s^{-1} and 1.6×10^{-2} cm^2 V^{-1} s^{-1}. These values are similar to those of unmodified PEDOT:PSS films reported (10^{-2} cm^2 V^{-1} s^{-1}).[46-48] However, PEDOT:PSS further modified with ethylene glycol and dodecyl benzene sulfonic acid has higher mobility values of 1-2 cm^2 V^{-1} s^{-1} using the same estimation method.[20, 26, 32] From the lower mobility, it can be concluded the close to normal $g_{m,\,max}$ values are due to the exceptional large *W/L* ratio of interdigitated electrodes, which is about 1000 in the substrate used. The large ratio of *W/L* scales up g_m,[28] which compensates the lower mobility of the PEDOT:PSS films prepared here and amplifies the transconductance. This might be a unique advantage of using a substrate with IDEs in OECT devices and provides a potential way to obtain ultra-high transconductance values.

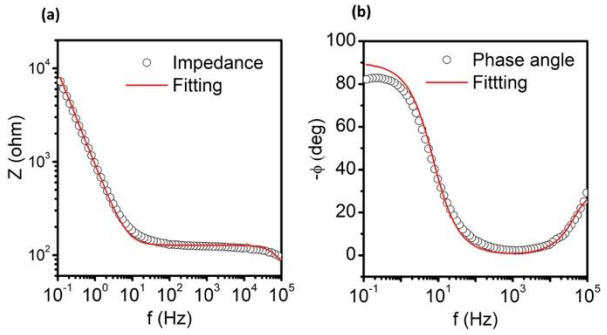

Figure 4.5 *Bode plots of electrochemical impedance spectroscopy for PEDOT:PSS film. Note: (a) Impedance Z. (b) Phase angle.*

Note: Electrochemical impedance spectroscopy (EIS) for determination of capacitance was conducted in a CHI 660A electrochemical workstation from 10 kHz to 0.1 Hz. PEDOT:PSS film is deposited on FTO glass substrate via spin-coating at 3000 rpm. The surface area of the film is about 0.7 cm^2 and film thickness is about 60 nm. EIS data was measured in 0.1M NaCl aqueous solution, using Ag/AgCl as the reference electrode and a Pt mesh as the counter electrode. DC offset potential was chosen to be zero and an AC amplitude of 10 mV is used. To fit the EIS data, equivalent circuit like R_sC or Rs(Rp||C) was adopted. The volumetric capacitance (C*) of PEDOT:PSS is determined to be about 40 F/cm^3.

As for the mobility discrepancy between pristine and crosslinked films, it is difficult to conclude the role of crosslinking in it, because the C^* value is assumed as the same value of 39.3 F/cm^3 in both scenarios. This value is close to our measured result via impedance spectroscopy (Figure 4.5). However, it is unclear whether crosslinking may change the value of C^*.

4.3.3 Stability of Transfer Characteristics

To test the stability of transfer characteristics of PEDOT:PSS, consecutive transfer curve measurements of a pristine OECT device without any GOPS added were performed in a PBS buffer solution. Gate voltage (V_g) was either scanned from +0.5 V to –0.5 V or from +0.2 V to –0.5 V. The former case aimed at imposing larger bias stress as compared to the latter one. The drain-source voltage (V_{ds}) was chosen to be –0.1 V or –0.5 V, which represents the linear regime and saturation regime, respectively. In Figure 4.6, four sets of transfer curves at different bias conditions are presented. When V_g scans from +0.5 V to –0.5 V, a significant decay of drain current (I_{ds}) upon consecutive transfer curve measurements can be observed in both V_{ds}, indicated by arrows in Figure 4.6a and c. At V_{ds} = –0.5V, the I_{on} drop (Figure 4.6a) is close to 20%, while at V_{ds} = –0.1V the I_{on} drop is only about 10% (Figure 4.6c). On the other hand, the decay of I_{on} at the lower gate bias stress (V_g = +0.2 V to –0.5 V) is much less prominent. When higher V_{ds} = –0.5 V is applied, the I_{on} drop is less than 5% as shown in Figure 4.6b. No noticeable drop (<1%) of I_{on} is observed when V_{ds} = –0.1 V (Figure 4.6d).

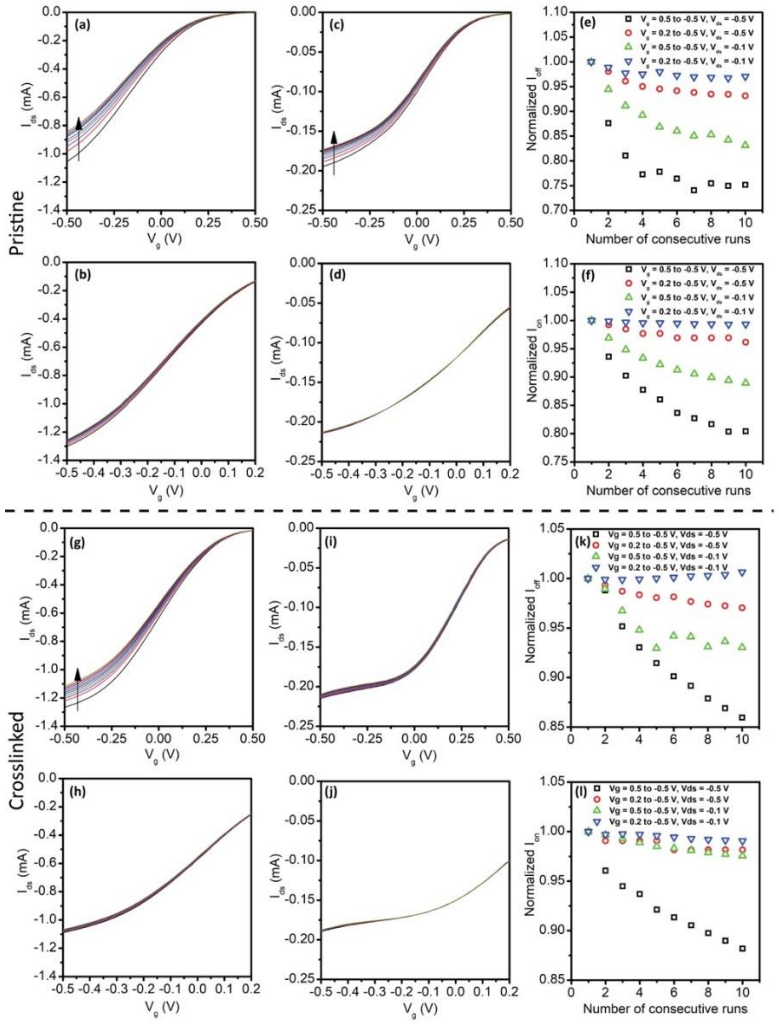

Figure 4.6 *Stability of pristine and crosslinked OECTs upon stress test on transfer curves.*

Note: Top: Consecutive transfer curve measurements of pristine PEDOT:PSS OECT devices in PBS buffer containing 0.1M NaCl at different bias conditions: (a) V_g = +0.5 V to –0.5 V, V_{ds} = –0.5 V; (b) V_g = +0.2 V to –0.5 V, V_{ds} = –0.5 V; (c) V_g = +0.5 V to –0.5 V, V_{ds} = –0.1 V; (d) V_g = +0.2 V to –0.5 V, V_{ds} = –0.1 V. Each test is separated by 10 s. Arrows indicate the decay direction from initial run to final run. In panel (e), "off" current (I_{off}) at $V_{g,\,off}$ from panel (a-d) is normalized with respect to its initial value. Similarly normalized "on" current (I_{on}) at $V_{g,\,on}$ from panel (a-d) is presented in panel (f). Bottom: Consecutive transfer curve measurements of GOPS crosslinked PEDOT:PSS OECT devices in PBS buffer containing 0.1M NaCl at different bias conditions: (g) V_g = +0.5 V to –0.5 V, V_{ds} = –0.5 V; (h) V_g = +0.2 V to –0.5 V, V_{ds} = –0.5 V; (i) V_g = +0.5 V to –0.5 V, V_{ds} = –0.1 V; (j) V_g = +0.2 V to –0.5 V, V_{ds} = –0.1 V. Each test is separated by 10 s. Arrow indicates the decay direction from initial run to final run. In panel (k), "off" current (I_{off}) at $V_{g,\,off}$ from panel (g-j) is normalized with respect to its initial value. Similarly normalized "on" current (I_{on}) at $V_{g,\,on}$ from panel (g-j) is presented in panel (l).

Because off current (I_{off}) is much lower in scale than I_{on}, its decay upon consecutive runs is not simultaneously noticeable in Figure 4.6a-d. To directly visualize and compare the evolution of I_{off} and I_{on} in Figure 4.6a-d, a normalized drain current I_{ds} using initial runs of transfer curve as the reference is introduced in Figure 4.6e and Figure 4.6f. These normalized current results demonstrate that the dependence of I_{off} drop and I_{on} drop with respect to V_g and V_{ds} conditions is highly consistent. When $V_{g,\,off}$ = +0.5 V and V_{ds} = –0.5 V, I_{off} shows a drastic decay of about 20%, which is the most notable one in all sets of conditions. The I_{off} drop is less pronounced at reduced V_{ds} = –0.1 V, which is about 10%. If $V_{g,\,off}$ is chosen as +0.2 V, I_{off} can be stabilized, especially when a lower V_{ds} = –0.1 V is used.

From the analysis on the decay of I_{ds} above, notable decay (>10%) of either I_{on} or I_{off} is always observed at higher $V_{g,\,off}$ = +0.5 V regardless of the V_{ds} value. Thus, V_g clearly has a much larger effect on the stability of consecutive transfer curve measurements than V_{ds}. Indeed, I_{ds} can be further stabilized by using a lower bias of V_{ds} at the same $V_{g,\,off}$, which indicates that higher V_{ds} also reduces the stability of transfer curves. However, if a proper $V_{g,\,off}$ = +0.2 V is selected, the influence of increasing V_{ds} to the stability can be very limited. Practically, for a pristine PEDOT:PSS OECT device, it is reasonably stable to work at the conditions with V_g = +0.2 V to –0.5 V, as the results shown in Figure 4.6c (high $V_{g,\,off}$) and Figure 4.6d (low $V_{g,\,off}$).

As presented in Figure 4.6 bottom, GOPS crosslinked PEDOT:PSS devices exhibit improved stability against V_g stress, especially at high $V_{g,\,off}$ conditions. The decay of I_{ds} (10%-15%) at the harshest condition with high $V_{g,\,off}$ = +0.5 V and V_{ds} = –0.5 V in combined

(Figure 4.6g) is lower than it in pristine PEDOT:PSS. When V_{ds} is reduced to –0.1 V, well-overlapped curves with no drastic decay can be observed even at $V_{g,\,off}$ = +0.5 V (Figure 4.6i). In particular, the drop of "on" current I_{on} (Figure 4.6l) is only about 2.5% while the pristine PEDOT:PSS decays about 10%. In the regime of lower $V_{g,\,off}$, both I_{on} and I_{off} drops are very limited, indicating that a good stability of I_{ds} against consecutive runs at $V_{g,\,off}$ = +0.2 V has been achieved (Figure 4.6h and j).

4.3.4 Stability of Current Response at Pulsed Gate

One of the major advantages of adopting pulsed gate bias is the short measurement time. For example, given that each pulse lasts 0.02 s, a typical pulse train containing 10 alternating "off" and "on" states takes only 0.4 s, which is far shorter than the measurement of a single transfer curve. In addition, on/off cycling operation based on pulsed gate bias has been used as an effective way of testing the stability of an OECT device.[27, 40] Additionally, OECTs based on pulse technique also have shown promising outcomes in neurophysiological applications.[41] Since the improvement in the stability of conventional transfer characteristics by crosslinking has already been shown, it will be worthwhile to extend the scope of this work to pulse technique to fulfill the need of newly emerged applications.

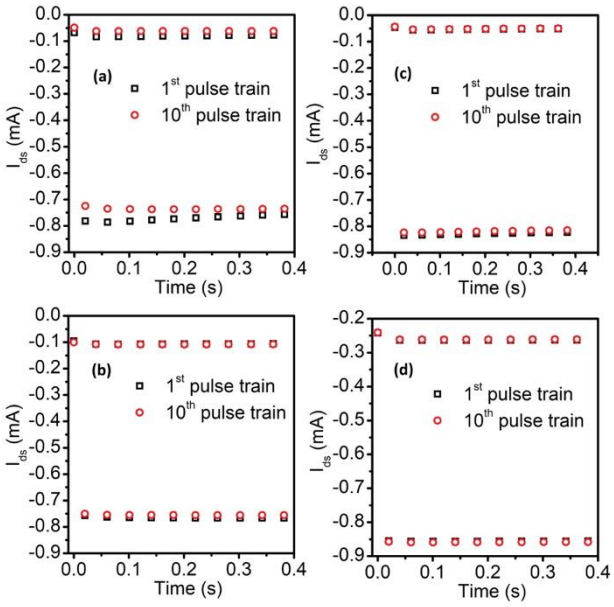

Figure 4.7 *Consecutive pulsed gate bias stress experiments on OECTs.*

Note: Pristine (a, b) and GOPS crosslinked (c, d) PEDOT:PSS OECT devices in PBS buffer containing 0.1M NaCl. Each pulse train of V_g consists of 10 pulses of $V_{g,\,off}$ and 10 pulses of $V_{g,\,on}$. The pulse frequency is 50 Hz, meaning each $V_{g,\,off}$ or $V_{g,\,on}$ pulse lasts 0.02 s. Each consecutive pulse train is separated by 10 s. Gate bias conditions: (a, c) $V_{g,\,off}$ = +0.5 V, $V_{g,\,on}$ = –0.5 V; (b, d) $V_{g,\,off}$ = +0.2 V, $V_{g,\,on}$ = –0.5 V. Note that V_{ds} = –0.5 V for all cases.

Pristine PEDOT:PSS devices only show noticeable decay of I_{ds} at a high $V_{g,\,off}$ = +0.5 V in which the current response in the initial pulse train and the final pulse train of consecutive runs are not well overlapped (Figure 4.7a). I_{on} in the 10th pulse train obviously deviates upwards from its initial values in the 1st pulse train, demonstrating a reduction of its magnitude. When a lower $V_{g,\,off}$ = +0.2 V is applied, regardless of whether crosslinking or not, the current response is very stable (Figure 4.7b, d). Moreover, crosslinked PEDOT:PSS shows great stability against high $V_{g,\,off}$ = +0.5 V(Figure 4.7c) as well, which suggests the stability of crosslinked OECT devices is better in pulsed gate cases than in conventional transfer curve measurements.

To visualize the evolution of I_{on} and I_{off}, results on both pristine and crosslinked devices are summarized in Figure 4.8. Only pristine devices at high $V_{g,\,off}$ have a decay of I_{on} and I_{off} larger than 10% (Figure 4.8a and b), all other devices exhibit good stability in pulsed gate bias cycles.

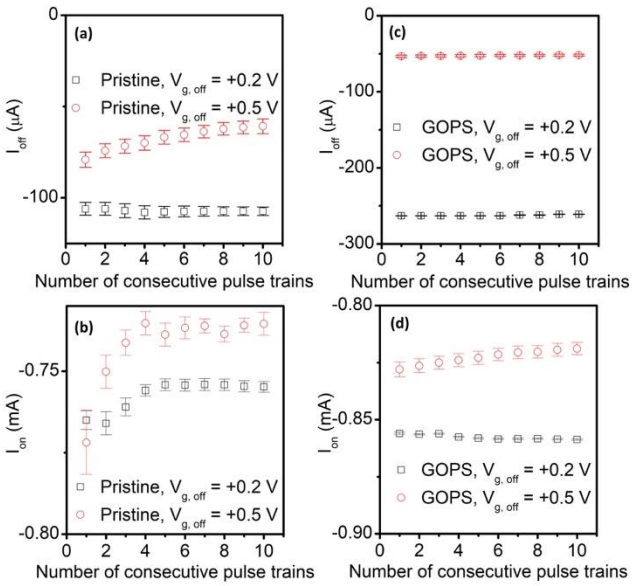

Figure 4.8 *Evolution of I_{off} and I_{on} of OECTs upon pulsed gate bias stress.*

Note: Pristine (a,b) and GOPS crosslinked (c,d) PEDOT:PSS upon high (+0.5 V) and low $V_{g,\,off}$ (+0.2 V) stress. Note that V_{ds} = –0.5 V for all cases.

4.3.5 On/off Ratios

The on/off ratio, another critical feature of a transistor type device, can be affected by the magnitude of $V_{g,\,off}$ and crosslinking. A summary of the on/off ratios of pristine and crosslinked OECTs is presented in Table 4.1. In general, there is a trade-off between on/off ratio performance and device stability. When the highest bias condition is applied ($V_{g,\,off}$ = +0.5 V, V_{ds} = –0.5 V), an on/off ratio exceeds 10^2 can be achieved in pristine PEDOT:PSS OECTs. However, it has been discussed that the decay of I_{ds} is also the largest in this

scenario. Understandably, a higher magnitude of $V_{g,\,off}$ and/or V_{ds} always leads to higher on/off ratios. The former enhances the de-doping of PEDOT:PSS by injecting more Na^+ ions into the film when the bias is engaged, while the latter one ensures the device operating in the saturation regime. However, a high magnitude of $V_{g,\,off}$ appears to have a major adverse effect on the stability of OECTs, while a high V_{ds} also contributes to the decay. For pristine PEDOT:PSS OECTs, stable devices are available when $V_{g,\,off}$ is lowered to +0.2 V, regardless of the form of gate bias, while the on/off ratio is generally around or below 10.

Table 4.1 *On/off Ratio of Pristine and Crosslinked OECTs in Transfer Characteristics and Pulsed Gate Bias Measurements.*

Note: Each bias condition is reproduced in at least three devices.

Bias Conditions	Pristine		Crosslinked	
	On/off ratio	Device Stability	On/off ratio	Device Stability
Transfer, $V_{g,off}$ = +0.5 V, V_{ds} = –0.5 V	140-300	Unstable	40-100	Unstable
Transfer, $V_{g,off}$ = +0.5 V, V_{ds} = –0.1 V	80-90	Unstable	**15-30**	**Stable**
Transfer, $V_{g,off}$ = +0.2 V, V_{ds} = –0.5 V	9-15	Stable	4-6	Stable
Transfer, $V_{g,off}$ = +0.2 V, V_{ds} = –0.1 V	3-6	Stable	2-3	Stable
Pulse, $V_{g,off}$ = +0.5 V, V_{ds} = –0.5 V	7-10	Unstable	**4-15**	**Stable**
Pulse, $V_{g,off}$ = +0.2 V, V_{ds} = –0.5 V	3-7	Stable	2-4	Stable

The enhanced stability brought by the crosslinking of OECTs also comes with a cost of reduced on/off ratio in transfer characteristics. The on/off ratio in transfer characteristics does not exceed 10^2 even at the highest bias condition. However, the highlighted pulse technique cases in Table 4.1 indicates that crosslinked OECTs can show on/off ratios larger than 10 while maintaining improved stability of OECTs device against

a high $V_{g,\,off}$ of +0.5 V. It allows stable operations at the particular high $V_{g,\,off}$ conditions which would otherwise be inaccessible for pristine PEDOT:PSS. The on/off ratio of stable crosslinked OECTs is similar to the reported values of 5-10 in a typical crosslinked PEDOT:PSS device.[49, 50] However, a much higher on/off ratio of ~1500 was recently achieved in crosslinked PEDOT:PSS film prepared by spay-coating.[21]

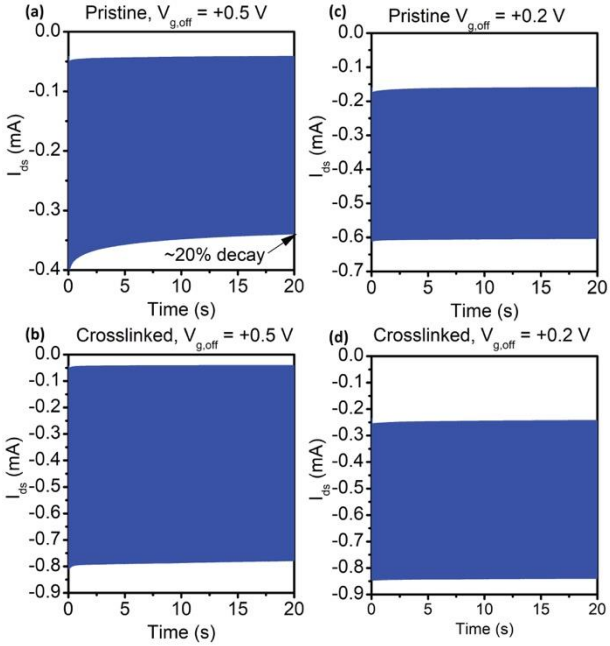

Figure 4.9 *On/off switches of pristine and crosslinked PEDOT:PSS OECTs at pulsed gate bias.*

Note: The total cycle number is 500, with 500 "off" states and 500 "on" states. Each pulse lasts 0.02 s. $V_{g,\,on}$ = –0.5 V and V_{ds} = –0.5 V for all cases. Zoomed in views of panel(a)-(d) can be referred to Figure 4.10.

The stability of OECTs under pulsed gate bias was also examined by large on/off switch cycles. As shown in Figure 4.9a, pristine PEDOT:PSS at $V_{g,\,off}$ = +0.5 V has a ~20% decay in "on" state current. All other devices exhibit good stability against 500 cycles. This observation is consistent with the results discussed earlier, indicating that as long as lower

$V_{g,\,off}$ = +0.2 V is adopted and/or the film is crosslinked, a stable OECT performance can be obtained.

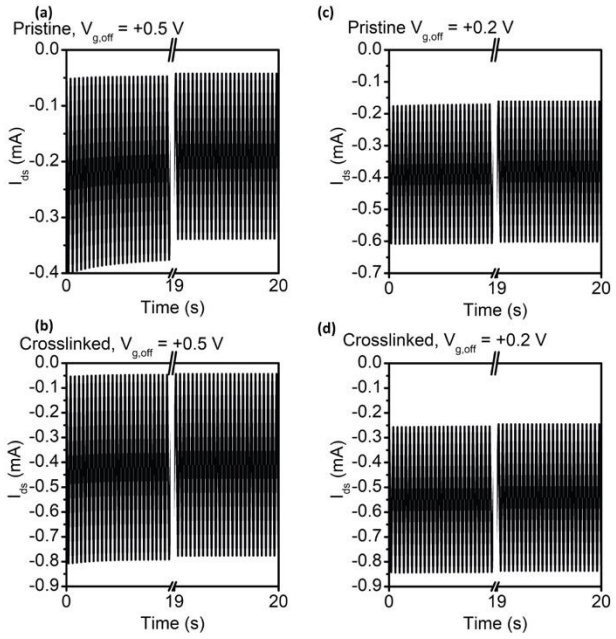

Figure 4.10 *Zoomed-in views of pulse gate stress results in Figure 4.9.*

Note: the first 50 cycles (0-1s) and last 50 cycles (19-20s) of corresponding results on pulsed gate bias stability in Figure 6. (a) Pristine, $V_{g,\,off}$ = +0.5 V. (b) Crosslinked, $V_{g,\,off}$ = +0.5 V. (c) Pristine, $V_{g,\,off}$ = +0.2 V. (d) Crosslinked, $V_{g,\,off}$ = +0.2 V. Note that $V_{g,\,on}$ = –0.5 V and V_{ds} = –0.5 V are for all cases.

4.3.6 Plausible Explanation on the Crosslinking Promoted Stabilization

The reason why higher $V_{g,\,off}$ (i.e. +0.5 V) deteriorates the stability of PEDOT:PSS based OECT device remains unclear. Previously, parasitic reactions with dissolved oxygen at high V_g has been considered as a possible cause for the instability for OECT devices operated in an aqueous solution.[27, 39] In our present study, the dissolved oxygen effect is carefully eliminated by deaerating the solution with high purity N_2 gas as well as maintaining a N_2 atmosphere on top of the solution. However, a significant drain current decay was still observed at higher $V_{g,\,off}$. It is well known that at positive $V_{g,\,off}$, Na^+ ions are injected into the PEDOT:PSS film. Therefore, the detrimental effect on the stability of

PEDOT:PSS may stem from the repetitive intercalation-extraction of Na^+ ions. Crosslinking of PEDOT:PSS film has been suggested to decrease its capacity of water uptake with lower ion mobility and electrical conductivity resulting from the reduction in the film swelling after GOPS crosslinking.[46] To probe the possible difference in ion mobility of pristine and crosslinked PEDOT:PSS OECTs, drain currents were recorded at various pulse frequencies while $V_{g,\,off}$ = +0.2 V was adopted so that both OECTs can operate in stable conditions. The results show that normalized I_{off} and I_{on} behave similarly for pristine and crosslinked devices, where a transition towards a steady state is observed at ~50 Hz (Figure 4.11). Furthermore, even if the ion mobility is reduced at a higher magnitude of $V_{g,\,off}$, it is not clear that whether the reduced ion mobility is directly related to the stability of PEDOT:PSS OECTs. Savva *et al*. have suggested that hydrophilic conjugated polymers such as PEDOT:PSS undergo significant volume expansion due to the uptake of hydrated cations and water, and the film shrinks as water and hydrated cations are ejected.[51] This kind of expansion-shrinking processes could impose long-lasting changes on the structure of conjugated polymer films and deteriorate the doping/de-doping efficiency, reversibility, and response speed of OECTs.[51, 52]

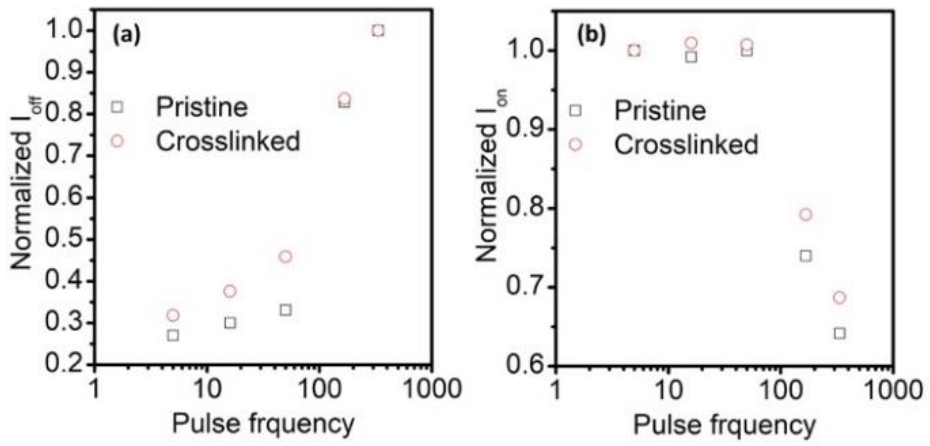

Figure 4.11 *Normalized drain current response as a function of pulse frequency.*

Note: (a) Normalized "on" state current (I_{on}). (b) Normalized "off" state current (I_{off}). Note that in pulse experiments, $V_{g,\,off}$ = +0.2 V, $V_{g,\,on}$ = -0.5 V, V_{ds} = -0.5 V.

Our preliminary AFM topography results in Figure 4.12 indicates that the surface roughness (RMS) of pristine PEDOT:PSS film decreases after cycled stress test similar to the condition in Figure 4.9a (V_g = +0.5 V to -0.5 V, V_{ds} = -0.5 V), while crosslinked film does not exhibit the same trend under the same condition. However, due to the limitations in the characterization methods employed in this work, the microscopic evolution of film structure upon consecutive gate bias stress cannot be fully revealed. Nevertheless, the results discussed above show that a proper selection of bias condition and crosslinking helps to minimize the effect brought by adverse structural changes of the hydrophilic conjugated polymeric films.

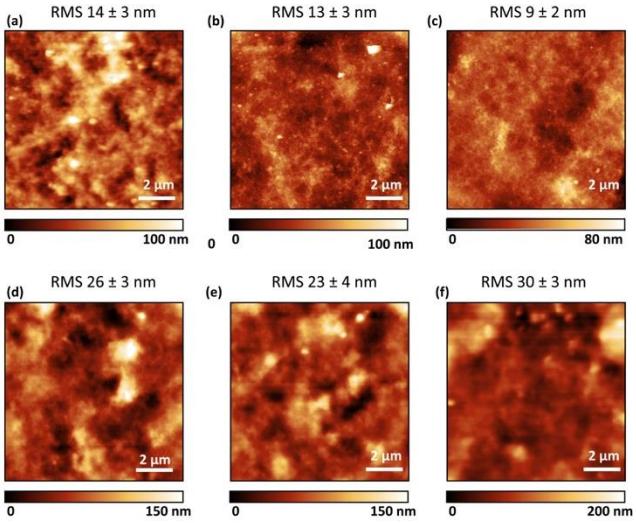

Figure 4.12 *AFM images of PEDOT:PSS films before and after immersion or pulsed bias stress.*

Note: (a) Pristine film. (b) Pristine film soaked in PBS buffer for 30 mins. (c) Prisitne film after 500 on/off cycles at V_g = +0.5 V to -0.5 V, V_{ds} = -0.5 V. (d) Crosslinked film. (e) Crosslinked film soaked in PBS buffer for 30 mins. (f) Crosslinked film after 500 on/off cycles at V_g = +0.5 V to -0.5 V, V_{ds} = -0.5 V. All samples were blow dried by N_2 before AFM measurement.

4.4 Conclusion

The critical role of gate voltages at the off state ($V_{g, off}$) on the stability of an OECT based on IDEs in PBS buffer has been demonstrated. As for pristine PEDOT:PSS, when a high $V_{g, off}$ of +0.5 V is used, a significant decay of drain current can be observed upon consecutive measurements in both the transfer characteristics and current response under pulsed gated bias. Pristine PEDOT:PSS OECTs can be stabilized by lowering $V_{g, off}$ to +0.2 V, resulting in a reduced on/off ratio due to the increase of off current. On the other hand, The GOPS crosslinked PEDOT:PSS ones show improved stability against high $V_{g, off}$ in both scenarios. In particular, crosslinked OECTs under the harshest pulsed gate bias condition ($V_{g, off}$ = +0.5 V, V_{ds} = –0.5 V) exhibit a stable on/off ratio of 4-15 upon cycling of gate bias. The PEDOT:PSS film decomposition in PBS buffer has been excluded as a cause for the decay of drain current because without the presence of gate bias, the *I-V*

curves for both pristine and crosslinked PEDOT:PSS film are stable. Source-drain voltage is also shown to have a minor effect on the deterioration of drain current upon repetitive gate bias stress. The repetitive process of Na^+ ion intercalation-extraction at high $V_{g,\,off}$ is believed to be the most probable cause of the decay. Crosslinking of the film might mitigate this adverse effect caused by expansion-shrinking during the repetitive switches between "de-doped" and "doped" state, leading to an improvement of the cycle stability. However, there are still questions remain unanswered. In particular, why the maximal extraction of Na^+ ions at $V_{g,\,on}$ has no noticeable effect on the stability of OECTs. More studies on the process of the intercalation and extraction of ions for CP based materials are needed to further investigate this question. We hope the results presented in this work would be helpful in the selection of the right working conditions for the OECT applications including biosensing.

Reference

1. Inal, S.; Rivnay, J.; Suiu, A.-O.; Malliaras, G. G.; McCulloch, I., Conjugated polymers in bioelectronics. *Acc. Chem. Res.* **2018,** *51* (6), 1368-1376.
2. Rivnay, J.; Inal, S.; Salleo, A.; Owens, R. M.; Berggren, M.; Malliaras, G. G., Organic electrochemical transistors. *Nat. Rev. Mater.* **2018,** *3* (2), 17086.
3. Moser, M.; Ponder Jr, J. F.; Wadsworth, A.; Giovannitti, A.; McCulloch, I., Materials in organic electrochemical transistors for bioelectronic applications: past, present, and future. *Adv. Funct. Mater.* **2019,** *29* (21), 1807033.
4. Paulsen, B. D.; Tybrandt, K.; Stavrinidou, E.; Rivnay, J., Organic mixed ionic–electronic conductors. *Nat. Mater.* **2019**, 1-14.
5. Bernards, D. A.; Malliaras, G. G., Steady-state and transient behavior of organic electrochemical transistors. *Adv. Funct. Mater.* **2007,** *17* (17), 3538-3544.
6. Zhu, Z.-T.; Mabeck, J. T.; Zhu, C.; Cady, N. C.; Batt, C. A.; Malliaras, G. G., A simple poly (3, 4-ethylene dioxythiophene)/poly (styrene sulfonic acid) transistor for glucose sensing at neutral pH. *Chem. Commun.* **2004,** (13), 1556-1557.
7. Liao, C.; Zhang, M.; Niu, L.; Zheng, Z.; Yan, F., Highly selective and sensitive glucose sensors based on organic electrochemical transistors with graphene-modified gate electrodes. *J. Mater. Chem. B* **2013,** *1* (31), 3820-3829.
8. Tang, H.; Yan, F.; Lin, P.; Xu, J.; Chan, H. L., Highly sensitive glucose biosensors based on organic electrochemical transistors using platinum gate electrodes modified with enzyme and nanomaterials. *Adv. Funct. Mater.* **2011,** *21* (12), 2264-2272.
9. Wustoni, S.; Savva, A.; Sun, R.; Bihar, E.; Inal, S., Enzyme-free detection of glucose with a hybrid conductive gel electrode. *Adv. Mater. Interfaces* **2019,** *6* (1), 1800928.
10. Berto, M.; Diacci, C.; Theuer, L.; Di Lauro, M.; Simon, D. T.; Berggren, M.; Biscarini, F.; Beni, V.; Bortolotti, C. A., Label free urea biosensor based on organic electrochemical transistors. *Flexible Printed Electron.* **2018,** *3* (2), 024001.
11. Liao, C.; Mak, C.; Zhang, M.; Chan, H. L.; Yan, F., Flexible organic electrochemical transistors for highly selective enzyme biosensors and used for saliva testing. *Adv. Mater.* **2015,** *27* (4), 676-681.
12. Khodagholy, D.; Curto, V. F.; Fraser, K. J.; Gurfinkel, M.; Byrne, R.; Diamond, D.; Malliaras, G. G.; Benito-Lopez, F.; Owens, R. M., Organic electrochemical transistor incorporating an ionogel as a solid state electrolyte for lactate sensing. *J. Mater. Chem.* **2012,** *22* (10), 4440-4443.
13. Liao, C.; Zhang, M.; Niu, L.; Zheng, Z.; Yan, F., Organic electrochemical transistors with graphene-modified gate electrodes for highly sensitive and selective dopamine sensors. *J. Mater. Chem. B* **2014,** *2* (2), 191-200.
14. Tang, H.; Lin, P.; Chan, H. L.; Yan, F., Highly sensitive dopamine biosensors based on organic electrochemical transistors. *Biosens. Bioelectron.* **2011,** *26* (11), 4559-4563.
15. Fu, Y.; Wang, N.; Yang, A.; Law, H. K. w.; Li, L.; Yan, F., Highly sensitive detection of protein biomarkers with organic electrochemical transistors. *Adv. Mater.* **2017,** *29* (41), 1703787.

16. Macchia, E.; Romele, P.; Manoli, K.; Ghittorelli, M.; Magliulo, M.; Kovács-Vajna, Z. M.; Torricelli, F.; Torsi, L., Ultra-sensitive protein detection with organic electrochemical transistors printed on plastic substrates. *Flexible Printed Electron.* **2018,** *3* (3), 034002.
17. Strakosas, X.; Sessolo, M.; Hama, A.; Rivnay, J.; Stavrinidou, E.; Malliaras, G. G.; Owens, R. M., A facile biofunctionalisation route for solution processable conducting polymer devices. *J. Mater. Chem. B* **2014,** *2* (17), 2537-2545.
18. Wustoni, S.; Wang, S.; Alvarez, J. R.; Hidalgo, T. C.; Nunes, S. P.; Inal, S., An organic electrochemical transistor integrated with a molecularly selective isoporous membrane for amyloid-β detection. *Biosens. Bioelectron.* **2019,** *143*, 111561.
19. Sessolo, M.; Khodagholy, D.; Rivnay, J.; Maddalena, F.; Gleyzes, M.; Steidl, E.; Buisson, B.; Malliaras, G. G., Easy-to-fabricate conducting polymer microelectrode arrays. *Adv. Mater.* **2013,** *25* (15), 2135-2139.
20. Rivnay, J.; Leleux, P.; Ferro, M.; Sessolo, M.; Williamson, A.; Koutsouras, D. A.; Khodagholy, D.; Ramuz, M.; Strakosas, X.; Owens, R. M., High-performance transistors for bioelectronics through tuning of channel thickness. *Sci. Adv.* **2015,** *1* (4), e1400251.
21. Ko, J.; Wu, X.; Surendran, A.; Muhammad, B. T.; Leong, W. L., Self-Healable Organic Electrochemical Transistor with High Transconductance, Fast Response, and Long-Term Stability. *ACS Appl. Mater. Interfaces* **2020,** *12* (30), 33979-33988.
22. Wu, X.; Surendran, A.; Moser, M.; Chen, S.; Muhammad, B. T.; Maria, I. P.; McCulloch, I.; Leong, W. L., Universal Spray-Deposition Process for Scalable, High-Performance, and Stable Organic Electrochemical Transistors. *ACS Appl. Mater. Interfaces* **2020,** *12* (18), 20757-20764.
23. Kaphle, V.; Liu, S.; Al-Shadeedi, A.; Keum, C. M.; Lüssem, B., Contact resistance effects in highly doped organic electrochemical transistors. *Adv. Mater.* **2016,** *28* (39), 8766-8770.
24. Kaphle, V.; Liu, S.; Keum, C. M.; Lüssem, B., Organic electrochemical transistors based on room temperature ionic liquids: performance and stability. *Phys. Status Solidi A* **2018,** *215* (24), 1800631.
25. Khodagholy, D.; Rivnay, J.; Sessolo, M.; Gurfinkel, M.; Leleux, P.; Jimison, L. H.; Stavrinidou, E.; Herve, T.; Sanaur, S.; Owens, R. M., High transconductance organic electrochemical transistors. *Nat. Commun.* **2013,** *4* (1), 1-6.
26. Rivnay, J.; Inal, S.; Collins, B. A.; Sessolo, M.; Stavrinidou, E.; Strakosas, X.; Tassone, C.; Delongchamp, D. M.; Malliaras, G. G., Structural control of mixed ionic and electronic transport in conducting polymers. *Nat. Commun.* **2016,** *7* (1), 1-9.
27. Keene, S. T.; van der Pol, T. P.; Zakhidov, D.; Weijtens, C. H.; Janssen, R. A.; Salleo, A.; van de Burgt, Y., Enhancement-Mode PEDOT: PSS Organic Electrochemical Transistors Using Molecular De-Doping. *Adv. Mater.* **2020,** *32* (19), 2000270.
28. Rivnay, J.; Leleux, P.; Sessolo, M.; Khodagholy, D.; Hervé, T.; Fiocchi, M.; Malliaras, G. G., Organic electrochemical transistors with maximum transconductance at zero gate bias. *Adv. Mater.* **2013,** *25* (48), 7010-7014.

29. Zhang, S.; Kumar, P.; Nouas, A. S.; Fontaine, L.; Tang, H.; Cicoira, F., Solvent-induced changes in PEDOT: PSS films for organic electrochemical transistors. *APL Mater.* **2015,** *3* (1), 014911.
30. Mantione, D.; del Agua, I.; Schaafsma, W.; ElMahmoudy, M.; Uguz, I.; Sanchez-Sanchez, A.; Sardon, H.; Castro, B. a.; Malliaras, G. G.; Mecerreyes, D., Low-temperature cross-linking of PEDOT: PSS films using divinylsulfone. *ACS Appl. Mater. Interfaces* **2017,** *9* (21), 18254-18262.
31. del Agua, I.; Mantione, D.; Ismailov, U.; Sanchez-Sanchez, A.; Aramburu, N.; Malliaras, G. G.; Mecerreyes, D.; Ismailova, E., DVS-Crosslinked PEDOT: PSS Free-Standing and Textile Electrodes toward Wearable Health Monitoring. *Adv. Mater. Technol.* **2018,** *3* (10), 1700322.
32. Inal, S.; Malliaras, G. G.; Rivnay, J., Benchmarking organic mixed conductors for transistors. *Nat. Commun.* **2017,** *8* (1), 1-7.
33. Zeglio, E.; Vagin, M.; Musumeci, C.; Ajjan, F. N.; Gabrielsson, R.; Trinh, X. T.; Son, N. T.; Maziz, A.; Solin, N.; Inganäs, O., Conjugated polyelectrolyte blends for electrochromic and electrochemical transistor devices. *Chem. Mater.* **2015,** *27* (18), 6385-6393.
34. Flagg, L. Q.; Bischak, C. G.; Onorato, J. W.; Rashid, R. B.; Luscombe, C. K.; Ginger, D. S., Polymer crystallinity controls water uptake in glycol side-chain polymer organic electrochemical transistors. *J. Am. Chem. Soc.* **2019,** *141* (10), 4345-4354.
35. Flagg, L. Q.; Giridharagopal, R.; Guo, J.; Ginger, D. S., Anion-dependent doping and charge transport in organic electrochemical transistors. *Chem. Mater.* **2018,** *30* (15), 5380-5389.
36. Wustoni, S.; Combe, C.; Ohayon, D.; Akhtar, M. H.; McCulloch, I.; Inal, S., Membrane-Free Detection of Metal Cations with an Organic Electrochemical Transistor. *Adv. Funct. Mater.* **2019,** *29* (44), 1904403.
37. Fuller, E. J.; Keene, S. T.; Melianas, A.; Wang, Z.; Agarwal, S.; Li, Y.; Tuchman, Y.; James, C. D.; Marinella, M. J.; Yang, J. J., Parallel programming of an ionic floating-gate memory array for scalable neuromorphic computing. *Science* **2019,** *364* (6440), 570-574.
38. Melianas, A.; Quill, T.; LeCroy, G.; Tuchman, Y.; Loo, H. v.; Keene, S.; Giovannitti, A.; Lee, H.; Maria, I.; McCulloch, I., Temperature-resilient solid-state organic artificial synapses for neuromorphic computing. *Sci. Adv.* **2020,** *6* (27), eabb2958.
39. Keene, S. T.; Melianas, A.; van de Burgt, Y.; Salleo, A., Mechanisms for enhanced state retention and stability in redox-gated organic neuromorphic devices. *Adv. Electron. Mater.* **2019,** *5* (2), 1800686.
40. van de Burgt, Y.; Lubberman, E.; Fuller, E. J.; Keene, S. T.; Faria, G. C.; Agarwal, S.; Marinella, M. J.; Talin, A. A.; Salleo, A., A non-volatile organic electrochemical device as a low-voltage artificial synapse for neuromorphic computing. *Nat. Mater.* **2017,** *16* (4), 414-418.
41. van De Burgt, Y.; Melianas, A.; Keene, S. T.; Malliaras, G.; Salleo, A., Organic electronics for neuromorphic computing. *Nature Electronics* **2018,** *1* (7), 386-397.

42. Lee, M.-H.; Chen, L.; Li, N.; Zhu, F., MoO 3-induced oxidation doping of PEDOT: PSS for high performance full-solution-processed inverted quantum-dot light emitting diodes. *J. Mater. Chem. C* **2017,** *5* (40), 10555-10561.
43. Park, H.; Shi, Y.; Kong, J., Application of solvent modified PEDOT: PSS to graphene electrodes in organic solar cells. *Nanoscale* **2013,** *5* (19), 8934-8939.
44. Zhang, W.; Bi, X.; Zhao, X.; Zhao, Z.; Zhu, J.; Dai, S.; Lu, Y.; Yang, S., Isopropanol-treated PEDOT: PSS as electron transport layer in polymer solar cells. *Org. Electron.* **2014,** *15* (12), 3445-3451.
45. Håkansson, A.; Han, S.; Wang, S.; Lu, J.; Braun, S.; Fahlman, M.; Berggren, M.; Crispin, X.; Fabiano, S., Effect of (3-glycidyloxypropyl) trimethoxysilane (GOPS) on the electrical properties of PEDOT: PSS films. *J. Polym. Sci., Part B: Polym. Phys.* **2017,** *55* (10), 814-820.
46. Stavrinidou, E.; Leleux, P.; Rajaona, H.; Khodagholy, D.; Rivnay, J.; Lindau, M.; Sanaur, S.; Malliaras, G. G., Direct measurement of ion mobility in a conducting polymer. *Adv. Mater.* **2013,** *25* (32), 4488-4493.
47. Rutledge, S.; Helmy, A., Carrier mobility enhancement in poly (3, 4-ethylenedioxythiophene)-poly (styrenesulfonate) having undergone rapid thermal annealing. *J. Appl. Phys.* **2013,** *114* (13), 133708.
48. Wei, Q.; Mukaida, M.; Naitoh, Y.; Ishida, T., Morphological change and mobility enhancement in PEDOT: PSS by adding co-solvents. *Adv. Mater.* **2013,** *25* (20), 2831-2836.
49. Kumar, P.; Yi, Z.; Zhang, S.; Sekar, A.; Soavi, F.; Cicoira, F., Effect of channel thickness, electrolyte ions, and dissolved oxygen on the performance of organic electrochemical transistors. *Appl. Phys. Lett.* **2015,** *107*, 053303.
50. Zhang, S.; Hubis, E.; Tomasello, G.; Soliveri, G.; Kumar, P.; Cicoira, F., Patterning of stretchable organic electrochemical transistors. *Chem. Mater.* **2017,** *29* (7), 3126-3132.
51. Savva, A.; Wustoni, S.; Inal, S., Ionic-to-electronic coupling efficiency in PEDOT: PSS films operated in aqueous electrolytes. *J. Mater. Chem. C* **2018,** *6* (44), 12023-12030.
52. Savva, A.; Cendra, C.; Giugni, A.; Torre, B.; Surgailis, J.; Ohayon, D.; Giovannitti, A.; McCulloch, I.; Di Fabrizio, E.; Salleo, A.; Rivnay, J.; Inal, S., Influence of water on the performance of organic electrochemical transistors. *Chem. Mater.* **2019,** *31* (3), 927-937.

CHAPTER V – Summary and Outlook

As shown in Chapter II and Chapter III, the combination of optical spectroscopy and AFM microscopy has been proved as a powerful route for the investigation of the structure-property relationship of conjugated polymers. The phenomena of CP aggregation in marginal solvent and chemical doping of CPs are often entangled, which means aggregation can promote chemical doping, and vice versa, chemical doping can facilitate the aggregation. To elucidate which phenomenon occurs in solution first, the UV-vis spectra from low molecular P3HT were collected and analyzed. No noticeable doping of fully dissolved P3HT can be observed in toluene. By introducing an anti-solvent, decane, aggregation of P3HT is initiated, followed by the proceeding of chemical doping reaction. Due to the interpretation of these results, aggregation and chemical doping can be decoupled. Aggregation can be regarded as a more prior step in solutions as compared to chemical doping. Using AFM equipped with Kelvin probe force microscopy (KPFM), pristine, doped, and partially dedoped P3HT films can be differentiated by a comparison of their characteristic surface potential values, which sheds light on the application of KPFM in the identification of highly polar compounds with strong molecular dipole such as F4TCNQ. In Chapter II, the lateral resolution of the AFM/KPFM technique is exhibited in a well-dispersed P3HT nanowire network film. Although the width of P3HT nanowires under AFM is below 50 nm, pristine and doped nanowires can still be differentiated by KPFM. Even more, in overly doped nanowire network samples, KPFM can also pick up the excess neutral dopant with a distinct “dark dot” feature, indicating a much lower surface

potential as compared to the ITO reference. The measured conductivity of doped P3HT nanowires prepared from orthogonal doping can exceed 0.1 S/cm, which is significantly enhanced from the pristine form of P3HT.

Despite the progress in the research of chemical doping of CPs, using combined spectroscopical and microscopical techniques, there are still some important topics needed to be addressed in future investigations. First, the dopant is thought to reside in the CP host upon finishing the doping reaction. However, it is still unclear where the precise locations of it within the CPs. As it has been discussed in Chapter III, dopant molecules are not very likely to diffuse into π-π stacks due to steric limitation, though this possibility cannot be fully excluded especially in the scenario of solution doping. The dopant is more likely to reside in the internal lamellar region and/or on top of a CP film. However, to confirm it a lateral resolution of at least sub 10 nm is required. Due to the nature of the AFM/KPFM technique, it is not very practical to obtain such a resolution. Techniques such as scanning transmission electron microscope (STEM) or small-angle X-ray scattering might be more suitable in achieving such delicate surface resolutions, while some significant technical questions need to be considered beforehand. For example, STEM requires a high vacuum to achieve a satisfactorily high resolution, while the dopant molecules in the doped CP samples are not stable under vacuum. They tend to drift away from the film and sublime. The diffusion of molecular dopant not only hinders the high-resolution study on its locations with the CPs, but it also brings up a second question, that is the long-term stability of doped CP films. The undesired diffusion and degradation of dopant within CP film, together with parasitic reactions of CP with oxygen and moisture, causing instability of

devices based on doped CPs, which also hamper their applications. Recently, there is an emerging new category of CPs named as donor-acceptor (D-A) conjugated polymer.[1-3] Within the monomer unit, partial charge transfer occurs from a "donor" segment to an "acceptor" segment. For example, in a typical D-A polymer, diketopyrrolopyrrole-dithienylthieno[3,2-b]thiophene (DPP-DTT), thiophene can donate electrons to the pyrrolopyrrole acceptor within a monomer unit. The "self-doping" D-A polymer seems to exhibit much better thermal stability and electrical properties as compared to conventional doped CPs. The OFET devices based on D-A polymers exhibit high hole mobility (~10 $cm^2\ V^{-1}\ s^{-1}$) while maintaining stable characteristics for several months even under an ambient environment without encapsulation.[2] The idea of incorporation D-A mechanism of doping within a polymer chain is rather intriguing and exciting, since it avoids the inevitable diffusion and degradation of small molecular dopants within a conventional CP matrix and thus naturally improved the stability of doped CP devices. However, whether the excellent stability of the D-A polymer can be solely attributed to the D-A mechanism is not clear. At the same time, not much knowledge has been gained in the self-doping mechanism of D-A. For example, there is little investigation on whether the polymorph or aggregation of D-A polymer has an impact on the doping efficiency and electrical properties. As the research in self doping D-A polymers goes further, fundamental understanding of its doping mechanism will become more and more critical for the pursuit of even higher electrical performance. Therefore, the knowledge and techniques from the dissertation might be useful for this purpose, especially the combinational approach of spectroscopy and microscopy.

In Chapter IV, the electrochemical manipulation of the doping of a typical CP, PEDOT:PSS, is performed on prefabricated interdigitated electrodes. In OECT devices, the doping level of a CP film is manipulated by controlling the ion injection into the film, which is directly related to the bias of the gate electrode. By adopting a prefabricated IDE substrate for device fabrication, a facile route for the fabrication of inexpensive and lithography-free OECTs is established for water-soluble CPs such as PEDOT:PSS. In both transfer curve and pulsed gate bias measurements, stable working conditions can be found. Meanwhile, crosslinking of PEDOT:PSS by a silane crosslinker such as GOPS is proved to be critical for improving device stability. The field of OECT is also attracting increasing research attention due to its potential applications in biosensing and neural signal processing. Multiple interesting and important research directions exist. First, as a pragmatic idea, the IDE based glass substrate can be substituted by a flexible substrate such as PDMS to better meet the demand of flexible electronics, as suggested by the recent publications.[4, 5] The synthesis of novel soft substrate materials and characterization of their mechanical properties and bio-compatibilities can be an exciting and challenging topic for future study. Second, it is not clear why crosslinking has a significant effect on the stabilization of OECTs upon bias stress. As discussed before, the CP films might undergo expanding upon ion injection and shrinking upon ion extraction. This expanding-shrinking process is thought to cause irreversible structural changes to a CP film. Thus, the role of crosslinking in the mitigation against the structural deterioration might be increasing the rigidity of the CP films. To examine this possibility, probing in-situ film topography evolution in an aqueous environment upon real gate bias conditions is needed. This requires

advanced in-situ AFM sample measurements in liquid and other possible in-situ quantitative techniques such as EQCM. Third, for the application of biosensing, the metal gate used in OECTs such as Au, Ag, or Pt must be properly modified to effectively capture targeting analytes. For instance, if a certain protein is a target, a highly specific receptor has to be covalently connected with the chemically modified gate electrode via surface coupling reactions such as EDC/NHS coupling between carboxylic and amine groups. After the successful modification of the metal gate, the drain current should respond differently with or without the presence of an analyte in the solution due to the binding events. The OECTs with the receptor-modified gate electrode have been reported for the fluorescent label-free sensing of biological analytes such as proteins or biomakers.[6, 7] However, it should be stressed that the bio-related research can be both expensive and challenging. Despite the drain current response can be observed in the sensing of biomolecules, the sensing mechanism behind the drain current response is not well elucidated.

In all, this chapter summarizes the work involved in the previous chapters, covering both the chemical doping and electrochemical doping part of the overall project. Apart from the obtained knowledge, some important research directions for future studies have also been outlined.

Reference

1. Chen, H.; Guo, Y.; Yu, G.; Zhao, Y.; Zhang, J.; Gao, D.; Liu, H.; Liu, Y., Highly π-extended copolymers with diketopyrrolopyrrole moieties for high-performance field-effect transistors. *Adv. Mater.* **2012,** *24* (34), 4618-4622.
2. Lei, Y.; Deng, P.; Li, J.; Lin, M.; Zhu, F.; Ng, T.-W.; Lee, C.-S.; Ong, B. S., Solution-processed donor-acceptor polymer nanowire network semiconductors for high-performance field-effect transistors. *Sci. Rep.* **2016,** *6* (1), 1-9.
3. Li, J.; Zhao, Y.; Tan, H. S.; Guo, Y.; Di, C.-A.; Yu, G.; Liu, Y.; Lin, M.; Lim, S. H.; Zhou, Y., A stable solution-processed polymer semiconductor with record high-mobility for printed transistors. *Sci. Rep.* **2012,** *2* (1), 1-9.
4. Ko, J.; Wu, X.; Surendran, A.; Muhammad, B. T.; Leong, W. L., Self-Healable Organic Electrochemical Transistor with High Transconductance, Fast Response, and Long-Term Stability. *ACS Appl. Mater. Interfaces* **2020,** *12* (30), 33979-33988.
5. Wu, X.; Surendran, A.; Moser, M.; Chen, S.; Muhammad, B. T.; Maria, I. P.; McCulloch, I.; Leong, W. L., Universal Spray-Deposition Process for Scalable, High-Performance, and Stable Organic Electrochemical Transistors. *ACS Appl. Mater. Interfaces* **2020,** *12* (18), 20757-20764.
6. Fu, Y.; Wang, N.; Yang, A.; Law, H. K. w.; Li, L.; Yan, F., Highly sensitive detection of protein biomarkers with organic electrochemical transistors. *Adv. Mater.* **2017,** *29* (41), 1703787.
7. Macchia, E.; Romele, P.; Manoli, K.; Ghittorelli, M.; Magliulo, M.; Kovács-Vajna, Z. M.; Torricelli, F.; Torsi, L., Ultra-sensitive protein detection with organic electrochemical transistors printed on plastic substrates. *Flexible Printed Electron.* **2018,** *3* (3), 034002.